2D simulation of heat flux distribution in space-relevant applications including electromagnetic fields in partially-ionized Argon plasmas

INAUGURALDISSERTATION

zur

Erlangung des akademischen Grades eines

doctor rerum naturalium (Dr. rer. nat.)

an der Mathematisch-Naturwissenschaftlichen Fakulät

der

Ernst-Moritz-Arndt-Universität Greifswald

vorgelegt von

Karl Felix Lüskow

geboren am 21. April 1990

in Brandenburg a. d. Havel, Deutschland

Greifswald, den 13. April 2018

Dekan: Prof. Dr. Werner Weitschies
1. Gutachter: Prof. Dr. Ralf Schneider
2. Gutachter: Dr. David Tskhakaya
Tag der Disputation: 20. Juli 2018

Abstract

Manipulating and utilizing plasmas becomes a more and more important task in various research fields of physics and in industrial developments. Especially in nowadays space-relevant applications there are different ideas to modify plasmas concerning particular tasks. One major point of interest is the ability to influence plasmas using magnetic fields. To study the underlying physical effects that were achieved by these magnetic fields for both scenarios Particle-in-Cell simulations were done. Two examples are discussed in this thesis.

The first example originates from an experiment performed by the European Space Agency ESA in collaboration with the German Space Agency DLR. To verify the possibility of heat-flux reduction by magnetic fields onto the thermal protection system of a space vehicle a simplified experiment on earth was developed. Most of the heat that is created during re-entry comes from compression of the air ahead of the hypersonic vehicle, as a result of the basic thermodynamic relation between temperature and pressure. The shock front, which builds up in front of the vehicle deflects most of the heat and prohibits the surface of the space vehicle from direct contact with the maximum flux. State of the art spacecrafts use highly developed materials like ceramics to handle the enormous heat. An attractive approach to reduce costs is to use magnetic fields for heat-flux reduction. This would allow the use of cheaper materials and thus reduce costs for the whole space mission. A partially-ionized Argon beam was used to create a certain heat-flux onto a target. The main finding of the experimental campaign was a large mitigation of heat-flux by applying a dipole-like magnetic field. The Particle-in-Cell method was able to reproduce experimental observations like the heat-flux reduction. An additionally implemented optical diagnostics module allowed to confirm the results of the spectroscopy done during the experiment. The underlying effect that is responsible for the heat-flux reduction was identified as a coupling between the modified plasma and the dominating neutral flux component. The plasma, that is guided towards the target, act as a shield in front of the target surface for arriving neutrals. These neutrals are slowed down by charge-exchange collisions. Furthermore the magnetic field induces an increased turbulent transport that is also needed to reach a reduction in heat-flux. The turbulent transport was also obtained by three-dimensional Direct Simulation Monte Carlo simulations. Unfortunately, such source driven turbulence can not be expected in

space, so that a heat flux reduction in real space applications is questionable. Nevertheless, other effects like the induced turbulence by the rotating vehicle can compensate the missing source driven effect.

The second scenario in which a magnetic field is used to modify the heat flux of a plasma is the operation of the pulsed cathodic arc thruster. The same Particle-in-Cell code was used to simulate a typical pulse of this newly developed thruster of Neumann Space Pty Ltd. The typical behavior of the thruster could be reproduced numerically. The thrust is mainly produced by fast electrons. These electrons are accelerated by electric fields as a result of a plasma-beam instability. This plasma-beam instability was verified by a phase space diagnostics for the electrons. To demonstrate the influence of the magnetic field a simulation of the cathodic arc thruster without magnetic field and one with magnetic field were compared. It was shown that the use of a magnetic field leads to a ten times larger thrust by directing the heat flux. The resulting narrow plume is an additional advantage of the particle guiding magnetic field. This narrowness of the plume reduces the danger of interaction with other components of the space vehicle.

Both scenarios demonstrate the different capabilities for electromagnetic fields to manipulate plasmas and especially the corresponding heat-flux with respect to certain tasks. The possibilities range from reducing the heat-flux onto a target to maximizing the thrust by directing the heat-flux.

This thesis demonstrates that simulations are a great tool to support experiments and to deliver an improved physics understanding. They help to identify the basic physics principles in the different systems, because they can deliver information not accessible to experiments. In particular, a better understanding of the influence of electromagnetic fields on the heat-flux distribution in space-relevant applications was obtained. This can be the basis for further simulation-guided optimization, e.g. for the design of more effective cathodic arc thrusters. Here, the goal is to minimize costs for prototypes by replacing the hardware by virtual prototypes in the simulations. This allows to test basic design ideas in advance and get more highly-optimized designs at a fraction of time and costs.

Contents

1 Motivation

When on the 12th of April 1981 the Columbia space shuttle was started to its first flight, a milestone in astronautics was reached. It was the first space flight of a reusable space vehicle. One of the main factors that made this possible was the newly developed thermal protection system (TPS). TPSs include all features that protect the space craft from aerodynamic heating during its high-speed travel through planetary atmospheres. Most of the heat that is created during re-entry comes from compression of the air ahead of the hypersonic vehicle, as a result of the basic thermodynamic relation between temperature and pressure. The shock front building up in front of the vehicle deflects most of the heat and prohibits the surface of the space shuttle from direct contact with the maximum flux. Therefore, the main mechanism of heating up the surface is convective heat transfer between the shock wave and the surface of the vehicle. For reusable space shuttles the TPS is the most expensive part in terms of money and workload. State of the art spacecrafts use highly developed materials like ceramics to handle the enormous heat. Large efforts are made to develop and use these special materials for the TPS [1]. Beside developing new materials, an alternative ansatz to reduce costs is to use magnetic fields for heat-flux reduction. This would allow the use of cheaper materials and thus reduce costs for the whole space mission. In 2002 the European Space Agency (ESA) started an investigation of heat-flux mitigation by electromagnetic fields using partially-ionized plasmas [2]. The goal of the experimental campaign was to verify the potential of magnetic fields to modify particle and heat flux distributions on a target. The ability of manipulation of plasmas is a well-known and often used application for electromagnetic fields. One of the most famous examples may be fusion as a potential future energy source, where a hot plasma is trapped inside a vessel by utilizing closed magnetic field lines. In contrast to that, the scenarios presented in this thesis deal with much colder plasmas and use magnetic fields to influence these plasmas with the main goal of optimizing the heat flux distribution.

It is a major task for physicists to find explanations about the underlying physical effects of observations. One possible tool to achieve this are computer simulations. Simulations try to use models to reproduce real experiments numerically and in the best case provide ideas for potential improvements. For example simulations were used to optimize the design of vacuum vessels for thruster testing on earth, which is presented in publication [P7] in the Appendix. Here, baffles in the vessel at the wall were utilized to reduce back-fluxes of sputtered particles. These particles can be redeposited inside the thruster channel and lead to conducting surfaces. Consequently, due to the modified geometry by the deposited particles the performance of the thruster is affected.

In this thesis two simulations of experimental scenarios will be described in which a plasma flow and its resulting heat flux is affected by an externally applied magnetic field.

The first one is an experiment in which an arc jet was used to create a strong heat flux from a fast particle flow of neutrals, electrons and ions onto a target. The experiment demonstrates the possibility of reducing the heat-flux onto a target surface using magnetic fields. Applying a dipole-like external magnetic field, a strong heat-flux mitigation was observed [2]. Even up to now the experiments could not be reproduced by models based on Navier-Stokes fluid codes for neutrals including simplified plasma models. One was not able to explain the main effects leading to the heat-flux reduction. In this work a Particle-in-Cell code is used to attack this problem and suggest possible explanations of the experimental findings. The results of the simulation are reported in [P1] and [P2] of the Appendix and will be summarized in chapter 3.

The other scenario, which will be investigated using the same code, is the Pulsed Cathodic Arc Thruster. This is a novel kind of electric thruster, developed by Neumann Space Pty Ltd [3]. Pulsed cathodic arcs are low voltage, high current discharges at low pressure that ablate and ionize cathode material and then accelerate that material away from the cathode surface [4]. This results in a partially-ionized plasma being ejected from the cathode and directed downstream at high velocity [5]. Such devices are used for ion implantation and surface modification in industry, in applications ranging from the creation of hard films on the surface of tools to altering the bioactivity of polymer surfaces [6], [7]. An application which has been of interest in recent years is that of spacecraft propulsion, where the high ion velocity implies that a flight-rated pulsed arc thruster could operate at specific impulses far greater than current technologies [3], [8], [9]. Electromagnetic fields for such thrusters are used to guide the plasma downstream and squeeze the plasma into a narrow beam. In the frame of this thesis it will be studied how the magnetic field of such a thruster is used to influence the fast particle flux and consequently the heat flux. In contrast to the first application, where the magnetic field is used to minimize the heat flux onto a target, the magnetic field is used here to maximize the particle flux, the energy flux and consequently the thrust of the cathodic arc thruster.

Both scenarios will be studied using a Particle-in-Cell code including Monte-Carlo collisions. Particle-in-Cell is a simulation method to model plasmas in a fully kinetic description. This is necessary due to the non-Maxwellian characteristics of the plasma species. Particle-in-Cell codes were already used for various research topics of plasma physics including low temperature plasmas in laboratory and industry. Therefore, they are well-suited for both scenarios discussed in this thesis and allow to get a deeper understanding of how magnetic fields can be utilized to influence the heat flux distribution of partially-ionized plasmas in space-relevant applications.

2 Basics

In this chapter the methods used for the simulation will be introduced and explained.

2.1 Particle-in-Cell Method

The well-established Particle-in-Cell method combined with Monte-Carlo collisions (PIC-MCC) is a powerful tool for simulations of plasmas. In plasma physics PIC is a widely accepted and applied method to obtain a better understanding of the basic physics mechanisms of different systems. PIC-MCC provides full insight for all microscopic and macroscopic parameters. In particular, entities like electrostatic potential, densities, temperatures, velocity distribution functions and power fluxes can be calculated. A more detailed description of the PIC-MCC method itself can be found in several reviews [10], [11].

PIC is a self-consistent method to follow particles in velocity and position space by solving the Boltzmann equation

$$\frac{\partial f_s}{\partial t} + \vec{v}\frac{\partial f_s}{\partial r} + \vec{a}\frac{\partial f_s}{\partial v} = \left(\frac{\partial f_s}{\partial t}\right)_{coll} \tag{2.1}$$

with the collision operator $\left(\frac{\partial f_s}{\partial t}\right)_{coll}$. f_s is the distribution function of a specific particle species. In the limit of small timesteps equation (2.1) can be written as the following linearized equation:

$$f_s(x, v, t + \Delta t) = (1 + \Delta t I)(1 + \Delta t D) f_s(x, v, t) \qquad . \tag{2.2}$$

The two operators are defined as

$$D(f_s) = -\vec{v}\frac{\partial f_s}{\partial r} - \vec{a}\frac{\partial f_s}{\partial v} \tag{2.3}$$

$$I(f_s) = \frac{\partial f_s}{\partial t}_{coll} \tag{2.4}$$

For a collisionless plasma the equation can be simplified to applying only the operator $(1 - \Delta t D)$ on the distribution function f_i. This is equivalent to the Vlasov equation

$$\frac{\partial f_s}{\partial t} + \vec{v}\frac{\partial f_s}{\partial r} + \vec{a}\frac{\partial f_s}{\partial v} = 0 \qquad . \tag{2.5}$$

The PIC method is an exact solution for this equation [12].

The large amount of particles ($\geq 10^{12}$) in a real system prohibits to use direct particle models with full particle-particle interactions like in Molecular Dynamics. The well-known N^2 scaling of these interactions makes it impossible for simulations to resolve all Coulomb-interactions between all particles. Due to the electrical screening of plasmas on the Debye length scale it is sufficient to solve the Poisson equation on a grid with N_g cells and a cell size of about the Debye length. To compute the potential ϕ at a position $\vec{r}$ given by the Poisson equation

$$\Delta\phi(\vec{r}) = -\frac{\rho}{\epsilon} \tag{2.6}$$

only charge densities ρ in each cell have to be known. There are different methods to solve the resulting matrix equation. As shown in [P4] of the Appendix the backsolve for the LU decomposition provides a fast and efficient possibility for sequential code structures and small domain sizes. Here, the LU decomposition has only to be computed once, because the discretization of the Laplace operator never changes over the PIC cycle. It depends only on the metric coefficients. For larger grids the memory requirements no longer allows to store the LU matrices. Here, the successive-over-relaxation (SOR) method is an alternative giving a chance to make use of massive parallelization. In [P4] assets and drawbacks of both methods are presented.

To reduce the computational costs and make PIC simulations manageable for computers, one uses so-called "super particles", which represent a certain number of real particles.

Instead of solving the equations of motion

$$\begin{aligned}\dot{\vec{x}} &= \vec{v} \\ \dot{\vec{v}} &= \frac{q}{m}\left(\vec{E} + \vec{v} \times \vec{B}\right)\end{aligned} \tag{2.7}$$

for every particle, they are solved only for every super particle. In (2.7) $\vec{x}$ denotes the position of a particle, $\vec{v}$ is its velocity, m its mass and q its charge. $\vec{E}$ and $\vec{B}$ are the electric and the magnetic field at the position of the particle. The ansatz of super particles is possible, since all real particles within one super particle have the same charge to mass ratio as the resulting super particle. Therefore, the super particle follows the same trajectory as the solution of (2.7) like a single particle. In the electrostatic approximation magnetic field effects are included in the Lorentz force, but are determined just by their external sources (e.g. magnets). For the scenarios described in this thesis corrections from plasma currents can be neglected as the internal magnetic field is several orders of magnitude smaller than the external field.

Using equation (2.2), a collision probability for each particle and collision type is needed. Therefore, particle collisions are handled by Monte-Carlo collisions (MCC) routines. If a collision occurs particle velocities are changed according to the collision dynamics. In order to simulate systems with non-Maxwellian distribution functions one should include a collision model, which does not rely on the shape of the distribution function of charged particles. For this purpose a binary collision model was implemented, similar to that first proposed by Takizuka and Abe [13] for Coulomb collisions. In this model, particles are collided by randomly picked pairs. The velocities of particles after collisions are obtained using a Monte-Carlo technique: scattering angles are chosen randomly from a certain distribution of angles.

Beside the Coulomb collisions several other atomic processes like electron-neutral elastic collisions, ionization, excitation, neutral-neutral collisions and charge-exchange collisions are necessary to achieve an accurate self-consistent plasma simulation. All these collision types are implemented following the models of [14] and [15]. Particles in one cell are divided into pairs randomly. The probability for particle α to collide with particle β is calculated as:

$$P_\alpha = 1 - \exp\left(-v n_\beta \sigma(E)\right) \tag{2.8}$$

with v the relative velocity of both randomly chosen particles, n_β the density of particle species β, and $\sigma(E)$ the energy dependent cross-section for the given type of collision.

Whether a collision has to be executed or not is obtained using a Monte-Carlo technique representing the collisions probability. If the collision takes place, the collision dynamics is performed taking into account the relative velocity angles of both particles. The positions of both particles are not influenced by any collision.

To ensure physical correctness of the simulation, effects on the smallest length scale have to be taken into account, which is usually the Debye length $\lambda_{D,e}$. This requests a grid with cell sizes of $\Delta x \leq 0.5\lambda_{D,e}$ [11]. The smallest time step of interest in a plasma is the electron plasma frequency $\omega_{p,e}$. So the time step of the simulation is restricted by $\Delta t \leq \frac{2\pi}{\omega_{p,e}}$. Due to stability constraints a $\Delta t \leq 0.2\frac{2\pi}{\omega_{p,e}}$ is used for the integration of the equations of motion. In Figure 2.1 one cycle of the PIC algorithm is presented. To start, charge densities ρ are interpolated from the particle position $\vec{x}_i$ of particle i to the grid points x_j with $j = 1, \ldots, N_g$ using a weighting function. The electric potential ϕ_j on each grid point j is calculated solving the Poisson equation (2.6). This allows to calculate the electric field at the grid points. Afterwards, the same weighting function as before is used to interpolate the electric field back to the particle positions $\vec{x}$ to guarantee momentum conservation. If different weighting schemes for charge density deposition and electric field interpolation are used self forces might be created as shown in [11]. Now, the equations of motion (2.7) are solved for each particle. This subroutine is called particle mover or pusher. In the next step the algorithm allows to calculate particle losses and sources at the boundaries and in the next step all included types of collisions are executed. The next time step follows and again the particles are mapped to the grid for the calculation of the charge density. Typically the PIC cycle is repeated about 10^7 times before simulation reaches steady state for the scenarios presented in this thesis.

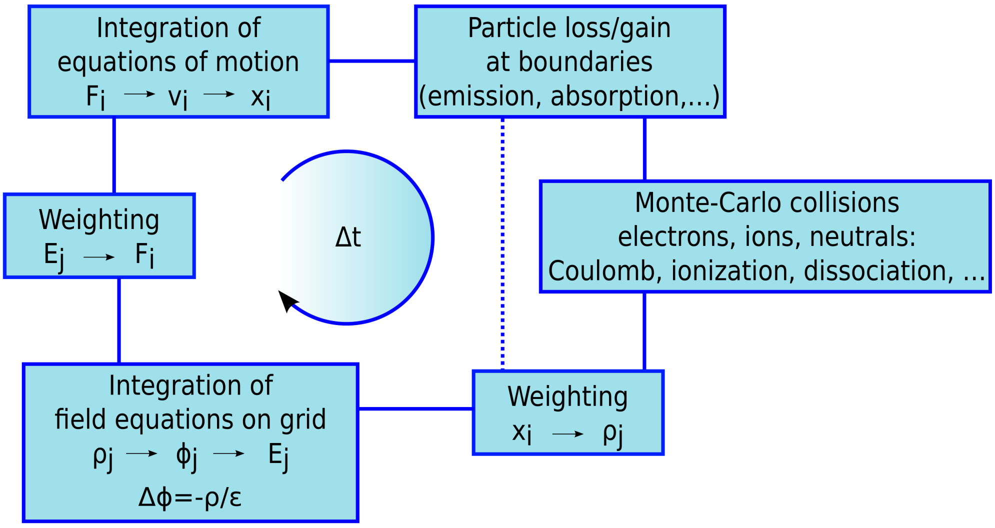

Figure 2.1: Scheme of the Particle-in-Cell method.

Neutrals are treated as plasma particles with zero charge. Technically, this is identical to a DSMC (Direct Simulation Monte Carlo) model for the neutrals.

2.2 Code Description

In this work a 2-dimensional axially symmetric PIC code with 3 dimensions in velocity space is used. The code only uses non-dimensional variables. Lengths are scaled to the Debye length as the smallest length scale. Times are scaled by the inverse electron plasma frequency as the smallest time scale of interest. This way one gets the following scaling:

$$\tilde{\Delta t} = \omega_{p,e} \Delta t = 0.2 \tag{2.9}$$

$$\tilde{\Delta z} = \frac{\Delta z}{\lambda_{D,b}} = 0.5 \tag{2.10}$$

Consequently, the velocities scale by:

$$\tilde{\Delta v_s} = v_s \frac{\Delta t_s}{\Delta z} \tag{2.11}$$

The subscripted s stands for each particle species. Ion's and neutral's movement are often not calculated at every timestep, since they are much slower than electrons. The so-called subcycling updates their particle positions after n steps of electron pushing. The subcycling factor is limited by the velocity of the respective species that has to be resolved.

Additionally, self-similarity scaling is applied to minimize numerical costs. To reduce the computational time the size of the system is scaled down by factor of ζ. In order to preserve the ratio of the charged particles mean free paths and the gyroradii to the system length L, the collision cross-sections σ and the magnetic field B are increased by the same factor ζ

$$L = \zeta L^* \qquad B = \zeta^{-1} B^* \qquad \sigma = \zeta^{-1} \sigma^* \qquad . \tag{2.12}$$

The primed entities represent the unscaled system. This reduces the computational costs, but keeps the relevant non-dimensional parameters of the system constant. These constant parameters are the Knudsen number for ionization and the Hall parameter for confinement. The Knudsen number is defined as the mean free path length of ionization collisions λ_{eN}

divided by a representative physical length scale of the system L

$$Kn \approx \frac{1}{n_N \sigma L} = \frac{\lambda_{eN}}{L} = constant \tag{2.13}$$

with n_N as the neutral density and σ as the cross-section for ionization. The Hall parameter β is the ratio between the electron gyrofrequency Ω_e and the electron-heavy particle collision frequency ν,

$$\beta = \frac{\Omega_e}{\nu} = \frac{eB}{m_e \nu} = constant \tag{2.14}$$

with e as the elementary charge, B the magnetic field and m_e the electron mass.

2.3 Optical Emission Spectral Analysis

In addition to the diagnostics provided directly by PIC such as densities, velocities and potential, a new post-processing diagnostic tool was developed. To be able to compare optical measurements and spectroscopic analysis with the simulation an optical emission diagnostic was implemented. It simulates the optical emission, similar to a photo observation in the experiment. Therefore, in every cell a spectrum of possible emission lines is calculated. The Open-ADAS library [16] provides photon emissivity coefficients (PEC), which are density and temperature dependent. An example for a dataset of PECs for a specific emission line at 562.68nm is shown in figure 2.2. This line can be assigned to a red color in the visible light spectrum, which is similar to the color from the photos of the experiment. These PECs are effective coefficients resulting from collisional radiative models. Such a model solves the equilibrium equation of excitation and disexcitation. It can also include residence

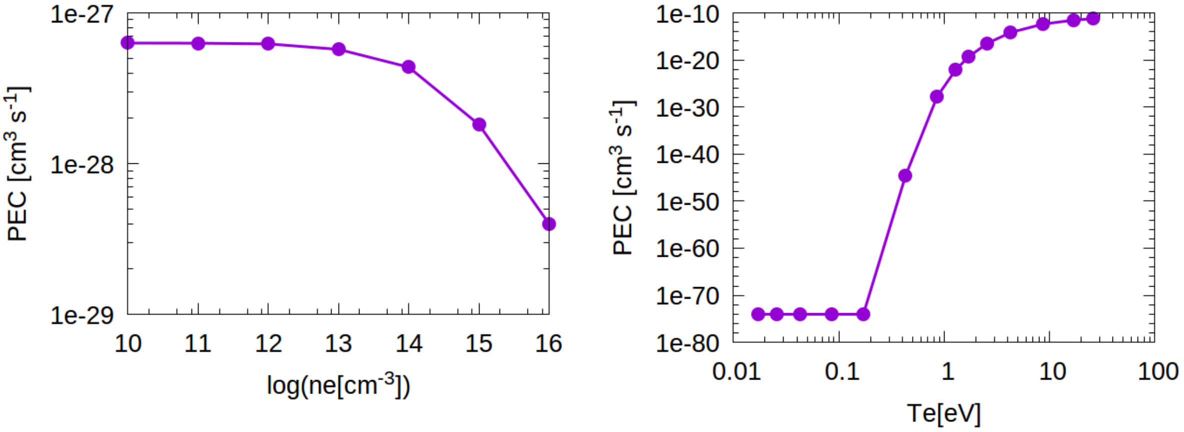

Figure 2.2: PEC dataset for 562.68nm emission line in Argon spectrum.

time effects of particles as a simple representation of transport, what can be expressed by

$$n_e n_{Z-1} S_{Z-1} - n_e n_Z S_Z + n_e n_{Z+1} \alpha_{Z+1} - n_e n_Z \alpha_Z - n_z/\tau_Z = 0 \tag{2.15}$$

with ionization rates S and recombination rates α. n_Z is the ion density of the ground state and τ_Z is the residence time of ions in the plasma. One is able to neglect the transport term when the timescale of the excitation process is much smaller than the transport time. This results in the coronal equilibrium for low densities. Here, the PECs get density independent as one can see in figure 2.2 for densities lower than 10^{13}cm^{-3}.

Using the PECs provided by the Open-ADAS library and the results of density and temperature from PIC-MCC one is able to calculate an intensity for each spectral line in every grid cell. Afterwards this can be used to calculate an RGB value that can be assigned to a color for every simulated cell and a brightness value according to the intensity. Collecting all cells results in a simulated photo of the scenario that can be compared with movies and photos from the experiment. A detailed description of the implemented optical emission spectral diagnostic is given in [P1] of the Appendix.

3 Simulation of Heat-Shield Experiment

The following chapter summarizes the results of the publications [P1] and [P2] in the Appendix, in which the mitigation of heat fluxes onto a target using magnetic fields was studied.

3.1 Motivation

Since the 1950s researchers tried to use electromagnetic fields for active control of aerodynamic flows [17]. Resler and Sears mentioned in their publication a heat-transfer reduction of neutral gas and plasma flows in contact with walls by applying magnetic fields. This effect is of particular interest for thermal protection of spacecrafts during planetary-atmosphere re-entry. The thermal protection system (TPS) of spacecrafts is one of the most expensive parts during space missions. Large efforts are done to develop and use special materials for the TPS [1]. One idea is to use magnetic fields for heat-flux reduction. If it is possible to reduce the heat-flux by externally applied electromagnetic fields, one will be able to use simpler and cheaper materials. In 2002 the thermodynamics section of the European Space Agency (ESA) initiated research activities on the electrodynamics heat-shield concept by EADS-Astrium [2]. Of particular interest was the heat-flux mitigation by means of Magnetohydrodynamics (MHD) in partially-ionized argon. Argon was chosen as test gas to get a principal understanding of the physical effects in a simple test system, which was required by the ESA. Argon was used due to its chemical inertness. This avoids the complex chemical processes of the atmosphere and allows computational analysis without focusing on various types of chemical reactions. The main goal of the campaign was to study the influence of electromagnetic fields on the heat transfer to a body interacting with hypersonic flows.

The main component of the test facility was an arc jet that is able to create a hypersonic flow field. The created hypersonic argon flow streams onto a blunt-body target made of quartz that mimics the spacecraft during the re-entry phase. Quartz is used as a reasonable-priced alternative to the dielectrics that were attached in TPS of spacecrafts.

The heat-flux on the target surface was measured without magnetic field as reference using infrared spectroscopy. Afterwards the coils inside the target are activated and create a dipole-like magnetic field. The intensity of this magnetic field could be varied by adjusting the electric current. Now, the heat flux is measured again and is compared with the reference measurement.

Photographs from the experiments for the case without magnetic fields are shown in Figure 3.1.

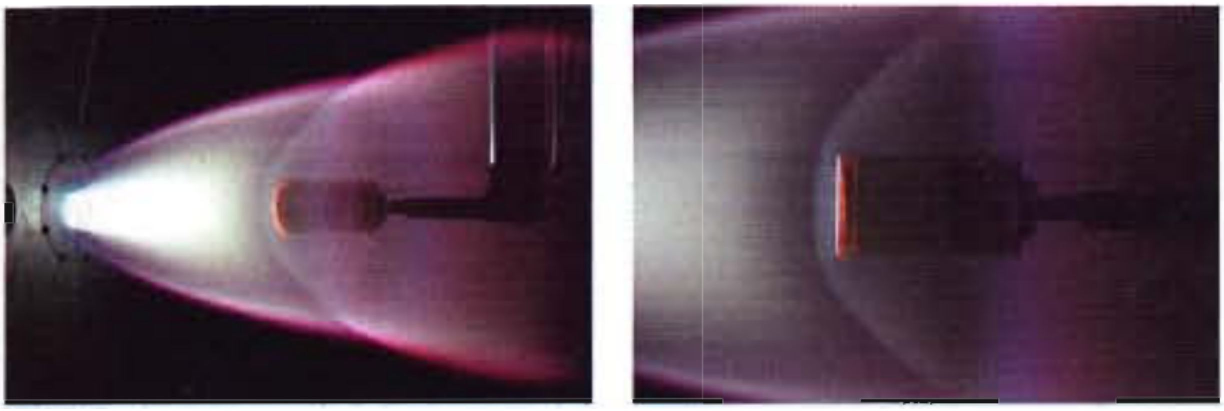

Figure 3.1: Photograph of the model during experimental tests [2] (the right one shows an enlarged view of the shock layer).

The magnetic field modifies the transport of ions and electrons in the plasma and leads to a change in the flow field. The main results of the experiments are the remarkable surface-temperature reduction of about 44% at the model and correspondingly derived heat-flux mitigation of 85% that occurred in the presence of an externally applied magnetic field [2]. Beside the shock cone and in front of the target additional emission regions appeared when applying the magnetic field. The additional emission regions are marked in Figure 3.2 with yellow and blue ellipses.

After this successful experimental campaign large efforts were invested to reproduce the results numerically. One major problem for the modelling is the lack of information about the plasma component in the experiment. There exist only average values for density ($n_e \approx 10^{11}\mathrm{cm}^{-3}$) and temperature ($T_e \approx 0.7\mathrm{eV}$), whereas the neutral component is really well characterized in terms of velocities, temperatures and densities. The average neutral density n_n is $\approx 10^{15}\mathrm{cm}^{-3}$.

In addition, spectroscopic data and a video from the experiment are available. The optical

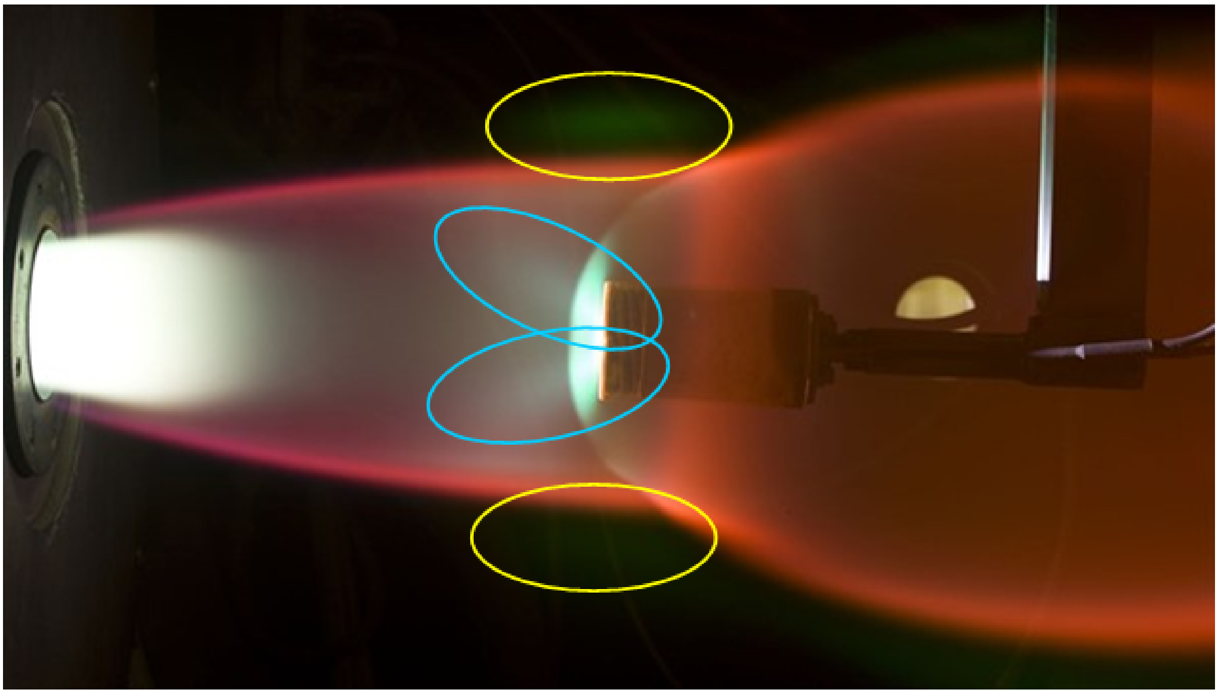

Figure 3.2: Experimental setup with additional emission regions marked in yellow and blue.

emission changed to a red colour when the magnetic field was applied, confirmed by observations by [18] in a similar experiment. The large bright area between the arc jet exit and the target shrank by activating the magnetic field and a small bright spot directly in front of the centre of the target appeared (see Figure 6 of [2]).

However, the experiments could not be reproduced by models based on neutral fluid codes with rather simplistic plasma models. One was not able to explain the main effects leading to the heat-flux reduction. One of the most challenging activities is the development of numerical algorithms to couple self-consistently equations describing non-equilibrium hypersonic-flows and Maxwell equations determining the electromagnetic field dynamics. As mentioned in [P2] collision mean free path lengths for electrons and ions are all similar or larger than the system length. Therefore, a Maxwellization of the plasma species can not be expected and a fluid model for the plasma is not able to reproduce the experiment sufficiently. Neutrals have such a high density that a Maxwell distribution is obtained by a large number of collisions and in principle a Navier-Stokes simulation is sufficiently accurate. Due to questions of simplicity in terms of implementation a DSMC description for neutrals is chosen, following the kinetic characteristics of the plasma model.

Especially energy fluxes and optical emission are determined strongly by fast tail electrons of more than 15eV and particularities of the non-Maxwellian velocity distribution functions are very important. Kinetic effects also play a crucial role in the plasma dynamics. Consequently, an existing Particle-in-Cell code with Monte-Carlo Collisions (PIC-MCC) is used for this study. For kinetic plasma simulations the Particle-in-Cell (PIC) method is very well suited. A detailed description of the method itself is given in section 2.1.

3.2 Simulation and Results

The spatial domain is two-dimensional using a cylindrical radial symmetric coordinate system. Cell size and time step are chosen in order to resolve the smallest length and time scales in the system. A detailed description of the domain is given in [P2].

For this scenario the code uses a self-similarity factor of 100 to reduce computational costs. The application of a self-similarity scaling is allowed for this scenario, because volume processes dominate over surface processes. Details of the scaling are reported in chapter 2. In the experiment neutrals and partially-ionized plasma from an arc jet source stream towards the blunt body in such a way, that ionization is very small. That means that the much larger density of neutrals is practically unaffected and decoupled from the plasma densities. Therefore, a higher super-particle factor for neutrals can be used compared to the plasma particles [P1].

The Finite-Element Magnetic Method solver (FEMM) [19] was used to calculate the magnetic field created by the coils inside the target. Its topology and the simulation domain are shown in Figure 3.3 from [P2].

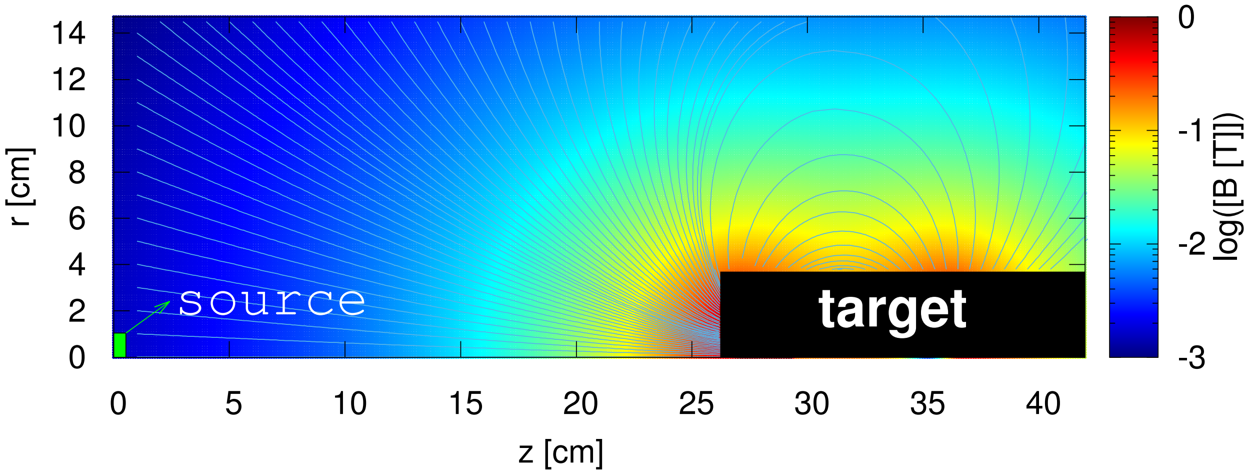

Figure 3.3: Magnetic field in the simulation domain [P2].

The particle source on the left side of the domain represents the fast particle beam from the arc jet consisting of neutrals, electrons and ions. According to the experiment neutrals have velocities of about 2000 m/s with a maximal injection angle of 12 degrees. Due to the restrictions in angular distribution predetermined by the experiment a correctly represented Maxwellian distribution is not possible. It limits the possible combinations of radial and axial velocities resulting in a hole in the distribution function. In addition there is the need for hot tail electrons being responsible for visible light emission. This is only achievable by electrons with a temperature higher than 15eV. Unfortunately, experimental characterization of the plasma distribution coming from the arc jet is lacking. Parametric simulation tests show that the best choice for the source distribution of electrons was to inject them with a bi-Maxwellian distribution, providing a cold background and a hot tail that is responsible for the optical emission by excitation collisions with neutrals [P2].

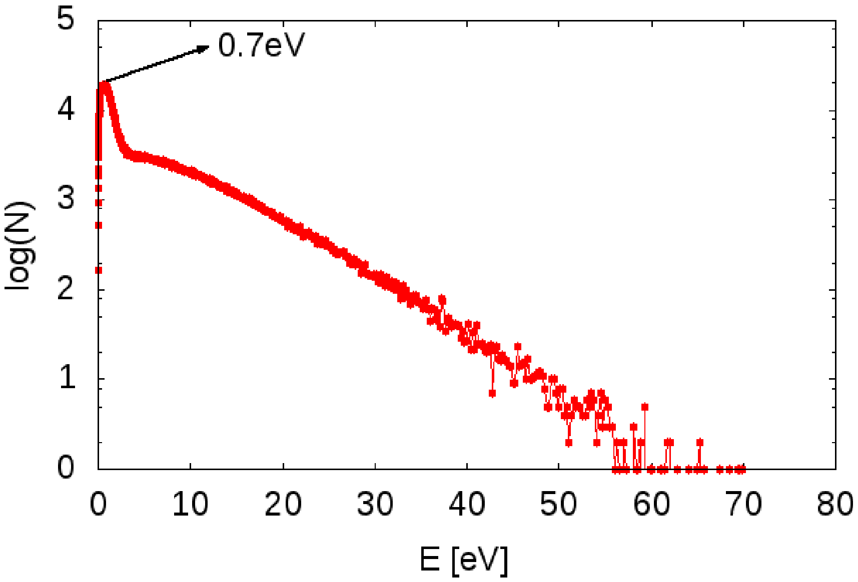

Figure 3.4: Electron energy distribution injected by the particle source [P2].

According to experimental measurements ions have a velocity distribution similar to the neutrals. Therefore, in the simulation the same parameters for the injection sources were used for both species.

During the experiment, strong fluctuations were observed when the magnetic field was applied [20]. This is motivated by the fact that the arc-jet itself delivers a turbulent flow due to angular gas insertion [21]. A three dimensional DSMC simulation was done to analyze the impact of this angular gas insertion. The streamlines in Figure 3.5 show the movement of markers distributed uniformly in the region of the particle source according to the fluid velocities calculated as velocity averages in the cells. The streaming neutrals form large convective cells that are typical for a strongly turbulent flow. Movies of the optical emission in the experiment indicate that this turbulence is strongly enhanced by the activation of

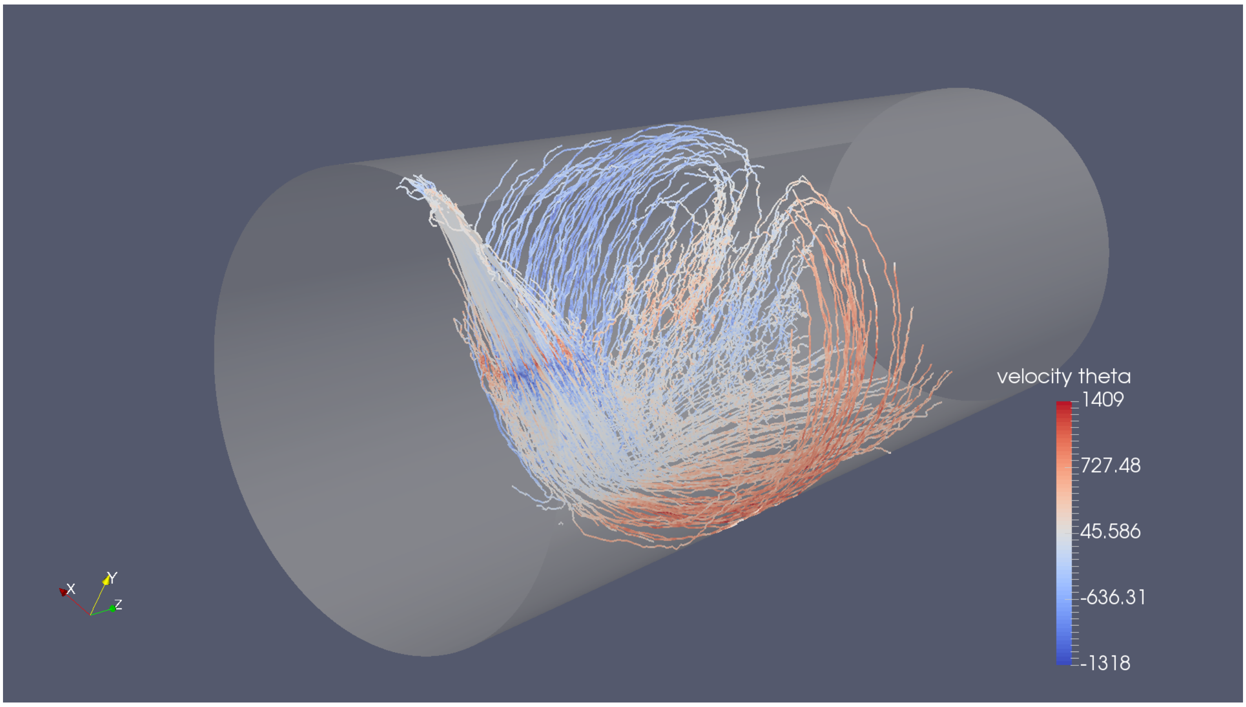

Figure 3.5: Streamlines as result of a 3D DSMC simulation of angular insertion into a cylindrical tube

the magnetic field. To take this into account, a radial diffusion model was implemented for the magnetized case. It is well-known that Huels-type arc heaters deliver a turbulent flow larger than the anomalous Bohm transport [21], [22]. This turbulent transport was implemented in a parametric form and adjusted to the experimental heat flux. Without activating the turbulence particle and heat flux will increase towards the center in contrast to the experiment. Turbulent transport is necessary to avoid this strong increase of heat flux.

The most important experimental finding was the strong heat-flux mitigation of 85% by applying the magnetic field [2]. Due to the large difference between plasma density and neutral density one can estimate that most of the heat-flux is carried by neutrals. Obviously, neutrals can not be affected directly by the magnetic field. Therefore, it is only possible to influence them via interaction with the plasma components which react to magnetic fields. As shown in [P1] and [P2] of the Appendix the PIC simulation is able to reproduce the effect of heat-flux mitigation qualitatively for the case when the magnetic field is applied. This effect is created by a combination of radial turbulent transport and collisions with plasma particles. The neutral flux is reduced indirectly.

The behaviour of the particles is sketched in Figure 3.6. Electrons follow the magnetic fieldlines, guiding them towards the target and build up a region of higher density in front

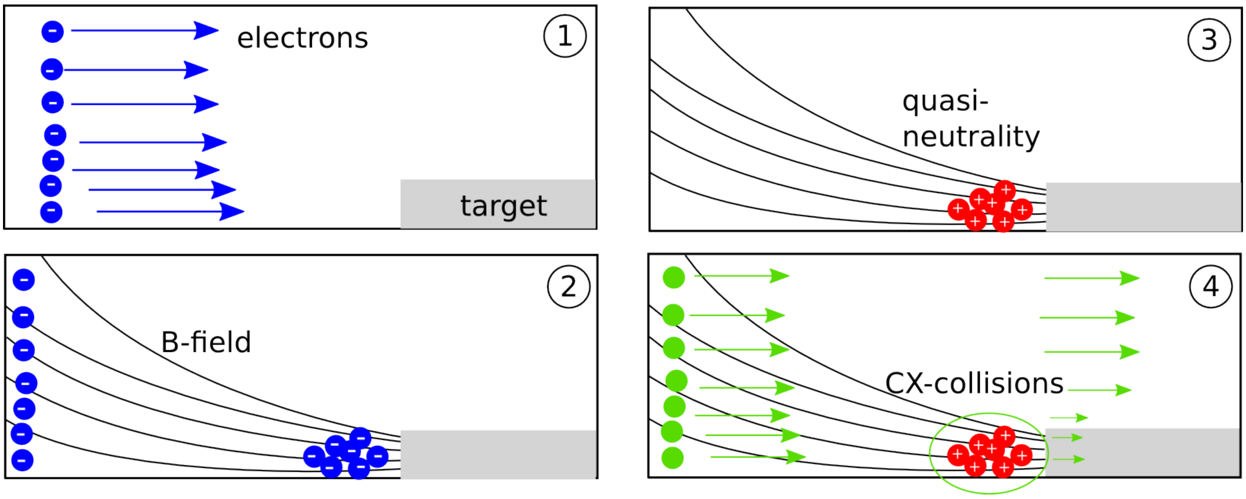

Figure 3.6: Schematic explanation of heat flux mitigation due to the effect of charge-exchange collisions.

of the target. This is shown in the second subplot of sketch 3.6. Ions follow due to the constraint of quasi-neutrality, see subplot 3 of Figure 3.6. If neutrals arrive in this region their velocity will be reduced by charge-exchange collisions with slower ions, compare subplot 4 of the sketch. The charge-exchange collisions act as a parallel momentum sink for neutrals slowing them down [P1]. It is shown in [P1] that an increased number of collisions with plasma particles lead to a loss in the energy and momentum of neutrals, mostly by charge-exchange collisions between neutrals and ions. This effect reduces the neutral energy flux to the target. Consequently, an overall reduction of heat-flux is observed as long as the plasma heat flux is not too strongly increased. For a mitigation of the total heat-flux a high density plasma is needed, acting as a shield against the streaming neutrals by charge-exchange collisions. However, this density should not get too large, otherwise the plasma fluxes reaching the target will increase and get dominant. In such situations with a dominant plasma flux the modified transport by magnetic field and an induced turbulence do not guarantee a reduction of the total heat flux to the target. The neutrals experience still a slowing down in front of the target, but the increased fluxes of hot electrons and fast ions create an increase of the total heat flux.

An example for the sensitivity of the results is shown in Figure 3.7. For comparison two combinations of diffusion coefficients for neutrals and plasma are shown. As expected the largest heat-flux reduction is obtained for the largest diffusion coefficient for neutrals, because this distributes the heat flux radially reducing also the peak value in the center. It is very interesting that it is already sufficient to raise only the diffusion coefficient for the plasma species to get a heat-flux reduction in comparison to the results with a diffusion coefficient of $10\text{m}^2/\text{s}$ for all species, where even a large increase of the heat-flux is observed. This proves the strong coupling between neutral and plasma species and its significance to achieve a heat-flux mitigation. Diffusion coefficients of about $1000\text{m}^2/\text{s}$, necessary to get a heat-flux mitigation, are so extremely high, that this can only be interpreted as an overall change in the source distribution from the arc jet. This is not linked with transport physics induced by the applied magnetic field. This means that the applied magnetic field seems to, directly or indirectly, influence the arc jet source which then modifies the experimental target conditions. The induced effect of profile smoothing by CX-collisions is a new finding of this study. This explains the observed reduction of the total heat-flux by magnetic field effects, which affects only charged particles.

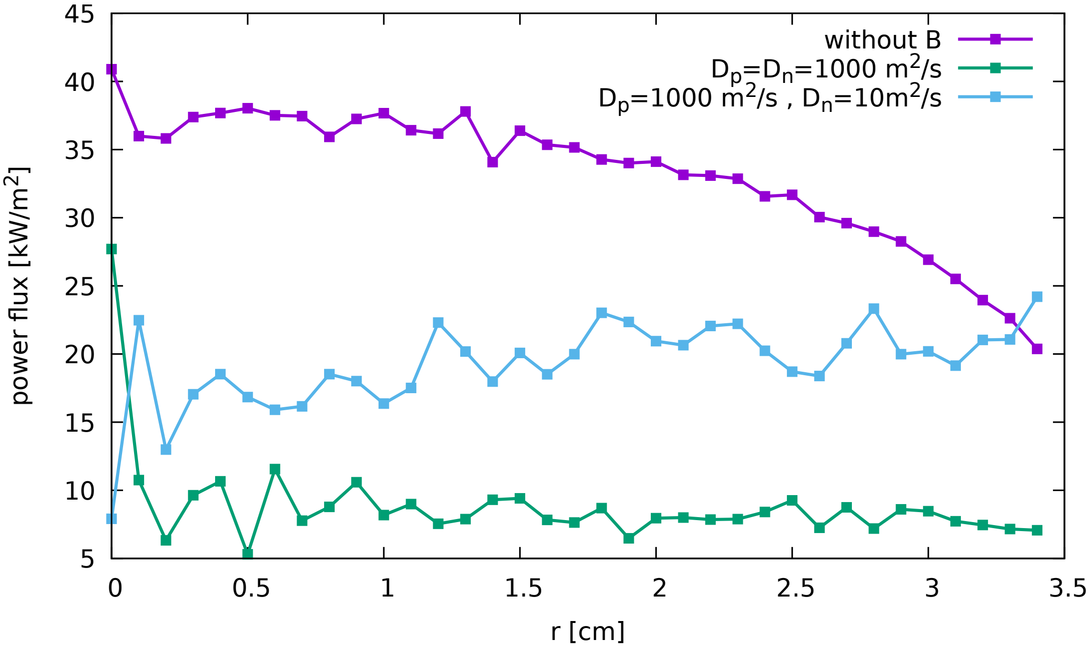

Figure 3.7: Simulated heat-flux without magnetic field in comparison with magnetic field and different combinations of diffusion constants for plasma D_P and for neutrals D_n.

For an application of the concept of magnetic field reduction for heat fluxes in re-entry scenarios the coupling of plasma and neutral channel by CX-collisions is also possible. If a reduction of the incoming heat-flux will be possible in re-entry is not guaranteed. In the experiment the tilted injection of neutrals in the arc jet induces strong turbulence also coupled to the plasma. This could be possible e.g. by induced turbulence from the rotating vehicle.

Beside the standard PIC diagnostics like density, potential and velocity an optical emission spectroscopy diagnostics tool was developed and presented in [P1]. It provides the emission spectrum for every calculation cell. One can compare simulation results with spectroscopy data and photos from the experiment. An additional diagnostic module allows to calculate an intensity for each wavelength in the ADAS database [P1]. Using the results of the diagnostics an optical spectrum for each cell is obtained. Emission in the optical range allows to convert wavelengths and intensities into specific colors and brightness for each simulation cell. This simulated optical emission can be compared with photos from the experiment. They reproduce the shift to more reddish colors when the magnetic field is applied. In addition, in the experiments with applied external magnetic field the intensity in various lines of the spectrum was decreased in the free stream region. This can be explained by a shift of the electron density back towards the source that was observed during simulation and experiment when applying the magnetic field.

The calculated spectra of a cell in the free stream region is shown in Figure 3.8. In accordance with the experiment, simulations show a push-back of the region of high electron density away from the target. This results in shrinking of the bright emission region in the free stream as known from the experiment [2]. In addition, in front of the target a region of higher density occurs when the magnetic field is applied. Due to the magnetic field a magnetic mirror builds up in front of the target. Consequently, more electrons are accumulated there,

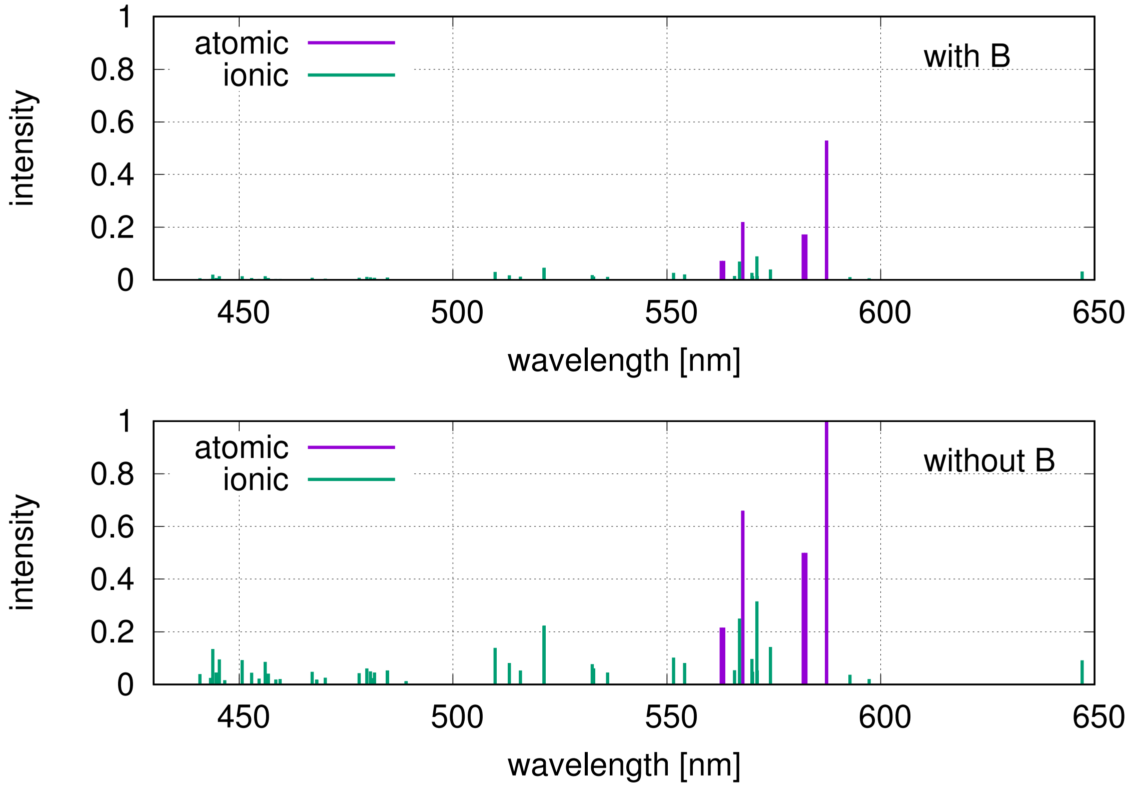

Figure 3.8: Simulated optical emission spectra in the shock front region, (a) with magnetic field and (b) without magnetic field [P1].

resulting in a density peak. This explains why experimentally an additional bright emission region near the target appears when the magnetic field is applied [P1].

3.3 Subsummary

Magnetic fields are used to manipulate a plasma so that in this case the heat flux onto a target can be reduced, which is an attractive approach for re-entry of spacecrafts. Particle-in-Cell simulations show that it is also possible to influence even a strong neutral channel. Collisions between plasma particles and neutrals trigger a coupling between both. Consequently, by affecting the plasma also the neutral channel is affected and the neutral flux is reduced as well. Beside the collision coupling the Particle-in-Cell simulation allowed to identify turbulence as a major reason for the heat-flux reduction. Unfortunately, this turbulence is driven mainly by the arc jet acting as particle source. This could be possible in a re-entry scenario e.g. by induced turbulence from the rotating vehicle.

4 Simulation of Cathodic Arc Thruster

In the previous chapter a magnetic field was used to minimize experimentally the heat flux onto a target. Here, a scenario will be described in which a magnetic field is used to maximize the extracted heat flux and by this the thrust for an ion thruster. All results of this study are reported in detail in [P3] of the Appendix.

4.1 Motivation

Since the 1960s electric propulsion systems were used on a large number of spacecraft missions. Beside the commercial use of such thrusters also the research for new concepts was enforced in the past. It became popular to support the industrial design optimization of thrusters also by simulation. Nowadays, there exist various types of ion thrusters that follow different concepts for how to accelerate a spacecraft. One example for such a thruster is the Highly Efficient Multistage Plasma Thruster (HEMP-T). Different aspects of the HEMP-T were studied by simulations like the ion angular distribution [P5] or the influence of different electron source locations [P6]. One recent type of thruster that was developed by Neumann Space Pty Ltd. is the cathodic arc thruster [3]. Cathodic arc thrusters are low voltage, high current discharges which erode the solid cathode material. Afterwards, the ablated material is ionized and accelerated away from the cathode, producing the thrust. The thruster itself, including the ion production is described in several publications from Neumann et al. [3], [8]. The simulations done in this thesis help to clarify the underlying physical mechanisms that play a key role during the pulsed operation of such a thruster.

4.2 Simulation and Results

The same Particle-in-Cell code as for the heat-shield experiment is used to simulate the cathodic arc thruster. The simulation domain consists of the thruster on the left side including anode, cathode, cathode mount, trigger pin and the coils, forming the magnetic field. To the right there is a free stream region in which the plume plasma expands. The whole domain as it is used for calculations in [P3] of the Appendix is shown in 4.1. The colors in 4.1 denote the strength of the magnetic field, which is created by the set of magnetic coils.

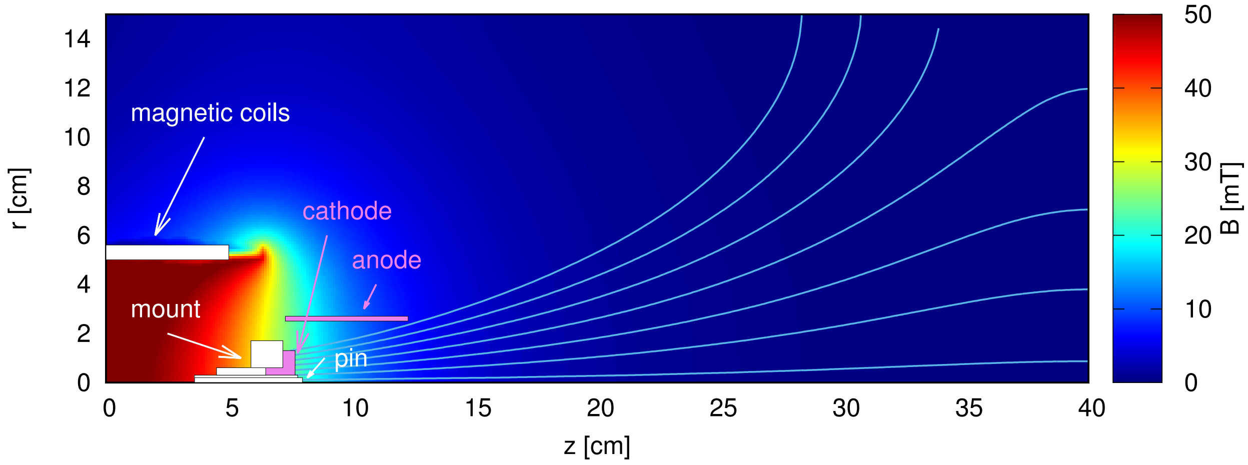

Figure 4.1: Magnetic field and simulation domain [P3].

The thruster works also without an applied magnetic field, but the magnetic field traps the plasma close to the symmetry axis, thus narrowing the plume plasma. For thrusters this is a big advantage due to higher efficiency of the directed beam and smaller particle fluxes to other parts of the satellite.

The simulation of the Pulsed Cathodic Arc Thruster starts with a phase in which −220V are applied at the cathode. The voltage is chosen according to the experiment. A high-energetic electron beam is injected near the trigger pin with velocities directed towards the cathode. The energy is chosen in such a way that despite moving towards the negative potential electrons are able to reach the cathode. As explained in [P3] this initial phase of the arc is rather complex and its simulation is not done self-consistently. Impinging electrons at the cathode ablate neutrals from the surface and the outgoing neutrals are ionized by other beam electrons. This plasma is starting to build up in the first plots of Figure 4.2 that shows the electron and ion density of a typical pulse.

As explained in detail in [P3] of the Appendix fluctuations build up and electron blobs are ejected during a pulse contributing to the thrust. The fluctuations grow and lead to large

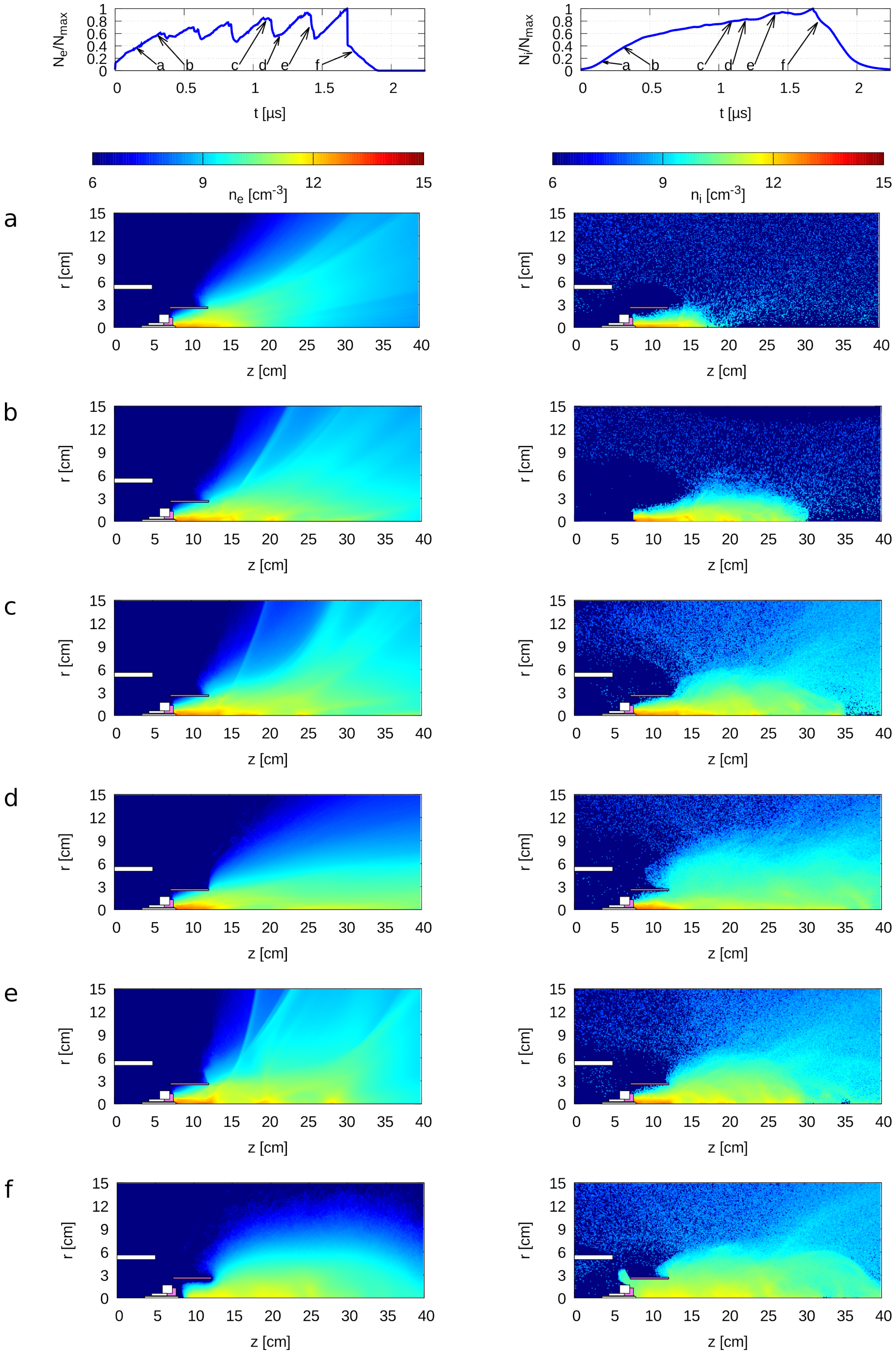

Figure 4.2: Electron (left) and ion (right) densities for different time steps of one pulse [P3].

electron blobs. In snapshot (d) of Figure 4.2 the size of the fluctuations has reached its maximum, producing also a maximum in the velocity of electrons leaving the thruster. At the end of the pulse after 2μs the potential is set to zero voltage at the cathode again and the particle injection is turned off. Consequently, even the bulk plasma is not trapped anymore and all plasma particles leave the thruster, producing maximum thrust (f). Details of the whole cycle of a pulse are described in [P3].

To identify the underlying effect that creates the large fluctuating electron blobs a phase space analysis was done. The corresponding plots for the same time steps as for the density diagnostic are shown in Figure 4.3.

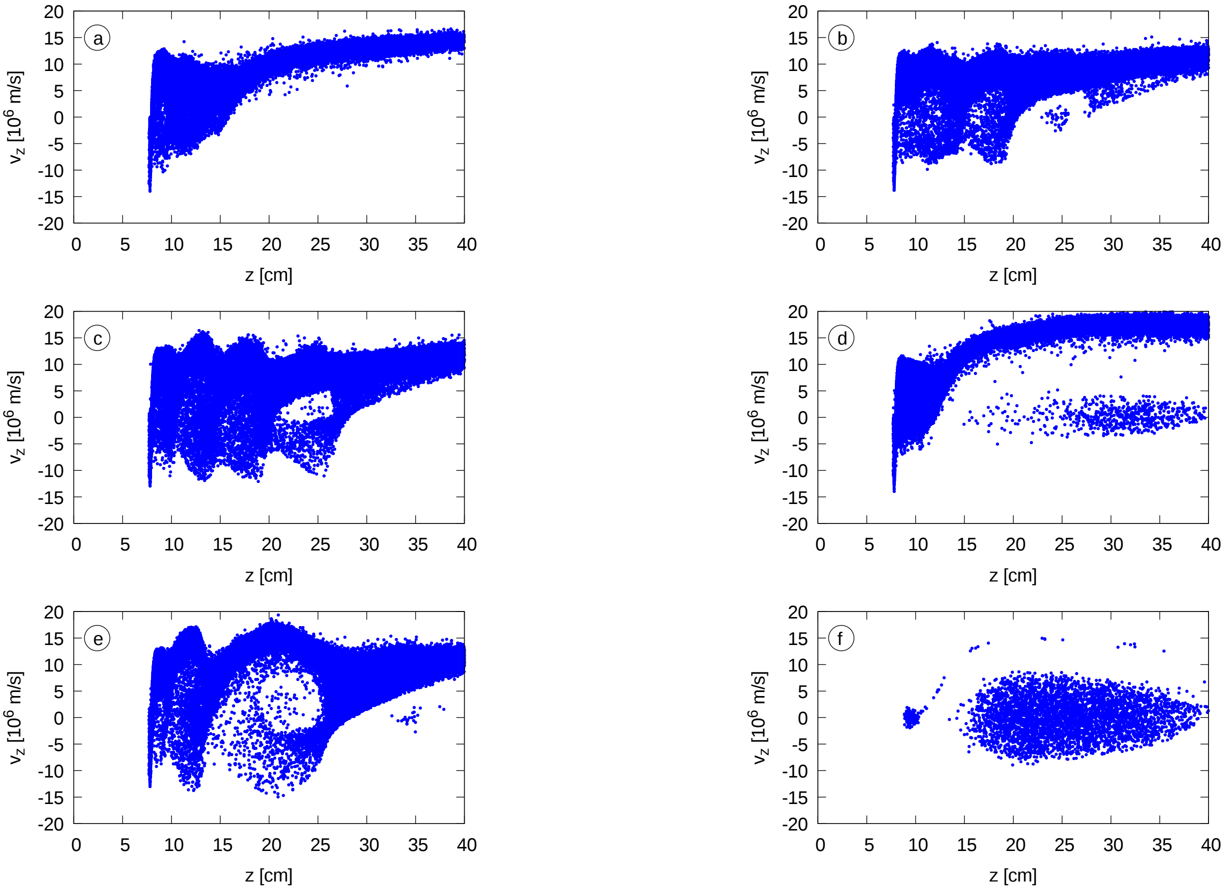

Figure 4.3: Phase space of axial velocity as a function of axial position for electrons at different time steps for one pulse [P3].

One can see that the plasma dynamics can be divided into two parts during the first phases of a pulse. Inside the thruster there is the plasma bulk, in which cold electrons are dominant. Beyond the thruster exit a fast electron beam is responsible for the thrust. In step (b) first eddies occur together with the density fluctuations. Such eddies are typical for a plasma instability. Analyzing the phase space distribution in detail it was possible to identify the instability as the well-known plasma-beam instability [P3], which is a special case of the two-stream instability. A cold, stationary background plasma interacts with a hot but low-density beam of electrons. The experimental situation was described first in 1925 by Langmuir [23]. A first kinetic theory of these unstable perturbations was developed by Bohm and Gross [24] analyzing their propagation along the beam direction. They found out that the instability is not an effect of collisions. It originates from electrical forces that couple particles with different velocities, resulting in groups of particles travelling with high velocities, similar to the density blobs visible in the density contour plots. Following the approach of Birdsall [10] analytic solutions can be derived. One can calculate the frequency of the instability, which agrees well with the frequency observed in the simulation of about $10^9 \mathrm{s}^{-1}$.

One other well-known effect of the plasma-beam instability is that large potential variations can occur. As described in publication [P3] electric fields of about 10^4kV/m are responsible for the large acceleration of electrons. Therefore, electrons with velocities of more than 10^7m/s are created and contribute mainly to the thrust. The simulations and the analytic estimates prove that the thrust production is dominated by the production of fast electrons by the beam-plasma instability producing density blobs. The thrust contribution of the eroded ions is a factor two smaller than the electron contribution.

The simulation is able to confirm several experimental findings of the cathodic arc thruster, especially a very narrow expansion plume as presented in publication [P3]. As mentioned before the magnetic field is used to maximize the thrust by narrowing the plume expansion. Therefore, the simulation was used to compare the operation of the thruster with and without magnetic field. The result of both scenarios is shown in Figure 4.4. Switching on the magnetic field leads to a thrust increased by a factor of 10.

In addition, it is obvious that the magnetic field amplifies the instability in the system and larger temporal variations in the thrust appear. This is helpful as larger variation leads to larger potential drops and consequently to larger electric fields. Therefore, electrons have the chance to accelerate to larger velocities and create higher thrust. The influence of the magnetic field strongly affects also the energy fluxes. The result is shown in Figure 4.5.

One can see that the magnetic fields leads to a peaked distribution of the energy flux at the axis, whereas without magnetic field a broad distribution exists. Integrating the energy flux radially, one gets a total heat flux leaving the thruster for the case without magnetic field of 60mW and 80mW for the case with magnetic field. Obviously, the total heat fluxes are not too different, but the thrust values vary from 1mN for the case without magnetic field to 10mN for the case with magnetic field, see Figure 4.4. This demonstrates, that the magnetic field optimizes thrust by concentrating the energy and particle fluxes axially. The similarity of the heat flux values and the large difference in thrust between the operation with and without magnetic field can be explained by the different impact of very fast electrons. The

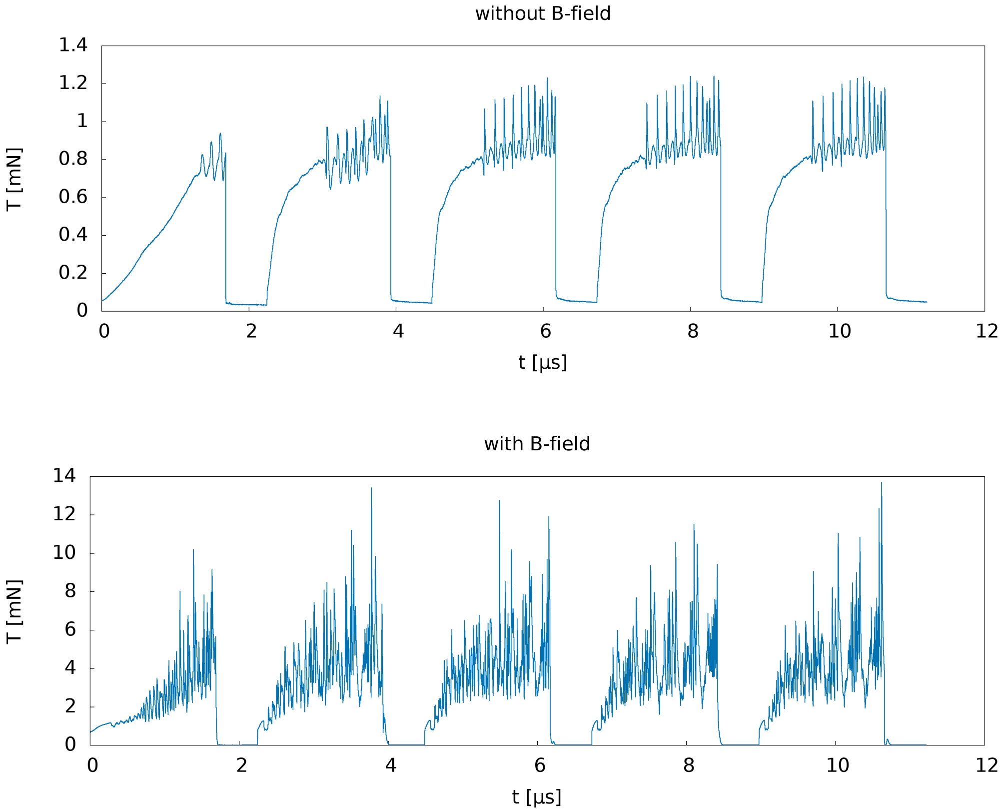

Figure 4.4: Thrust of the cathodic arc thruster without (top) and with (bottom) magnetic field.

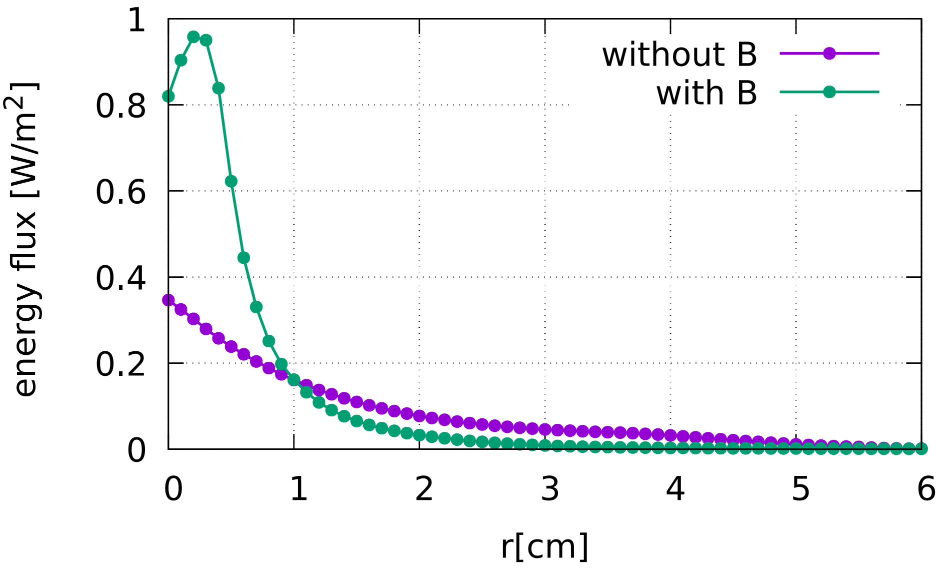

Figure 4.5: Energy flux of the cathodic arc thruster without and with magnetic field.

peaked radial profile in the electron heat flux in the case with magnetic field explains the large increase in thrust. This thrust is mainly carried by fast electrons accelerated by the large electric fields. These electric fields are a result of steep potential gradients created by the plasma-beam instability.

4.3 Subsummary

The Particle-in-Cell simulations were used to study the physical mechanisms that occur during a typical pulse of the newly developed Pulsed Cathodic Arc Thruster. The simulations reproduce the main experimental characteristics of a pulsed thrust that is mainly carried by the plasma. The simulation showed that mostly fast electrons and not ions are responsible for the thrust, which was not expected. Comparing the operation of the thruster without and with magnetic field demonstrated that the magnetic field guides and centers the energy and particle flux towards the symmetry axis. This results in a ten times higher thrust and a significantly narrower plume, which makes the Pulsed Cathodic Arc Thruster quite attractive for space missions.

5 Conclusions

Manipulating and utilizing plasmas becomes a more and more important task in various research fields of physics and in industrial developments. Especially in these days space-relevant applications there are different ideas to modify plasmas concerning particular tasks. One major point of interest is the ability to influence plasmas using magnetic fields. Two examples are discussed in this thesis.

To study the underlying physical effects that were achieved by these magnetic fields for both scenarios Particle-in-Cell simulations were done. The first example originates from an experiment performed by the European Space Agency (ESA) in collaboration with the German Space Agency (DLR). To verify the possibility of heat-flux reduction onto the thermal protection system of a space vehicle a simplified experiment on earth was developed. A partially-ionized Argon beam was used to create a certain heat-flux onto a target. The main finding of the experimental campaign was a large mitigation of heat-flux by applying a dipole-like magnetic field. The Particle-in-Cell method was able to reproduce experimental observations like the heat-flux reduction. An additionally implemented optical diagnostics module allowed to confirm the results of the spectroscopy done during the experiment. The underlying effect that is responsible for the heat-flux reduction was identified as a coupling between the modified plasma and the dominating neutral flux component. The plasma, that is guided towards the target, act as a shield in front of the target surface for arriving neutrals. These neutrals are slowed down by charge-exchange collisions.

Furthermore, the magnetic field induces an increased turbulent transport that is also needed to reach a reduction in heat-flux. The turbulent transport was also obtained by three-dimensional Direct Simulation Monte Carlo simulations. Unfortunately, such source driven turbulence can not be expected in space, so that a heat flux reduction in real space applications is questionable. Nevertheless other effects like the induced turbulence by the rotating vehicle can compensate the missing source driven effect.

The second scenario in which a magnetic field is used to modify the heat flux of a plasma is the operation of the Pulsed Cathodic Arc Thruster. The same Particle-in-Cell code was used to simulate a typical pulse of this newly developed thruster of Neumann Space Pty Ltd. The typical behavior of the thruster could be reproduced numerically. The thrust is mainly produced by fast electrons. These electrons are accelerated by electric fields as a result of a plasma-beam instability. This plasma-beam instability was verified by a phase space diagnostics for the electrons. To demonstrate the influence of the magnetic field a simulation of the cathodic arc thruster without magnetic field and one with magnetic field were compared. It was shown that the use of a magnetic field leads to a ten times larger thrust by directing the heat flux. The resulting narrow plume is an additional advantage of the particle guiding magnetic field. This narrowness of the plume reduces the danger of interaction with other components of the space vehicle.

Both scenarios demonstrate the different capabilities for electromagnetic fields to manipulate plasmas and especially the corresponding heat-flux with respect to certain tasks. The possibilities range from reducing the heat-flux onto a target to maximizing the thrust by directing the heat-flux.

This thesis demonstrates that simulations are a great tool to support experiments and to deliver an improved physics understanding. They help to identify the basic physics principles in the different systems, because they can deliver information not accessible to experiments. In particular, a better understanding of the influence of electromagnetic fields on the heat-flux distribution in space-relevant applications was obtained. This can be the basis for further simulation-guided optimization, e.g. for the design of more effective cathodic arc thrusters. Here, the goal is to minimize costs for prototypes by replacing the hardware by virtual prototypes in the simulations. This allows to test basic design ideas in advance and get more highly-optimized designs at a fraction of time and costs.

6 Bibliography

[1] M. L. Blosser, „Advanced metallic thermal protection systems for reusable launch vehicles“, in *Proceedings of the Space Technology and Applications International Forum*, 1997, pp. 1125–1143.

[2] Gülhan, Esser, Koch, Siebe, Riehmer, Giordano, and Konigorski, „Experimental verification of heat-flux mitigation by electromagnetic fields in partially-ionized-argon flows“, *Journal of Spacecraft and Rockets*, vol. 46, no. 2, pp. 274–283, 2009.

[3] P. R. C. Neumann, M. Bilek, and D. R. McKenzie, „A centre-triggered magnesium fuelled cathodic arc thruster uses sublimation to deliver a record high specific impulse“, *Applied Physics Letters*, vol. 109, no. 9, p. 094 101, 2016. DOI: `10.1063/1.4962124`. eprint: `http://dx.doi.org/10.1063/1.4962124`. [Online]. Available: `http://dx.doi.org/10.1063/1.4962124`.

[4] E. Hantzsche, „Mysteries of the arc cathode spot: A retrospective glance“, *IEEE Transactions on Plasma Science*, vol. 31, no. 5, pp. 799–808, Oct. 2003, ISSN: 0093-3813. DOI: `10.1109/TPS.2003.818412`.

[5] G. Y. Yushkov, A. Anders, E. M. Oks, and I. G. Brown, „Ion velocities in vacuum arc plasmas“, *Journal of Applied Physics*, vol. 88, no. 10, pp. 5618–5622, 2000. DOI: `10.1063/1.1321789`. eprint: `http://dx.doi.org/10.1063/1.1321789`. [Online]. Available: `http://dx.doi.org/10.1063/1.1321789`.

[6] R. Fu, S. Kwok, P. Chen, P. Yang, R. Ngai, X. Tian, and P. Chu, „Surface modification of cemented carbide using plasma nitriding and metal ion implantation“, *Surface and Coatings Technology*, vol. 196, no. 1, pp. 150–154, 2005, 13th International Conference on surface modification of materials by ion beams, ISSN: 0257-8972. DOI: `http://dx.doi.org/10.1016/j.surfcoat.2004.08.167`. [Online]. Available: `http://www.sciencedirect.com/science/article/pii/S0257897204007662`.

[7] M. Bilek, D. McKenzie, and R. Powles, „Treatment of polymeric biomaterials by ion implantation“, *Biomaterials and surface modification. Research Signpost, Kerala*, 2007.

[8] P. R. C. Neumann, M. Bilek, and D. R. McKenzie, „Optimising ion production in pulsed refractory and non-refractory cathodic arcs“, in *Proceedings of the 12th Asia Pacific Physics Conference (APPC12).* JPS Conference Proceedings, 2014, vol. 1, p. 015 059. DOI: `10.7566/JPSCP.1.015059`. eprint: `http://journals.jps.jp/doi/pdf/10.7566/JPSCP.1.015059`. [Online]. Available: `http://journals.jps.jp/doi/abs/10.7566/JPSCP.1.015059`.

[9] J. E. Polk, M. J. Sekerak, J. K. Ziemer, J. Schein, N. Qi, and A. Anders, „A theoretical analysis of vacuum arc thruster and vacuum arc ion thruster performance“, *IEEE Transactions on Plasma Science*, vol. 36, no. 5, pp. 2167–2179, Oct. 2008, ISSN: 0093-3813. DOI: `10.1109/TPS.2008.2004374`.

[10] Birdsall and Langdon, *Plasma physics via computer simulation.* CRC Press, 2004.

[11] Tskhakaya, Matyash, Schneider, and Taccogna, „The particle-in-cell method“, *Contributions to Plasma Physics*, vol. 47, no. 8-9, pp. 563–594, 2007.

[12] R. W. Hockney and J. W. Eastwood, *Computer simulation using particles.* CRC Press, 1988.

[13] T. Takizuka and H. Abe, „A binary collision model for plasma simulation with a particle code“, *Journal of Computational Physics*, vol. 25, no. 3, pp. 205–219, 1977.

[14] V. Vahedi, G. DiPeso, C. Birdsall, M. Lieberman, and T. Rognlien, „Capacitive rf discharges modelled by particle-in-cell monte carlo simulation. i. analysis of numerical techniques“, *Plasma Sources Science and Technology*, vol. 2, no. 4, p. 261, 1993.

[15] F. Bronold, K. Matyash, D. Tskhakaya, R. Schneider, and H. Fehske, „Radio-frequency discharges in oxygen: I. particle-based modelling“, *Journal of Physics D: Applied Physics*, vol. 40, no. 21, p. 6583, 2007.

[16] H. Summers, „Atomic data and analysis structure“, *JET Report*, 1994.

[17] E. Resler and W. Sears, „The prospects for magneto-aerodynamics“, *Journal of the Aeronautical Sciences*, vol. 25, no. 4, pp. 235–245, 1958.

[18] Kranc, Cambel, and Yuen, *Experimental investigation of magnetoaerodynamic flow around blunt bodies.* National Aeronautics and Space Administration, 1969.

[19] D. Meeker, „Finite element method magnetics“, *FEMM*, vol. 4, p. 32, 2010.

[20] J. M. Park, K. S. Kim, T. H. Hwang, and S. H. Hong, „Three-dimensional modeling of arc root rotation by external magnetic field in nontransferred thermal plasma torches“, *IEEE transactions on plasma science*, vol. 32, no. 2, pp. 479–487, 2004.

[21] K.-H. Kim, „Numerical investigation of plasma flows inside segmented constrictor type arc-heater“, in *Aeronautics and Astronautics*, InTech, 2011.

[22] Bohm, Burhop, Massey, and Williams, *The characteristics of electrical discharges in magnetic fields*, ser. National nuclear energy series: Electromagnetic Separation Project 6. New York: McGraw-Hill, 1949.

[23] I. Langmuir, „Scattering of electrons in ionized gases“, *Physical Review*, vol. 26, no. 5, p. 585, 1925.

[24] D. Bohm and E. P. Gross, „Theory of plasma oscillations. a. origin of medium-like behavior“, *Physical Review*, vol. 75, no. 12, p. 1851, 1949.

7 Cumulative thesis articles

Author Contributions

Article [P1]: "Electrostatic particle-in-cell simulation of heat flux mitigation using magnetic fields", K.F. Lüskow, S. Kemnitz, G. Bandelow, J. Duras, D. Kahnfeld, R. Schneider and D. Konigorski, *Journal of Plasma Physics* 82(5) (2016).
All authors carved out the problem, outlined the calculation, and determined the scope of the article. K.F. Lüskow and R. Schneider performed the analytic calculation. K.F. Lüskow performed the numerical calculation, based on numerical developments by S. Kemnitz, G. Bandelow, J. Duras, D. Kahnfeld and P. Matthias. The manuscript was written by K.F. Lüskow, R. Schneider and D. Konigorski and was edited by all authors.

Article [P2]: "Simulation of heat-flux mitigation using electromagnetic fields",
K.F. Lüskow, S. Kemnitz, G. Bandelow, J. Duras, D. Kahnfeld, R. Schneider and D. Konigorski, *Plasma Physics and Technology Journal* 3(3): 110–115 (2016).
All authors carved out the problem, outlined the calculation, and determined the scope of the article. K.F. Lüskow and R. Schneider performed the analytic calculation. K.F. Lüskow performed the numerical calculation, based on numerical developments by S. Kemnitz, G. Bandelow, J. Duras and D. Kahnfeld. The manuscript was written by K.F. Lüskow, R. Schneider and D. Konigorski and was edited by all authors.

Article [P3]: "Particle-in-cell simulation of the cathodic arc thruster", K.F. Lüskow, P.R.C. Neumann, G. Bandelow, J. Duras, D. Kahnfeld, S. Kemnitz, P. Matthias, K. Matyash and R. Schneider, *Physics of Plasmas* 25(1):013508 (2018).
All authors carved out the problem, outlined the calculation, and determined the scope of the article. K.F. Lüskow and R. Schneider performed the analytic calculation. K.F. Lüskow performed the numerical calculation, based on numerical developments by S. Kemnitz, G.

Bandelow, J. Duras, D. Kahnfeld, K. Matyash and P. Matthias. The manuscript was written by K.F. Lüskow, R. Schneider and P.R.C. Neumann and was edited by all authors.

Article [P4]: "Solution of Poisson's Equation in Electrostatic Particle-in-Cell Simulations", D.Kahnfeld, R. Schneider, K. Matyash, O. Kalentev, S. Kemnitz, J. Duras, K.F. Lüskow, G. Bandelow, *Plasma Physics and Technology Journal* 3(3): 110–115 (2016).
All authors carved out the problem, outlined the calculation, and determined the scope of the article. D. Kahnfeld performed the analytic calculation and the numerical calculation, based on numerical developments by S. Kemnitz, G. Bandelow, J. Duras, O. Kalentev, K. Matyash and K.F. Lüskow. The manuscript was written by D. Kahnfeld and R. Schneider and was edited by all authors.

Article [P5]: "Ion angular distribution simulation of the Highly Efficient Multistage Plasma Thruster", J. Duras, D. Kahnfeld, G. Bandelow, S. Kemnitz, K.F. Lüskow, P. Matthias, N. Koch and R. Schneider, *Journal of Plasma Physics* 83 (2017).
All authors carved out the problem, outlined the calculation, and determined the scope of the article. D. Kahnfeld performed the analytic calculation. J. Duras performed the numerical calculation, based on numerical developments by D. Kahnfeld, G. Bandelow, S. Kemnitz, K.F. Lüskow and P. Matthias. The manuscript was written by J. Duras, D. Kahnfeld, N. Koch and R. Schneider and was edited by all authors.

Article [P6]: "Influence of electron source on the near field plume in a multistage plasma thruster", J. Duras, R. Schneider, O. Kalentev, S. Kemnitz, K. Matyash, N. Koch, K.F. Lüskow, D. Kahnfeld and G. Bandelow, *Plasma Physics and Technology* 3(3): 126–130 (2016).
All authors carved out the problem, outlined the calculation, and determined the scope of the article. J. Duras performed the numerical calculation, based on numerical developments by O. Kalentev, S. Kemnitz, K. Matyash, K.F. Lüskow, D. Kahnfeld and G. Bandelow. The manuscript was written by J. Duras, R. Schneider and N. Koch and was edited by all authors.

Article [P7]: "Electrostatic Ion Thrusters - Towards Predictive Modelling", O. Kalentev, K. Matyash, J. Duras, K.F. Lüskow, R. Schneider, N. Koch and M. Schirra, *Contributions to Plasma Physics* 54(2): 235–248 (2014).

All authors carved out the problem, outlined the calculation, and determined the scope of the article. O. Kalentev, K. Matyash, J. Duras and K Lüskow performed the numerical calculation. The manuscript was written by O. Kalentev, K. Matyash, J. Duras and R. Schneider and was edited by all authors.

Article [P8]: ”Monte-Carlo re-deposition model during terrestrial measurements of ion thrusters”, J. Duras, O. Kalentev, R. Schneider, K. Matyash, K.F. Lüskow and J. Geiser, *Acta Polytechnica* 55(1): 7–13 (2015).
All authors carved out the problem, outlined the calculation, and determined the scope of the article. J. Duras performed the analytic and numerical calculations, based on the numerical development by O. Kalentev, K. Matyash, K.F. Lüskow and J. Geiser. The manuscript was written by J. Duras and R. Schneider and was edited by all authors.

J. Plasma Phys. (2016), vol. 82, 595820502 © Cambridge University Press 2016 1
doi:10.1017/S0022377816000829

Electrostatic particle-in-cell simulation of heat flux mitigation using magnetic fields

Karl Felix Lüskow[1,†], **S. Kemnitz**[1,2], **G. Bandelow**[1], **J. Duras**[1,3], **D. Kahnfeld**[1], **P. Matthias**[1], **R. Schneider**[1] and **D. Konigorski**[4]

[1]Institute for Physics, Ernst-Moritz-Arndt University of Greifswald, Felix-Hausdorff-Str. 6,
D-17489 Greifswald, Germany

[2]Institute of Computer Science, University of Rostock, Albert-Einstein-Str. 22,
D-18059 Rostock, Germany

[3]Department of Applied Mathematics, Physics and Humanities, Nürnberger Institute of Technology,
Keßlerplatz 12, D-90489 Nürnberg, Germany

[4]Airbus Operations GmbH, Emerging Technologies and Concepts, Kreetslag 10,
D-21129 Hamburg, Germany

(Received 13 June 2016; revised 1 September 2016; accepted 2 September 2016)

The particle-in-cell (PIC) method was used to simulate heat flux mitigation experiments with partially ionised argon. The experiments demonstrate the possibility of reducing heat flux towards a target using magnetic fields. Modelling using the PIC method is able to reproduce the heat flux mitigation qualitatively. This is driven by modified electron transport. Electrons are magnetised and react directly to the external magnetic field. In addition, an increase of radial turbulent transport is also needed to explain the experimental observations in the model. Close to the target an increase of electron density is created. Due to quasi-neutrality, ions follow the electrons. Charge exchange collisions couple the dynamics of the neutrals to the ions and reduce the flow velocity of neutrals by radial momentum transport and subsequent losses. By this, the dominant heat-transport channel by neutrals gets reduced and a reduction of the heat deposition, similar to the experiment, is observed. Using the simulation a diagnostic module for optical emission is developed and its results are compared with spectroscopic measurements and photos from the experiment. The results of this study are in good agreement with the experiment. Experimental observations such as a shrank bright emission region close to the nozzle exit, an additional emission in front of the target and an overall change in colour to red are reproduced by the simulation.

Key words: magnetized plasmas, plasma dynamics, plasma simulation

1. Introduction and experimental overview

The thermal protection system of spacecrafts is one of the most expensive parts for space missions. Large efforts are undertaken to develop and use special materials for the thermal protection system (Blosser 1996). One idea was to use magnetic fields

---

† Email address for correspondence: lueskow@physik.uni-greifswald.de

for heat flux reduction. If it is possible to reduce the heat flux by externally applied electromagnetic fields, one would be able to use simpler and cheaper materials. In 2002 the European Space Agency (ESA) started an investigation of heat flux mitigation by means of MHD (magnetohydrodynamics) in partially ionised argon (Gülhan *et al.* 2009). Argon was chosen as test gas for this campaign due to its chemical inertness. This simplifies the analysis and makes the inclusion of complicated plasma chemistry unnecessary.

In the experiment an arc jet was used to create a flow field, with a typical Mach number between 5 and 10, which hits a target. The heat flux on the target surface was measured with and without a magnetic field. Applying a dipole-like external magnetic field a strong heat flux mitigation was observed (Gülhan *et al.* 2009). However, even up to now, the experiments could not be reproduced by models based on Navier–Stokes fluid codes for neutrals with fluid models for the plasma components. One was not able to explain the main effects leading to the heat flux reduction.

One major problem for the modelling is the lack of information about the plasma component in the experiment. There exist only average values for density ($n_e \approx 10^{11}\,\text{cm}^{-3}$) and temperature ($T_e \approx 0.7$ eV), whereas the neutral component is well characterised using different diagnostic methods in terms of temperature and velocities, including axial and radial profiles at specific locations. The average neutral density n_n is $\approx 10^{15}\,\text{cm}^{-3}$.

In addition, spectroscopic data and a video from the experiment are available (Detlev Konigorski, personal communications, January 2014). During the experiment a clear change in the emission was visible in photos looking into the vacuum chamber onto the blunt body. The flow illumination changed to a red colour when the magnetic field was applied, confirmed in observations by Kranc, Cambel & Yuen (1969) in a similar experiment. The large bright area between the arc jet exit and the target shrank by activating the magnetic field and a small bright spot directly in front of the centre of the target appeared (see figure 6 of Gülhan *et al.* (2009)).

There are several groups that have tried to reproduce the experiment in simulations. They all applied Navier–Stokes codes or direct simulation Monte Carlo codes for the neutral gas description. In contrast to the complex and rather complete models of neutral transport, only fluid models for the description of the plasma were used, mostly with estimated transport coefficients (Katsurayama *et al.* 2008; Otsu *et al.* 2012).

Using a self-consistent kinetic particle method instead of fluid models a more realistic description of neutral and plasma dynamics and their interaction is possible. Specifically, an existing particle-in-cell (PIC) code with Monte-Carlo collisions (Tskhakaya *et al.* 2007) is used for this study.

Perturbed plasma source distribution functions are typical for plasma sources, e.g. those shown by Godyak & Piejak (1990) for RF (radio frequency) discharges or by Behringer & Fantz (1994) for DC (direct current) discharges. Such non-Maxwellian characteristics of the plasma components are also expected from the arc jet.

2. Simulation method

The well-established PIC method is combined with Monte Carlo collisions (PIC-MCC). In plasma physics, the PIC method is a widely accepted method to obtain a better understanding of the basic physical mechanisms of various systems because the PIC-MCC approach provides full insight into all (microscopic and macroscopic) parameters. A more detailed description of the PIC-MCC method itself can be found in several reviews (Birdsall & Langdon 2004; Tskhakaya *et al.* 2007)

The principle of PIC is to follow so-called super-particles. Each of these represents the same number of physical particles following the same trajectory as single particles due to their identical mass-to-charge ratio, resulting in the same Lorentz force. The electric field for the Lorentz force is calculated self-consistently on a spatially equidistant grid from the Poisson equation. In the electrostatic approximation, magnetic field effects are included in the Lorentz force, but are determined just by their external sources (e.g. magnets). Corrections from plasma currents are neglected. Particles experience collisions according to Monte Carlo collision algorithms. This allows one to implement all relevant collision types. For this work electron–neutral elastic, ionisation, excitation, Coulomb collision, neutral–neutral and charge exchange collisions are implemented. Effective ionisation and radiation energy losses are included in the model. Neutrals are treated as plasma particles with zero charge. Technically, this is identical to a DSMC (direct simulation Monte Carlo) model for the neutrals.

In the experiment, the neutral density is approximately four orders of magnitude larger than the electron density (Gülhan *et al.* 2009). If one uses the same super-particle factor for plasma and for neutrals, one runs into computational memory limits due to the large number of neutral particles.

Due to the relatively low electron energy compared with ionisation energies above 15 eV, there are only a very small number of ionisation collisions. Due to the very low ionisation degree, the neutrals can be assumed to be practically decoupled in density from the plasma component.

Therefore, different weights for neutrals and plasma particles are taken care of by scaling the cross-section of collisions with neutrals linearly. The cross-section for neutral–neutral collisions is increased quadratically by this factor. These scalings are technically equivalent to modifying the super-particle factor for neutrals. This allows one to reduce the number of pseudo-particles for neutrals to a moderate number. In this work a scaling factor of 10^3 is used.

The spatial domain is two-dimensional (axial and radial). Due to collisions three components in velocity space need to be resolved. The domain consists of 400 axial and 140 radial cells. With a cell size of $\Delta r \approx 1.05$ mm this leads to a domain of 42 cm × 14 cm. The cell size and the time step $\Delta t \approx 10^{-12}$ s are chosen in order to resolve the Debye lengths and the electron cyclotron frequency. For this system the cyclotron frequency ($\nu \approx 7 \times 10^{10}$ Hz) in the region with strong magnetic fields is higher than the plasma frequency ($\omega_{p,e} \approx 3 \times 10^{10}$ Hz).

The target is placed directly at the symmetry axis at the right side of the domain. It has a radius of 3.6 cm and its surface is located at 26 cm according to the experimental conditions. The target has a dielectric surface made out of quartz ($\epsilon = 4.27$) and the inner part is metallic. All boundaries except the left one have a fixed potential of zero. The left domain boundary is set to 0.5 V, to represent the exit of the arc jet and ensure that particles move towards the target. At outer domain boundaries all particles are absorbed. Plasma particles that hit the target are also absorbed, only neutrals are reflected at the surface of the target. This represents the inertness against chemical reactions of the noble gas argon.

The size of the domain is scaled down by a factor of 100 to overcome spatial resolution limits. One applies a self-similarity scaling keeping the relevant non-dimensional parameters constant, namely the ratio of system length to gyroradii and to mean free path. The first represents the influence of the magnetisation by the external magnetic field, the second the collisional effects. By increasing all densities and the magnetic field by the same factor, the ratio of system length to gyroradii

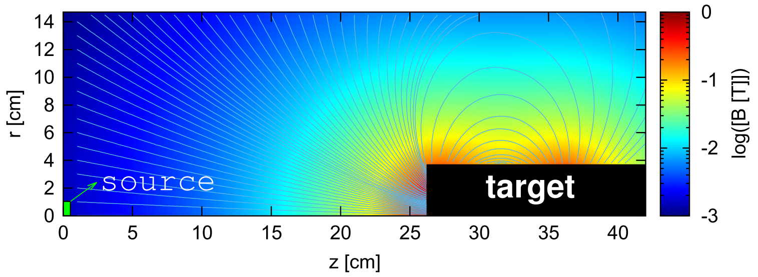

FIGURE 1. Magnetic field in the simulation domain.

and to mean free path is conserved. This ensures the physical correctness of the simulation as proven by Taccogna *et al.* (2005).

The external magnetic field was calculated using the finite-element magnetic method solver (FEMM) (Meeker 2010). The topology of the dipole-like magnetic field is shown in figure 1.

For neutrals a uniform background density (representing background pressure effects) is combined with the main particle source at the left side of the domain near the axis with a radial extension up to 1 cm. The location of the source is shown in green in figure 1. Neutrals are injected with a Maxwellian-distributed velocity with a drift of 2070 m s^{-1} in axial direction according to the mean velocity measured by microwave interferometry. For every sampled velocity it is ensured that particles leave the source with an initial angle smaller than 12° to reproduce the angular distribution of the particle source in the experiment. The characterisation of the plasma species coming from the arc jet is not known experimentally. Therefore, variation of the source parameters was used to represent the experiment as well as possible. Finally, the following plasma source distributions were used. Ions have similar source distributions as the neutrals.

Electrons are injected with a two-Maxwellian distribution. The first one has a shift in energy of approximately 1 eV to represent the measured averaged temperature from experiment and a width of 1 eV. A second Maxwellian with the same shift and variable width and source strength is added. The parameters are fitted to get as close as possible to the experimental results without a magnetic field. The best result are obtained for a source strength of 1/3 of the bulk source and a width of 20 eV. The second contribution is necessary to provide some electrons with higher energies of above 13 eV, otherwise there is no line emission in the visible range as observed in the photos and in the spectroscopic analysis of the experiment. According to Kranc *et al.* (1969) the red emission is due to excitation of metastable argon atoms with energies of approximately 11 eV. The resulting electron energy distribution function is shown in figure 2 for different axial positions.

The number of injected particles is chosen to approximate the average density for electrons ($n_e = n_i \approx 2.8 \times 10^{11}$ cm^{-3}) and for neutrals ($n_n \approx 1.6 \times 10^{15}$ cm^{-3}). For a typical run approximately 4×10^6 super-particles for each plasma species and 6×10^6 super-particles for neutrals are used.

During the experiment strong fluctuations were observed when the magnetic field was applied. To reflect this observation in the model in the case of an applied magnetic field, radial anomalous diffusion is implemented. In addition to the Bohm diffusion (Bohm *et al.* 1949), which scales like

$$D \propto \frac{T}{B}, \tag{2.1}$$

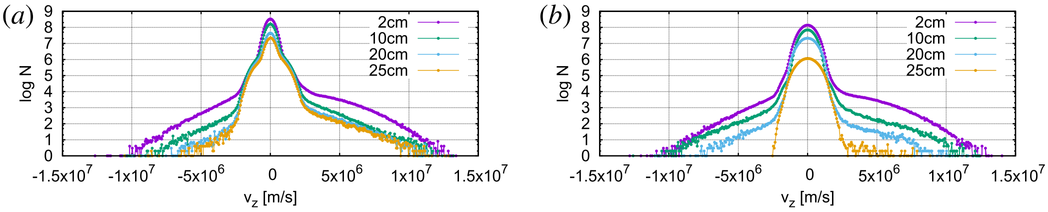

FIGURE 2. Electron axial velocity distribution functions for different axial positions averaged over 10^5 time steps ((*a*): without magnetic field, (*b*) with magnetic field).

with the temperature T and the magnetic field B, a constant transport is taken into account. This contribution is motivated by the fact that the arc jet itself delivers a turbulent flow due to angular gas insertion. Movies of the experiment give the impression that this turbulence is strongly increased within the source by the activation of the magnetic field. For cylindrical geometry the radial diffusion has to be implemented correctly as derived by Bormann, Brosens & De Schutter (2001):

$$p^r_{\pm} = \frac{1}{2}\left(1 \pm \frac{1}{2k}\right), \tag{2.2}$$

with $k = r/\sqrt{2D \times \Delta t}$ for a diffusion coefficient D. The diffusion coefficient is set to 10 $\mathrm{m}^2\ \mathrm{s}^{-1}$ for plasma particles and 1 $\mathrm{m}^2\ \mathrm{s}^{-1}$ for neutrals. The estimation for the coefficients is based on diffusion coefficients from magnetic fusion (Perkins *et al.* 1994). Bohm *et al.* (1949) showed that turbulence in a plasma can be created or at least be enhanced by magnetic fields. The non-local effect is also observed in systems like the cylindrical Hall thruster from PPPL (Princeton Plasma Physics Laboratory) (Ellison, Raitses & Fisch 2012).

3. Discussion

The most important finding from the experiment was a strong heat flux mitigation by activating the magnetic field. According to Gülhan *et al.* (2009) the total heat flux was reduced by 85 %. Due to the large difference between plasma density and neutral density one can expect that most of the heat flux is carried by neutrals. Up to now it has not been understood why their fluxes could be affected so strongly by a magnetic field, because neutrals experience no direct force from the Lorentz force. This is only possible if it is induced by the interaction with the plasma components which react to magnetic fields.

3.1. *Heat flux mitigation*

In the PIC simulation a heat flux mitigation is observed for the case when the magnetic field is applied. This effect is created by a combination of radial turbulent transport and kinetic effects. The first is introduced parametrically the latter is treated self-consistently. The neutral flux is reduced indirectly. Electrons follow the magnetic field lines guiding them towards the target and build up a region of higher density in front of the target. Ions follow due to the constraint of quasi-neutrality. If neutrals arrive in this region their velocity gets reduced by charge exchange collisions with slower ions. The charge exchange collisions act as a parallel momentum sink for the neutrals slowing them down (Lüskow *et al.* 2016). Neutrals lose energy and momentum due to the increased number of collisions with plasma particles and by

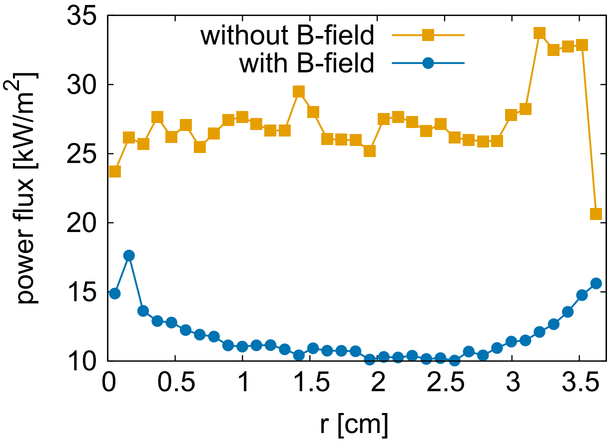

FIGURE 3. Simulated radial profile of the total target heat flux.

this the neutral energy flux to the target is reduced. In charge exchange collisions momentum and energy are transferred from neutrals to ions. Due to strong radial transport most of the ions are guided away from the target in the radial direction and the heat flux of ions is only weakly increased. The reduction of total heat flux is shown in figure 3. The integral total heat flux is reduced by 58% compared to the case without a magnetic field, representing very well the experiment. Details of the model do not yet fit and require further adjustment in terms of source definitions and transport. For example, the strong reduction of the heat flux in the centre is not well represented. Further experimental characterisation of the plasma components and the neutrals in the case with a magnetic field would be very helpful to guide this process.

3.2. *Optical emission spectral analysis*

Experiments used mostly spectroscopy and photos to study the overall behaviour of the system when applying magnetic fields. To verify the simulation against the experiment, diagnostic routines in the PIC-MCC model are developed that provide the emission spectrum for every cell. In the Monte Carlo collision routines, effective energy losses are taken into account. In the open-ADAS library (Summers 1994; Summers & O'Mullaine 2011) one obtains photon emissivity coefficients (PEC) for many transition lines of argon, both ionic and atomic. Details about the calculation of open-ADAS' PECs for argon are given in O'Mullane (2008). The PECs are effective coefficients from a collisional radiative model and are functions of electron energy and density. Due to the kinetic character of PIC, it is possible to calculate the energy distribution function in every cell of the domain. A diagnostics module is added to the code, in which for each wavelength an intensity is calculated integrating the PECs with respective densities and temperatures of electrons over the time-averaged distribution function. By this, for each cell, an emission spectrum can be reconstructed.

For a more detailed comparison with spectroscopic measurements two cells are chosen. The first one is within the shock layer in front of the target ($r = 1\Delta r$, $z = 220\Delta r$), the other one is located in the free stream region ($r = 60\Delta r$, $z = 90\Delta r$). For both regions spectroscopic measurements exist. For all spectra, intensities are scaled to a maximum intensity. This was chosen to represent a typical value for

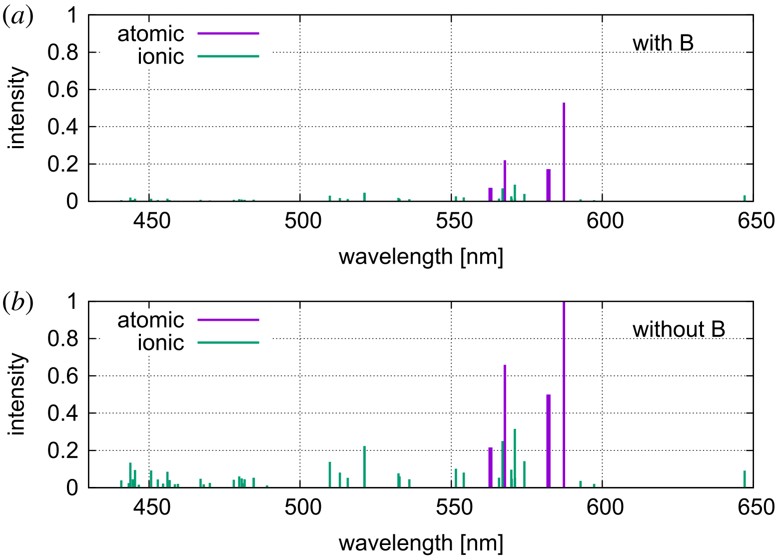

FIGURE 4. Optical emission spectra in the free stream region, (*a*) with magnetic field and (*b*) without magnetic field.

over-saturation of the detector chips in the CCD (charge-coupled device) camera (Janesick 2001). Details will be discussed later. In the free stream, a loss of intensity in several emission lines is visible in figure 4 with the applied magnetic field. This is in good agreement with emission spectroscopy.

Overall, the emission pulls back from the target. This is a consequence of the changes in the electron density distribution. The electrons follow the magnetic field lines and are guided back towards the exit and upwards by the dipole-like field acting similar to a magnetic cusp mirror. Consequently, the electron density is reduced as the magnetic field is applied compared to the non-magnetised case. Therefore, the chance for excitation is also reduced and the overall emission rate is decreased. In the shock the situation is quite different. Experimentally, there is a small bright spot in front of the centre of the target which appears when activating the magnetic field. Here, an increase of intensity of several emission lines is observed (figure 7 of Gülhan *et al.* (2009)). The same tendency appears in our model for this region. Calculated optical emission spectra are shown in figure 5 with and without a magnetic field.

In the experiment the whole photo turns more red by switching on the magnetic field. This is represented in the simulation by larger peaks in the red wavelength region in the cells around the target.

Each wavelength in the optical spectrum has a specific colour. Therefore, it is possible to use the spectrum for every cell in order to calculate a colour, represented by a RGB (red-green-blue)-value. With this, one can try to create a simulated photo that can be compared to the experiment. Details about this procedure will be published elsewhere. CCD cameras have a so-called full-well capacity that describes the maximum number of charges that can be saved in one pixel (Janesick 2001). If this number is reached the CCD sensor for this pixel is saturated and the cell is plotted in white in figure 6, indicating a bright region of emission in the experimental photo. Black regions are cells with no emission.

On the left side the original colour data are plotted. On the right there is a zoom into the shock region in front of the target, shifted in colour space towards green to visualise clearer the effects at the shock.

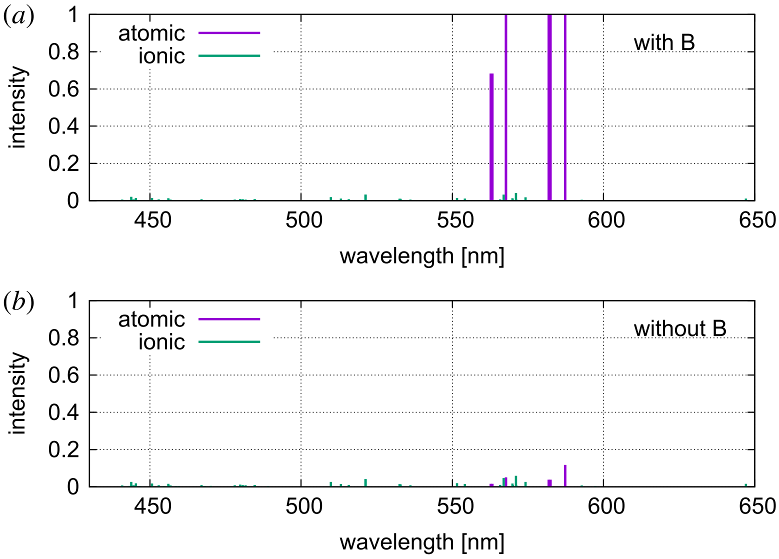

FIGURE 5. Optical emission spectra in the shock front region, (*a*) with magnetic field and (*b*) without magnetic field.

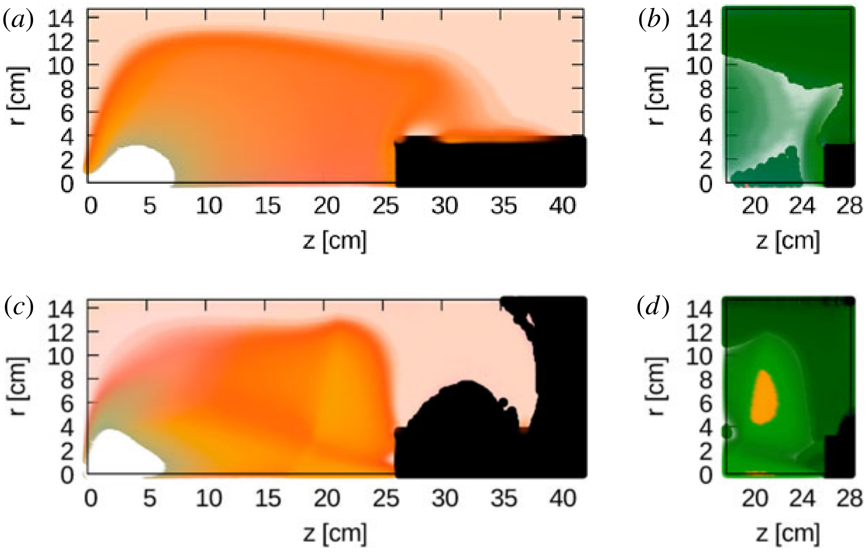

FIGURE 6. (*a*,*c*) colour plot of the optical emission, (*b*,*d*): zoom into the shock region with shifted colours ((*a*,*b*) without magnetic field, (*c*,*d*) with magnetic field).

One can see several features from the experiment which are in good agreement with the simulation. The white area with saturated cells has shrunk towards the arc jet exit when the magnetic field is applied. The shock is smeared out and there are additional emission regions directly in front of the target, one at the centre and one at an outer radial position.

4. Conclusions

A PIC-MCC code was modified and applied to a heat flux mitigation experimental campaign performed by ESA in 2007. During the campaign it was shown that heat flux towards a target can be reduced by a external magnetic field.

The simulation reproduces the heat flux reduction qualitatively. The magnetic field leads to a change in electron and ion density by affecting the trajectories of the charged particles through the Lorentz force. Magnetic field lines in the dipole-like field converge to the centre of the target. As particles are guided into this region a shield of high plasma density builds up in front of the target. Neutral transport is affected by charge exchange collisions with ions acting as a momentum sink for the neutrals and reducing the neutral axial velocity. By this, the resulting total neutral heat flux is reduced. Ion heat flux is increased only weakly, because the radial losses due to the magnetic field and turbulence get stronger.

In addition, the simulation was verified against experimental spectroscopy using optical emission analysis. In the free stream region a loss of intensity for all wavelengths appeared, whereas in front of the target an increase of the intensity is observed. Both effects were in good agreement with the experiment.

A photo was simulated from the calculated optical emission spectrum. The simulation reproduces the observed optical effects when applying the external magnetic field. These effects are an overall red shift, a smaller bright emission region close to the arc jet exit and an emission region in front of the target.

Acknowledgements

This work was supported by the German Space Agency DLR through Project 50RS1508.

REFERENCES

Behringer, K. & Fantz, U. 1994 Spectroscopic diagnostics of glow discharge plasmas with non-maxwellian electron energy distributions. *J. Phys.* D **27** (10), 2128–2135.

Birdsall, C. K. & Langdon, A. B. 2004 *Plasma Physics via Computer Simulation*. CRC Press.

Blosser, M. L. 1996 Advanced metallic thermal protection systems for reusable launch vehicles. NASA Technical Memorandum 110296, October 1996.

Bohm, D., Burhop, E. H. S., Massey, H. S. W. & Williams, R. W. 1949 The characteristics of electrical discharges in magnetic fields. In *National Nuclear Energy Series: Electromagnetic Separation Project 6*, McGraw-Hill.

Bormann, G., Brosens, F. & De Schutter, E. 2001 Modeling molecular diffusion. In *Computational Methods in Molecular and Cellular Biology: from Genotype to Phenotype*, pp. 189–224. MIT Press.

Ellison, C. L., Raitses, Y. & Fisch, N. J. 2012 Cross-field electron transport induced by a rotating spoke in a cylindrical hall thruster. *Phys. Plasmas* **19** (1), 013503.

Godyak, V. A. & Piejak, R. B. 1990 Abnormally low electron energy and heating-mode transition in a low-pressure argon rf discharge at 13.56 mHz. *Phys. Rev. Lett.* **65** (8), 996.

Gülhan, A., Esser, B., Koch, U., Siebe, F., Riehmer, J., Giordano, D. & Konigorski, D. 2009 Experimental verification of heat-flux mitigation by electromagnetic fields in partially-ionized-argon flows. *J. Spacecr. Rockets* **46** (2), 274–283.

Janesick, J. R. 2001 *Scientific Charge-coupled Devices*, vol. 117. SPIE Press.

Katsurayama, H., Kawamura, M., Matsuda, A. & Abe, T. 2008 Kinetic and continuum simulations of electromagnetic control of a simulated reentry flow. *J. Spacecr. Rockets* **45** (2), 248–254.

KRANC, S., CAMBEL, A. B. & YUEN, M. C. 1969 *Experimental Investigation of Magnetoaerodynamic Flow Around Blunt Bodies*, vol. 1393. National Aeronautics and Space Administration.

LÜSKOW, K. F., KEMNITZ, S., BANDELOW, J., DURAS, J., KAHNFELD, D., SCHNEIDER, R. & KONIGORSKI, D. 2016 Particle-in-cell simulation concerning heat-flux mitigation using electromagnetic fields. *Plasma Phys. Technol.* (submitted).

MEEKER, D. 2010 Finite element method magnetics. *FEMM* **4**, 32.

O'MULLANE, M. 2008. Photon emissivities for ArI and ArII. ADAS Communications: ADAS C(08)-01.

OTSU, H., KATSURAYAMA, H., KONIGORSKI, D. & ABE, T. 2012 Effect of the strong magnetic field on the electrodynamic heat shield system for reentry vehicles. *In 43rd AIAA Plasmadynamics and Lasers Conference*. p. 2731. American Institute of Aeronautics and Astronautics.

PERKINS, F., BARABASCHI, P., BOUCHER, D., CORDEY, J. G., COSTLEY, A., DEBOO, J., DIAMOND, P. H., FUJISAWA, N., GREENFIELD, C. M., HOGAN, J. *et al.* 1994 Iter physics basis. In *Plasma Physics and Controlled Nuclear Fusion Research: Proceedings of the International Conference on Plasma Physics and Controlled Nuclear Fusion Research*, vol. 15, p. 477. International Atomic Energy Agency.

SUMMERS, H. P. & O'MULLAINE, M. 2011 Atomic data and modelling for fusion: the adas project. In *7th International Conference on Atomic and Molecular Data and THEIR Aplications-ICAMDATA-2010*, vol. 1344, pp. 179–187. AIP Publishing.

SUMMERS, H. P. 1994 Atomic data and analysis structure. *JET Rep.*

TACCOGNA, F., LONGO, S., CAPITELLI, M. & SCHNEIDER, R. 2005 Self-similarity in hall plasma discharges: applications to particle models. *Phys. Plasmas* **12** (5), 053502.

TSKHAKAYA, D., MATYASH, K., SCHNEIDER, R. & TACCOGNA, F. 2007 The particle-in-cell method. *Contrib. Plasma Phys.* **47** (8–9), 563–594.

Plasma Physics and Technology **3**(3):110–115, 2016

PARTICLE-IN-CELL SIMULATION CONCERNING HEAT-FLUX MITIGATION USING ELECTROMAGNETIC FIELDS

Lüskow K. F. [a,*], Kemnitz S.[a,c], Bandelow G.[a], Duras J.[a],
Kahnfeld D.[a], Schneider R.[a], Konigorski D.[b]

[a] *Ernst-Moritz-Arndt University Greifswald, Institute of Physics, Felix-Hausdorff-Str. 6, 17487 Greifswald, Germany*

[b] *Airbus Operations GmbH, Emerging Technologies & Concepts, Kreetslag 10, 21129 Hamburg, Germany*

[c] *University Rostock, Institute of Informatics, Albert-Einstein-Str. 22, 18059 Rostock, Germany*

[*] `lueskow@physik.uni-greifswald.de`

Abstract. The Particle-in-Cell (PIC) method was used to study heat flux mitigation experiments with argon. In the experiment it was shown that a magnetic field allows to reduce the heat flux towards a target. PIC is well-suited for plasma simulation, giving the chance to get a better basic understanding of the underlying physics. The simulation demonstrates the importance of a self-consistent neutral-plasma description to understand the effect of heat flux reduction.

Keywords: Particle-in-Cell, argon, heat-flux mitigation, electromagnetic fields.

1. Motivation

In space missions an enormous amount of money is spent for the thermal protection systems for re-entry. To minimize these costs one is interested in finding new ways of reducing the heat flux. The idea is to use magnetic fields to guide the flux away from the re-entry vehicle. In 2002 the European Space Agency (ESA) started an investigation on heat flux mitigation by means of MHD in partially-ionized argon-flows. Argon was chosen for first-principle tests, because it is a noble gas and inert. Therefore, additional complications from complex chemistry — like in air — do not appear, simplifying the analysis of such tests. A strong heat flux reduction was measured, created by an externally applied magnetic field [1]. In the past Navier-Stokes fluid codes for the neutrals were applied combined with rather crude models for the plasma components. Such models were not able to reproduce the experimental observations. With the help of a kinetic particle method one expects to get a more realistic description of the system, including neutrals and plasma. Therefore, a Particle-in-Cell code with Monte-Carlo Collisions (PIC-MCC) was developed.

2. Code description and simulation set-up

The code uses the well-established Particle-in-Cell method combined with Monte-Carlo collisions (PIC-MCC). PIC was successfully applied in various fields of plasma physics to obtain a better physical understanding. PIC-MCC simulation delivers a fully self-consistent microscopic description of a plasma. Therefore, all plasma-parameters (macroscopic and microscopic) can be diagnosed. In particular, entities like potential, densities, temperatures, velocity distribution functions and power fluxes can be calculated. A more detailed description of the method itself can be found in different reviews [2, 3].

So-called “super-particles” are used, each of them representing a number of real physical particles. All of them follow the same trajectory due to the fact that they have the same mass-to-charge ratio and therefore the same acceleration by the Lorentz force. The particles move in the self-consistent electric field which is calculated on a spatially equidistant grid from the Poisson equation, which itself is determined by the space charge deposited by the pseudo-particles and the applied boundary conditions. The real mass ratio between electrons and ions is used. Particle collisions are handled by Monte-Carlo collisions (MCC) routines, that change particle-velocities according to the underlying collision dynamics. All relevant collision types are implemented in the code: electron-neutral elastic, ionization, excitation, coulomb collisions, ion-neutral momentum transfer and charge exchange. Neutrals are treated as plasma particles with zero charge. This, in fact, means that the neutral model is a Direct Simulation Monte-Carlo (DSMC) description.

In the model two spatial (axial and radial) and three velocity components (2d3v) are resolved. The computational domain is a region of 42 cm in axial and 14 cm in radial direction. It consists of a particle source on the left boundary and a target on the right, both lying directly at the symmetry axis. All particles crossing the symmetry axis get reflected. The face of the blunt body target is placed at 26 cm, it has a radius of 3.6 cm. The blunt body is implemented as metallic, but is covered by a dielectric surface made of quartz ($\epsilon = 4.27$). The left domain boundary has a fixed potential of 0.5 V to represent the exit of the arc-

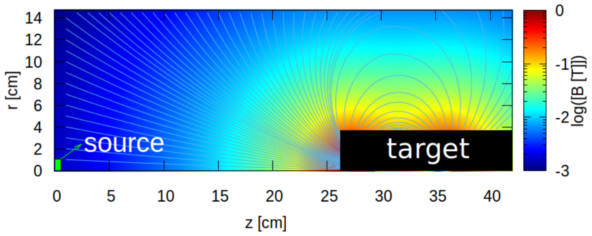

Figure 1. Magnetic field used for the current simulation domain.

jet used for the experiment and ensures that particles injected here move towards the target. The upper and the right domain boundaries are set to zero potential.

The magnetic field was calculated using the Finite-Element Magnetic Method solver (FEMM) [4]. The topology of the dipole-like magnetic field is shown in figure 1.

At outer domain boundaries all particles get absorbed. The same procedure is done for plasma particles at the target. Secondary electron emission can be neglected due to the small emission coefficient of quartz (< 0.5) at low energies [5]. Neutrals are reflected at the target surface, because it is assumed that noble gases are inert to chemical reactions.

A uniform background density is combined with a local particle source at the left side of the domain. The neutral gas density reproduces the background pressure from the experiment that is not created by the source but is an artifact of the non-perfect vacuum creation in the test-chamber.

The number of particles injected in each timestep were adjusted in order to reach the measured density from the experiment ($n_e = n_i \approx 2.8 \cdot 10^{11}\,\mathrm{cm}^{-3}$, $n_n \approx 1.6 \cdot 10^{15}\,\mathrm{cm}^{-3}$). Neutrals are injected with a maxwellian-distributed velocity with a drift of 2070 m/s to represent the free stream velocity measured by microwave interferometry. Ions have similar source velocities as neutrals. Electrons are injected with a two temperature energy distribution. The main peak of the distribution function is at 0.7 V which is the measured averaged electron temperature from experiment. Due to the strong emission of light during experiment one also needs hot tail electrons that are represented in the simulation by a second distribution at higher energies but with lower particles numbers. This is a typical feature of plasma sources, for example in RF plasmas [6]. The high energy tails exist because the mean free path of such electrons are longer than the source dimension and non-Maxwellian distribution functions can sustain. A plot of the energy distribution functions that is injected in the simulation can be seen in figure 2.

To optimize numerical performance the size of the domain is scaled down by a factor of 100 preserving the ratios of system lengths to gyroradii and mean free path. As a consequence of similarity scaling densities and the magnetic field are increased by the same factor. This ensures the correct physical behavior of all particles.

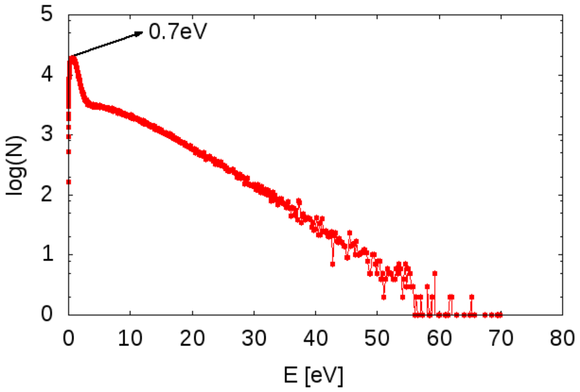

Figure 2. Electron energy distribution injected by the particle source.

The large difference between neutral and plasma density leads to a problem in computational resources due to the large number of neutral particles if the same pseudo-particle factor is applied to neutrals and plasma. Fortunately, the ionization threshold energy is beyond the measured electron temperature, so one can consider the ionization as negligible. Therefore, one is allowed to implement an additional scaling factor for neutral super-particles. For the current simulation an additional weighting factor of 10^3 is applied. The weighting factor linearly increases the cross-section for every collision in which one neutral is involved. The cross section for neutral-neutral collisions is multiplied by the square of the weighting factor.

According to experimental observations there are stronger fluctuations setting in by applying the magnetic field than in the unmagnetized case. To take this into account in the simulation a radial diffusion model was implemented for the magnetized case. A diffusion coefficient of $10\,\mathrm{m}^2\,\mathrm{s}^{-1}$ is used for plasma particles. For neutral particles a coefficient of $0.1\,\mathrm{m}^2\,\mathrm{s}^{-1}$ is set.

This estimate is based on diffusion coefficients from magnetic fusion [7]. It is well-known that turbulence in a plasma can be created or at least can be enhanced by magnetic fields [8]. Without activating the turbulence all particles move towards the center of the target and the flux will be strongly increased in contrast to the experiment.

3. Results

3.1. Comparison of the simulation with experiment

To ensure that the simulation represents the correct physics as observed in the experiment, one has to compare the results from the simulation with the measurements from the experiment. Unfortunately, plasma parameters are not well diagnosed in the experimental campaign. One has only line-averaged values for electron temperature and density. The electron den-

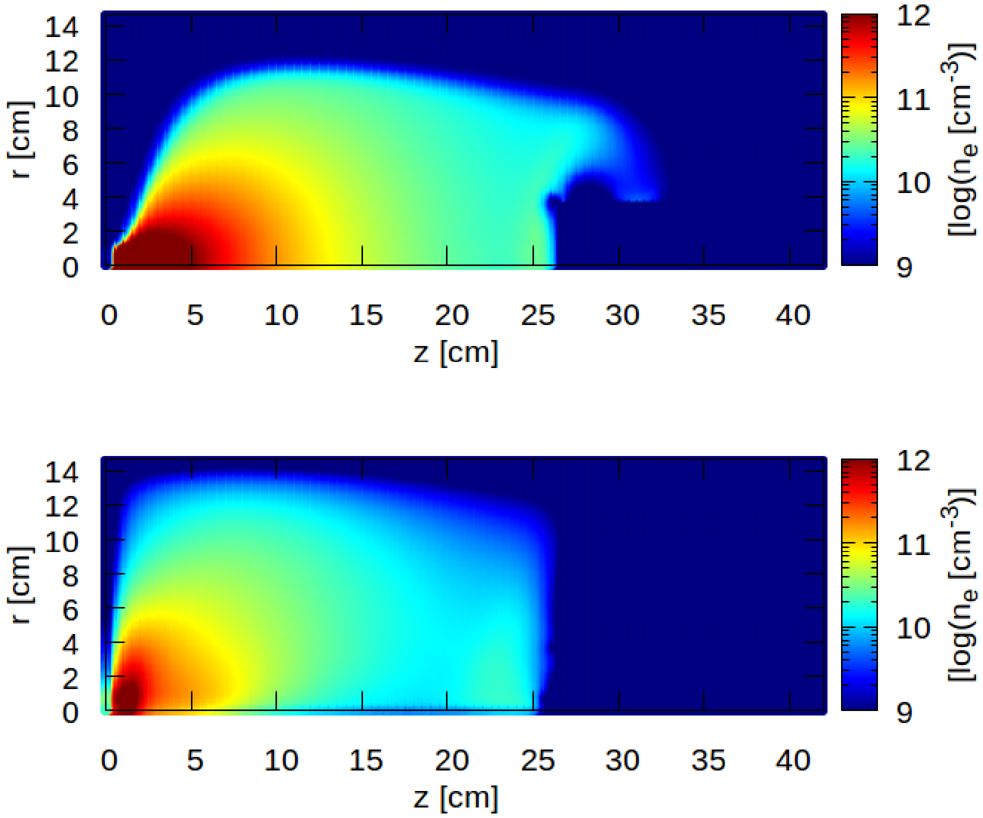

Figure 3. Electron density without (top) and with (bottom) magnetic field.

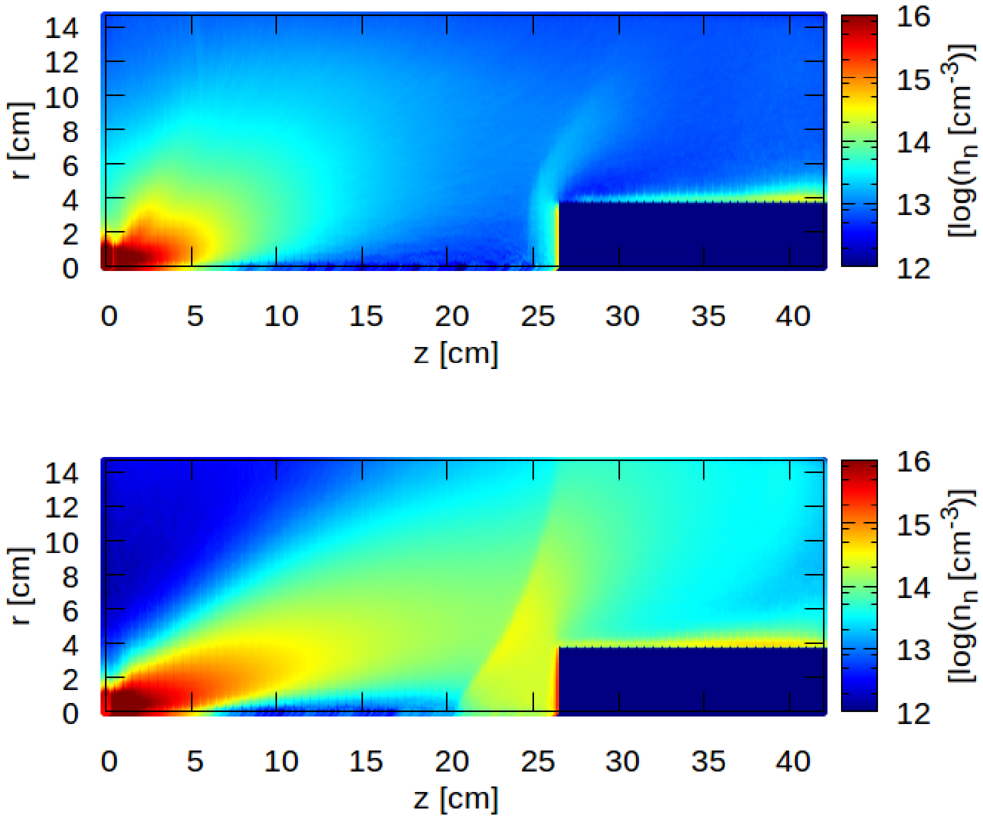

Figure 4. Neutral density without (top) and with (bottom) magnetic field.

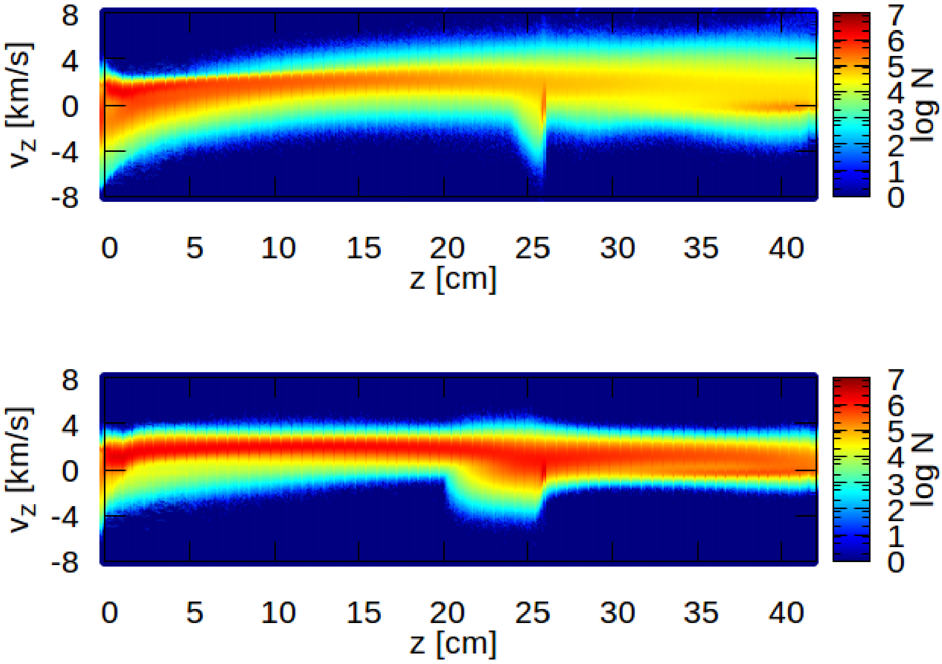

Figure 5. Distribution function of the axial velocity component for neutral particles without (top) and with (bottom) magnetic field.

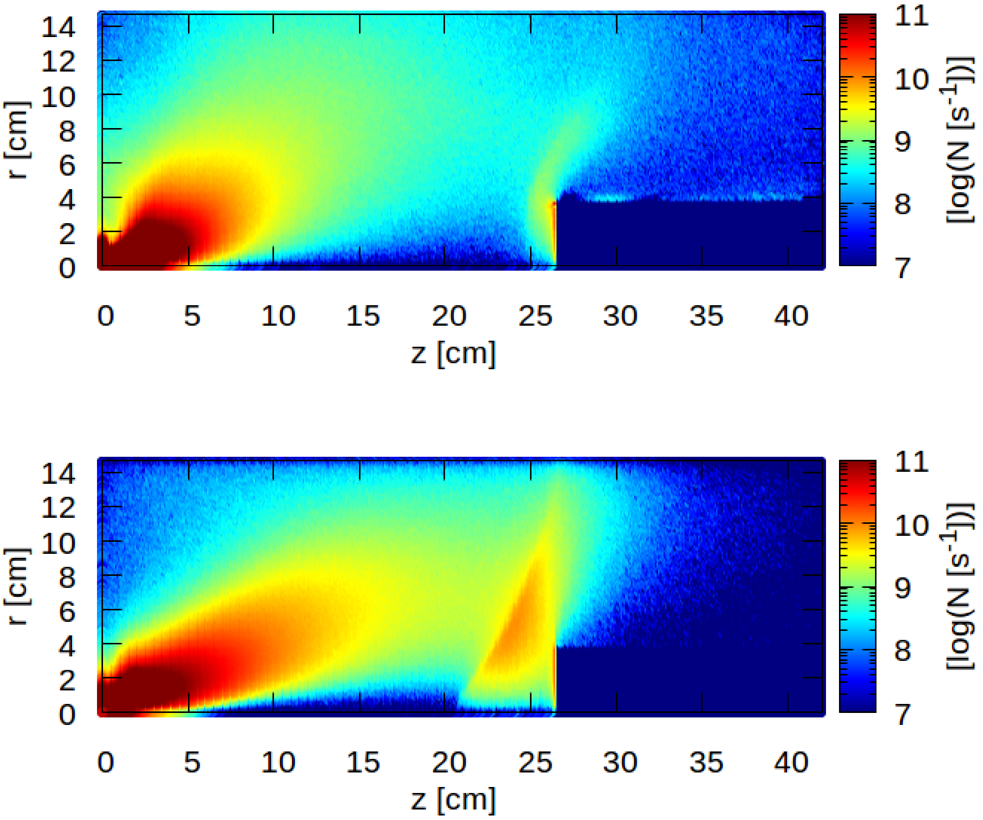

Figure 6. Number of charge exchange collisions per second without (top) and with (bottom) magnetic field.

sity n_e in the experiment was measured by microwave interferometry with the result of $2.8 \cdot 10^{11}\,\mathrm{cm}^{-3}$ [1]. The simulated density averaged over the region where the measurement takes place is $1.8 \cdot 10^{11}\,\mathrm{cm}^{-3}$ for the case without magnetic field. In figure 3 the electron density is shown with and without magnetic field.

In accordance with the experiment one can see a push-back of the region of high electron density from the target. This is in good agreement with the shrinking of the bright emission region from experiment [1]. In addition, the density distribution is changed significantly and in front of the target a region of higher density occurs. Experimentally, an additional bright emission region near the target appears when a magnetic field is applied.

In contrast to plasma parameters the neutral gas dynamics is very well characterized. The averaged neutral density in experiment was $1.6{\cdot}10^{15}\,\mathrm{cm}^{-3}$. So it is about 4 orders of magnitude larger than the electron density. The simulated neutral density distribution can be seen in figure 4. In good agreement with the experiment without magnetic field a clear shock front at the target is obtained. The average velocity of neutrals in this region is decreasing from supersonic (about 2 500 m/s) to less than 1 000 m/s. The original sharp shock front in the case without magnetic field gets broadened in the case with magnetic field. This broadening is a combination of very strong charge exchange collisions and radial anomalous turbulent transport introduced as described before. The triangular shape of the neutral density in the case with magnetic field is a consequence of the plasma species reacting to the magnetic field. Electrons are magnetized and follow the magnetic field. They get pushed towards the front side of the target, where they accumulate. The increased turbulent transport leads to a radial triangular structure of this increased density region reflecting also the structure of the magnetic fieldlines. Ions follow electrons due to quasi-neutrality and pile up there as well. Charge exchange collisions couple this density increase in the plasma species to the neutrals. Therefore, this triangular structure builds up for neutrals as well. It would be interesting to check, whether this triangular shape in density and the broadening of the shock front is also detectable in experiment. Indications are existing in the experiment, because the shock front practically vanished in the case with magnetic field in the photos (see Figure 6 of [1]).

The simulated axial velocity distribution from DSMC is shown in figure 5 summed over all neutrals with the same axial position independent of their radial position. One can see that the main peak is at about $2\,000\,\mathrm{m\,s}^{-1}$ similar to the experimentally observed velocity of $2\,350\,\mathrm{m\,s}^{-1}$. In front of the target there are neutrals with negative axial velocities. These neutrals originate from reflection at the target as determined by collisional effects in the solid (collisional cascades).

The velocity distribution function for ions in Figure 7 looks very similar to the one for neutrals. This resembles the strong coupling by charge exchange collisions.

3.2. Heat Flux Reduction

The most important finding from experiment was the strong heat flux mitigation by activating the magnetic field. Due to the relative small electron and ion densities compared to the neutral density one can estimate that most of the heat flux towards the target is carried by the neutrals. Up to now the reason for the strong heat flux reduction by an magnetic field was not understood, because there exists no obvious direct coupling between B-field and neutral particle dynamics.

In the simulation results a significant change in the neutral velocity distribution function appears when the magnetic field is activated. In front of the target there are more particles with negative axial velocities than in the case without magnetic field. An explanation for this can be found in the coupling to the movement of plasma particles.

Electrons moving towards the target experience magnetic field gradients redirecting them towards the axis. As a consequence a redistribution of electron density with an increased density near the axis even in front of the mach cone is appearing. Due to quasineutrality the ion density needs to be similar to the electron density. Argon has the characteristics of very high charge exchange cross-sections. Therefore, the increased ion density in front of the mach cone leads to more charge-exchange collisions that modify the velocity of the neutrals, see figure 6.

This shows up as an increased region of negative velocities in the axial velocity distributions (see figure 5). As a consequence, the averaged neutral velocity gets reduced compared to the case without magnetic field. The total heat flux profile is summed up over all species contributions (electrons, ions, neutrals). It is dominated in this case by the neutral component. Therefore, less neutral flux reach the target and the total heat flux is reduced, see figure 8. The charge-exchange collisions act as a parallel momentum sink for the neutral flow slowing it down. The integral reduction of the total heat flux can be calculated by integrating the flux over the target in radial direction. The result is a mitigation to 57% of the original heat flux without magnetic field. The measured heat flux reduction was 85% with rather large experimental uncertainties.

4. Conclusions

In the frame of this study a PIC-MCC code was developed to simulate a heat flux mitigation experimental campaign performed by DLR 2007. The main result of the experimental campaign was the demonstration to reduce the total heat flux by externally applied

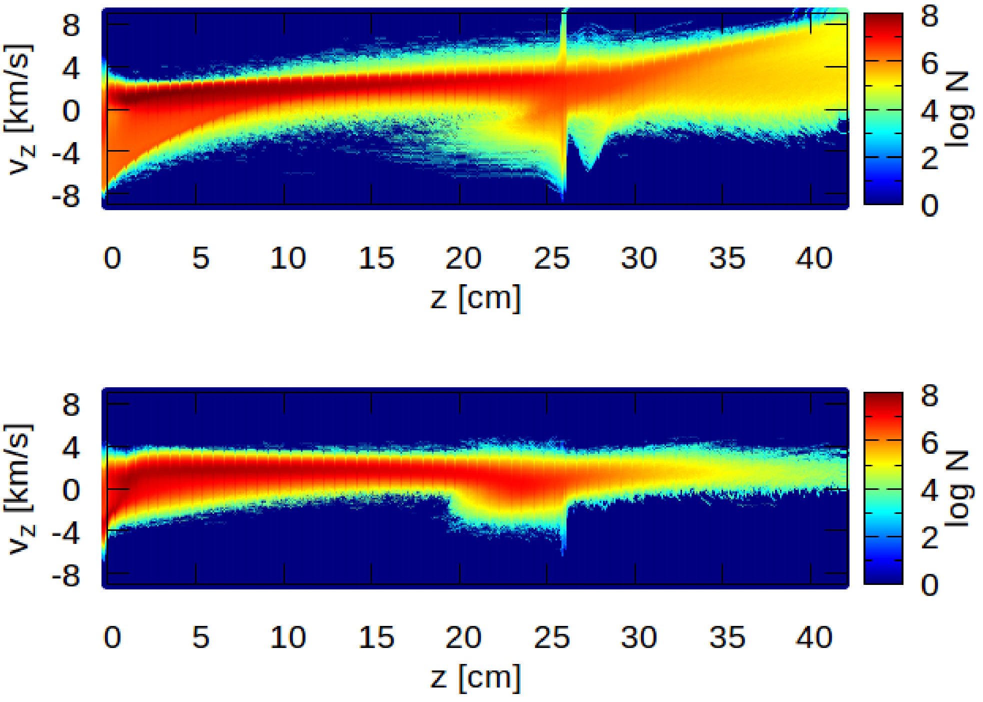

Figure 7. Distribution function of the axial velocity component for ions without (top) and with (bottom) magnetic field.

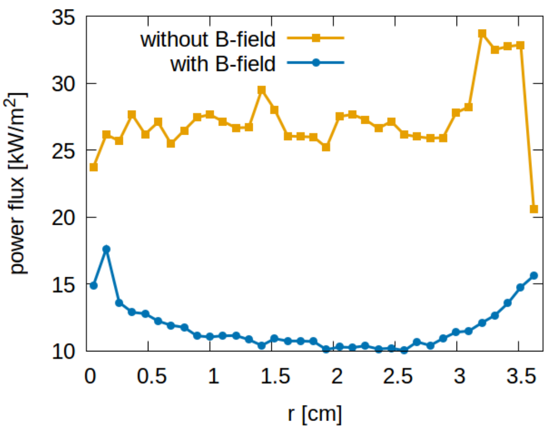

Figure 8. Simulated radial profile of the total heat flux on the target.

magnetic fields. This effect was qualitatively reproduced by PIC-DSMC simulations for the first time. A possible explanation for the effect was found by an increase of charge exchange collisions between plasma ions and neutrals. This shields the target from the impinging neutral particles acting as a momentum sink for the neutral gas flow. The increased ion density driving this effect is also affected by increased radial turbulent transport observed experimentally in the magnetized plasma and taken into account also in the model.

Acknowledgements

This work was supported by the German Space Agency DLR through Project 50RS1508.

References

[1] Ali Gülhan, Burkard Esser, Uwe Koch, Frank Siebe, Johannes Riehmer, Domenico Giordano, and Detlev Konigorski. Experimental verification of heat-flux mitigation by electromagnetic fields in partially-ionized-argon flows. *Journal of Spacecraft and Rockets*, 46(2):274–283, 2009.

[2] Charles K. Birdsall and A. Bruce Langdon. *Plasma physics via computer simulation.* CRC Press, 2004.

[3] D. Tskhakaya, K. Matyash, R. Schneider, and F. Taccogna. The particle-in-cell method. *Contributions to Plasma Physics*, 47(8-9):563–594, 2007.

[4] David Meeker. Finite element method magnetics. *FEMM*, 4:32, 2010.

[5] A Dunaevsky, Y Raitses, and NJ Fisch. Secondary electron emission from dielectric materials of a hall thruster with segmented electrodes. *Physics of Plasmas (1994-present)*, 10(6):2574–2577, 2003.

[6] VA Godyak and RB Piejak. Abnormally low electron energy and heating-mode transition in a low-pressure argon rf discharge at 13.56 mhz. *Physical review letters*, 65(8):996, 1990.

[7] F Perkins, P Barabaschi, D Boucher, JG Cordey, A Costley, J Deboo, PH Diamond, N Fujisawa, CM Greenfield, J Hogan, et al. Iter physics basis. In *Plasma Physics and Controlled Nuclear Fusion Research: Proceedings of the... International Conference on Plasma Physics and Controlled Nuclear Fusion Research*, volume 15, page 477. International Atomic Energy Agency, 1994.

[8] D. Bohm, E. Burhop, H. S. W. Massey, and R. Williams. *The characteristics of electrical discharges in magnetic fields.* National nuclear energy series: Electromagnetic Separation Project. McGraw-Hill, 1949.

PHYSICS OF PLASMAS **25**, 013508 (2018)

Particle-in-cell simulation of the cathodic arc thruster

Karl Felix Lüskow,[1,a)] Patrick R. C. Neumann,[2,b)] Gunnar Bandelow,[1] Julia Duras,[3]
Daniel Kahnfeld,[1] Stefan Kemnitz,[4] Paul Matthias,[1] Konstantin Matyash,[1]
and Ralf Schneider[1]
[1]*Institute of Physics, Ernst-Moritz-Arndt University of Greifswald, 17489 Greifswald, Germany*
[2]*Neumann Space Pty Ltd., 41 Wood Avenue, Brompton 5007, South Australia, Australia*
[3]*Department of Applied Mathematics, Physics and Humanities, Nuremberger Institute of Technology, 90489 Nuremberg, Germany*
[4]*Institute of Computer Science, University of Rostock, 18059 Rostock, Germany*

(Received 7 November 2017; accepted 26 December 2017; published online 12 January 2018)

The cathodic arc thruster is a newly developed electric propulsion system. It provides a stream of ions with very high velocities from a solid conducting cathode. This high ion velocity in combination with a high ionization fraction makes the cathodic arc thruster attractive for spacecraft propulsion. In the past, a record-high specific impulse was measured for such thrusters. The thruster uses a voltage of $-220\,\mathrm{V}$ at the cathode for several microseconds, producing plasma from the cathode material which then streams out of the thruster producing thrust. In this work, a two-dimensional axial-symmetric particle-in-cell code with Monte-Carlo collisions is used to simulate the plasma of a cathodic arc thruster with a simplified wall model for the initial triggering of the arc. The work concentrates on the plasma transport and aims not at a self-consistent description of the arc, including plasma-wall interaction, e.g., description of the erosion and surface heating. The interaction of the arc beam with the background plasma results in a plasma-beam instability. Due to this instability charge separation can be detected that leads to large electric fields. By this electric field, plasma particles are accelerated and contribute to the thrust. *Published by AIP Publishing.*
https://doi.org/10.1063/1.5012584

I. INTRODUCTION

Cathodic arc thrusters are a new development that could permit the delivery of far higher mass fractions to destination orbits due to their high specific impulse.[1] The eroded material from a conducting cathode is ejected by a striking electrical arc between the anode and cathode.[2] Due to its high current discharge, this material is ionized and plasma is accelerated away from the cathode surface.[3] Previous studies measured extremely high ion velocities for such pulsed cathodic arc thrusters. Measurements of erosion rates have confirmed that these thrusters can operate highly efficient.[1,2,4,5]

In order to get deeper insight into the underlying physics, simulations are perfectly suited.[6] Results of simulations can support the experimental development by providing a basic understanding of the system. Due to the non-Maxwellian character of cathodic arc thrusters, a fully kinetic plasma description is needed. Plasma particles have no chance to maxwellize, due to strong magnetic fields, very fast electrons from the initial arc and, in consequence, mean free paths longer than the device dimension. Particle-In-Cell with Monte-Carlo collisions (PIC-MCC) is a widely used kinetic method to simulate a plasma and is used in this work to study the time-dependent behavior of a cathodic arc thruster.

II. BASICS

Pulsed cathodic arcs are high current, low voltage discharges at low pressure that ablate and ionize the cathode material and then accelerate that material away from the cathode surface in small regions known as cathode spots.[7] This results in a highly ionized quasi-neutral plasma being ejected from the cathode and directed downstream at high velocity.[4] Devices of this type are used for ion implantation and surface modification in industry, in applications ranging from the creation of hard films on the surface of tools to altering the bioactivity of polymer surfaces.[5,8] An application which has been of interest in recent years is that of spacecraft propulsion, where the high ion velocity implies that a flight-rated pulsed arc thruster could operate at specific impulses far greater than current technologies.[1,9,10] The design of experimental systems should be informed by high fidelity simulations that run at conditions experienced in laboratory experiments, so that simulation results can be verified using experimental results.[6] This work presents simulations of the cathodic arc plasma undertaken using PIC-MCC to guide the development of a pulsed arc thruster system.

III. SIMULATION METHOD

The well-established electrostatic Particle-In-Cell method is combined with Monte Carlo collisions (PIC-MCC). PIC-MCC provides time-dependent information about all microscopic and macroscopic parameters of a plasma. In particular, physical entities like potential, densities of all species, temperatures, and velocity distribution functions can be calculated. For further information about the PIC-MCC method itself, several reviews can be found.[11,12]

The idea behind PIC is to follow the so-called super-particles where one super-particle represents a certain

---

[a)] lueskow@physik.uni-greifswald.de
[b)] patrick@neumannspace.com

number of physical particles. Due to the same mass-to-charge ratio as a single particle, the super-particle follows the same trajectory as the single particle. The electrostatic electric field is calculated self-consistently by using a Poisson solver on an equidistant rectangular grid. The electrostatic approximation can be used here, because the magnetic fields generated from the electric plasma currents can be neglected compared with the self-consistent electric fields or background magnetic fields (e.g., from coils) acting in the Lorentz force. Collisions between particles are simulated using Monte Carlo collision algorithms. This is valid as long as the collision term in the kinetic equation can be linearized in time, which is valid for the small time steps used in PIC. This allows implementing all relevant types of collisions like electron-neutral elastic, ionization, excitation, Coulomb collisions, neutral-neutral, and charge exchange collisions. Neutrals are treated the same way as plasma particles, but due to their zero charge they experience no electric forces. This is equivalent for the neutral transport to a DSMC (Direct Simulation Monte Carlo) description.

The two-dimensional cylinder symmetric domain used in this study consists of 150 cells in radial and 400 cells in axial direction. To resolve the collision dynamics correctly, all three dimensions in velocity space are resolved. Using a cell size of $dr = 1\,\mathrm{mm}$ leads to a domain size of $15\,\mathrm{cm} \times 40\,\mathrm{cm}$. This guarantees to resolve the shortest length-scale of the system, namely, the Debye scale. A time step of $dt = 10^{-12}\,\mathrm{s}$ is chosen in order to resolve the fastest time-scale of the system, namely the plasma frequency. Due to slower velocities of ions and neutrals compared to electrons, a sub-cycling can be used for both species. This means that neutrals and ions are pushed only every two hundredth time step. A similar ansatz can be followed for collisions. According to the collision, frequency collisions are performed only every tenth time step.

The magnetic field created by the magnetic coils is calculated using the finite element solver FEMM.[13] A plot of the magnetic field lines including the position of magnetic coils, anode, cathode, cathodic mount, and a trigger pin is shown in Fig. 1. To improve the numerical performance, the size of the system is scaled down by a self-similarity factor of 100 applying a scaling which preserves the ratios of length to gyroradii and mean free path. Consequently, all densities and the magnetic field are multiplied by this factor. By using this scaling, one ensures the correct physical behaviour of the scaled system compared to the real one.[14] The similarity scaling is motivated by the one of Taccogna *et al.*[15]

The potential at all outer boundaries of the domain is set to zero voltage and all particles get absorbed. Also, the anode is grounded, whereas at the cathode a pulsed potential boundary condition is applied. For the pulse lengths of $1.7\,\mu\mathrm{s}$ $-220\,\mathrm{V}$ is set at the cathode and electrons are injected into the system at the trigger pin. The voltage of $-220\,\mathrm{V}$ is chosen according to the experiment of Neumann Space, but the simulation allows every other voltage as a boundary condition. When the pulse has ended there is a cool-down phase of $0.5\,\mu\mathrm{s}$. During this phase, the cathode is at ground potential and the electron injection is turned off. Afterwards, $-220\,\mathrm{V}$ is applied again and the injection source is turned on again. During the injection phase, fast electrons of about $20\,\mathrm{eV}$ are injected at the pin. This mimics the initial arc phase, which is not included self-consistently in the simulation. Electrons move then towards the cathode. If an electron hits the cathode, there is a probability of 1% to sputter a neutral from the cathodic surface according to the approach of Timko *et al.*[16]

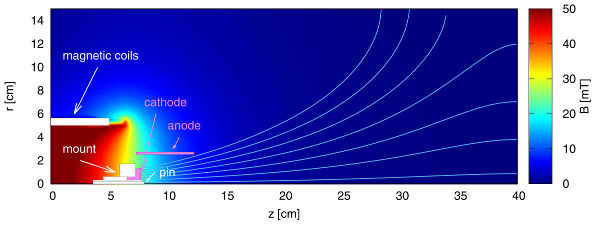

FIG. 1. Magnetic field and simulation domain.

As discussed in experimental reviews about arcs,[17,18] one of the most uncertain physics aspects is the triggering mechanism. Several different mechanisms had been proposed for this like thermionic electron emission, photoinduced ionization, sputtering, evaporation, and oxide removal.[19–22] It is still not clear which processes are active for certain conditions. Therefore, and to hold this part of the simulation as simple as possible, the approach of Timko *et al.* is used as the initial trigger for the simulations of arc discharges[16] in this paper. Timko *et al.*[16] were able to reproduce the observed currents. All plasma transport processes resulting from this initial trigger are simulated self-consistently in the code. Further effects in the cathode spot are neglected, e.g., ion emission.[17] Ion emission would contribute mostly to the surface heating which is not included in the model. Ions emitted from the surface will not contribute to the plasma because they experience the sheath in front of the wall and will be redeposited on the cathode delivering additional cathode heating. This paper describes the dynamics of the plasma in the thruster channel. Therefore, the approach for the physics at the cathode is chosen rather simplistic. If one wants to model the dynamics of the arc itself including effects like dynamical cathode spots, other timescales than here would be of interest and a molecular dynamic description is needed like in Ref. 23. In Ref. 17, the equilibration time for a cathodic arc is given as typically larger than $1\,\mu\mathrm{s}$. In the system analyzed here, the typical pulse length is a few milliseconds and the arc is not fully developed in terms of densities and currents. This dynamic behavior requires a kinetic description of the system, because equilibration is not reached. The electron density stays below $10^{12}\,\mathrm{cm}^{-3}$. Therefore, electrostatic Particle-in-Cell calculations are appropriate and possible for this system.

These neutrals can be ionized by other fast electrons and ions are created. Every impinging ion that reach the cathode can emit a new neutral. Neutrals that are sputtered from the surface are injected into the system with Maxwell distributed velocities, assuming room temperature.

Electrons are magnetized and stream along the magnetic field lines towards the exit of the thruster. Ions follow electrons due to quasi-neutrality in the plasma and contribute to the thrust. At the end of the pulse after $1.7\,\mu\mathrm{s}$, all plasma particles left the thruster producing maximum thrust. Only neutrals remain in the thruster as an inventory for higher ionization during the next pulse. After about 4–5 pulses, a quasi-steady state is reached, because the dynamic relaxation process of the neutrals has saturated and the whole thruster is filled up with neutrals.

IV. RESULTS

The large benefit of a PIC simulation is that it allows diagnosing all macroscopic and microscopic quantities time-dependently. Figure 2 shows the behavior of electron and ion densities. The number of super-particles in the system is shown at the top of this figure, left side for electrons and right side for ions. One can see that the number of electrons fluctuates strongly after a short ramp-up phase, whereas the ion number increases continuously and remains afterwards relatively constant until the end of the pulse. Electrons have a very small mass compared to ions; therefore, their dynamic response to changes is much faster. Heavy ions are slow and experience only the time-averaged electric field, like already discussed in detail for radio-frequency plasmas.[24]

The strong fluctuations in the number of electrons are also visible in the different snapshots of the electron density during a pulse, which are shown on the left side of Fig. 2. First, electrons starting from the pin fill up the thruster and by following the magnetic field lines they form a small plume after the exit of the thruster. Ions are created near the cathode and a small plasma builds up (a) during the first 0.3 μs. Therefore, the number of electrons and ions increases monotonically. The plasma density inside the thruster increases especially near the cathode where ions are injected. At time (b), which is after 0.3 μs first fluctuations in the electron density show up and a blob of electrons is separated from the bulk plasma at the thruster exit around $z = 15$ cm. Afterwards, fluctuations in the electron density begin to increase. Similar to a plasma gun, regions with higher electron density form, separate and are sent out of the thruster (c). After each release of electrons, the plasma reaches a minimum in electron density, whereas the ion density increases further (d). Ions are slower and do not react as fast as electrons. Therefore, electrons are stronger influenced by fluctuations. Electron density builds up again until a critical density is reached. When this limit is reached, new blobs of electrons form and leave the thruster. The electron blobs now get so large that even ions are carried with them due to quasi-neutrality and one can detect small ion blobs (e), too. At this point, the fluctuations have grown so strong that several blobs leave close to the axis with a high frequency, visible at axial positions 20 and 28 cm. After 1.7 μs, the end of the pulse is reached and the anode potential is set to zero Volts. In the plots of super-particle numbers at the top of Fig. 2, this is visible in a strong decrease of the particle numbers of both plasma species. The plasma collapses and only neutrals remain in the thruster channel. For the start of the next pulse, the remaining neutrals act as an inventory for ionization. Therefore, the plasma builds up faster, fluctuations are getting even stronger and the thrust is higher than in the first pulse. After about 4–5 pulses, one reaches a quasi-steady state, because the whole thruster is pre-filled with neutrals.

The fluctuations increase in size and frequency, characteristic of a plasma instability. This instability is responsible for the dynamics of the thruster described before. To identify the underlying effect responsible for these fluctuations, a phase space analysis for electrons is shown in Fig. 3. The plots show the phase space of velocity in axial direction v_z as a function of axial position z.

The six plots are snapshots of the phase space taken at the same time as the density snapshots discussed before. In the first plot (a), the thruster fills up with electrons. Beyond the exit of the thruster, which is located at $z = 15$ cm, fast electrons leave the thruster with velocities larger than 10^7 m/s. At time step (b), first fluctuations occur in the density. In the phase space plot first eddies appear, characteristic of a plasma-beam instability. There are fast beam electrons with about 1.4×10^7 m/s and background electrons from the plasma in the thruster channel. Considering the densities of beam and plasma electrons, following Birdsall[11] one can estimate the ratio $R = n_b/n_p \propto \omega_{pb}/\omega_{pp} \approx 0.01$. This is typical of a plasma-beam instability with a weak beam and a cold plasma.[11,25,26] Taking into account $R = 0.01$ and following the calculations of Birdsall,[11] the instability frequency can be estimated as $\omega = 0.93\omega_p = 0.93\sqrt{\frac{n_e e^2}{\epsilon_0 m_e}}$. Using an average electron density near the cathode of $n_e \approx 10^{15}\,\mathrm{m}^{-3}$, an instability frequency of $1.8 \times 10^9\,\mathrm{s}^{-1}$ is obtained. This analytical result is similar to the frequency of the emitted electron blobs that one can see at time step (c), namely $10^9\,\mathrm{s}^{-1}$. Three regions of trapped electrons with low energies are visible. Also, three blobs of very fast electrons appear that will leave the thruster during the next time steps. In the fourth plot (d), the instability has reached its maximum, producing also a maximum in the velocity of electrons leaving the thruster. The inventory of electrons in the thruster has to build up again, which is reached in the next time step (e). The phase space plot shows slow trapped electrons in the thruster and also some very fast blobs of electrons that leave the thruster. At timestep (f), the potential is shut down and the bulk plasma leaves the thruster, too.

After identifying the beam-plasma instability, one can explain now the electron blobs dynamics that contribute to the thrust. It is well known that the plasma-beam instability is linked with a time-varying potential, which is shown in Fig. 4. The time steps for the potential plots are the same as for density and phase space.

In the first plot (a), the potential builds up, in plot (b) first potential gradients establish beyond the exit of the thruster, which creates electric fields in the plume. These potential gradients get larger in (c), where for the first time positive potential values are detected. The steep potential gradients that are built up now enlarge the electric fields up to about 10 kV/m. Following the simple model of Birdsall,[11] the electric field E is calculated as

$$\frac{1}{4}\epsilon_0 E^2 = 4 m_b n_b v_0 \Delta v \;\Rightarrow\; E \approx 4 \times 10^4\,\mathrm{kV/m}. \qquad (1)$$

This calculated electric field has the same order of magnitude as the electric field obtained in the simulation. In (d),

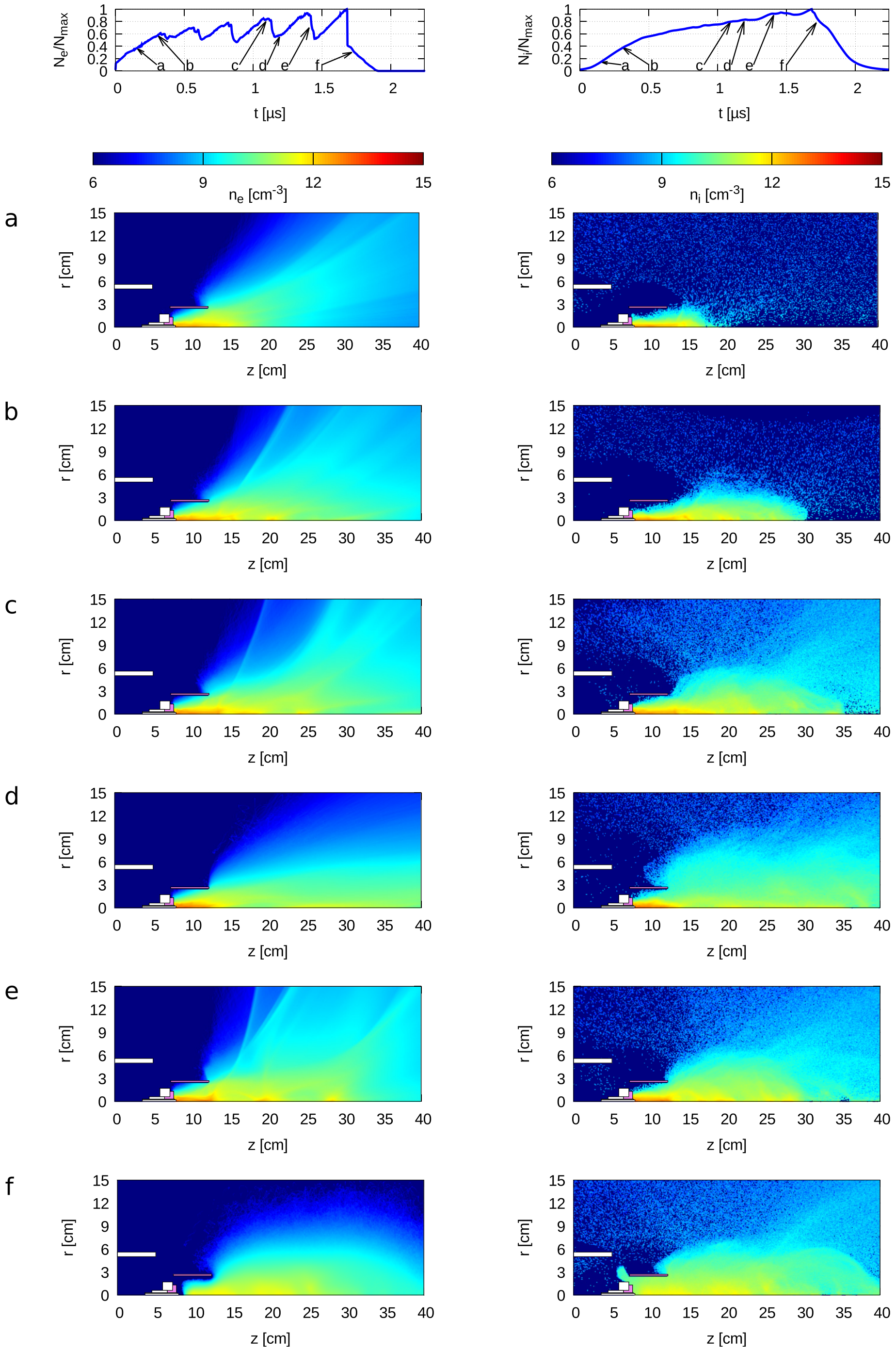

FIG. 2. Electron (left) and ion (right) densities for different time steps during a typical pulse.

the plasma loads again and the potential is again relatively constant with only small gradients. At time step (e), one large potential gradient builds up, the charge separation gets larger resulting in strong electric fields of more than 10 kV/m. The dynamics in the plume region is covered by the Poisson equation. Plasma dynamics determines the charge separation and by this the creation of electric fields. Charge separation is possible due to the higher mobility of electrons compared to ions. On longer timescales, quasi-neutrality of plasma will be reached, but for short timescales very high electric fields occur. These very high electric fields accelerate electrons to high velocities, which contribute to the thrust. In (f), the potential at the cathode is turned off, so that only a positive plasma potential remains. Very fast, all plasma particles leave the thruster and the potential approaches zero before starting with the next pulse. The resulting thrust of a complete run with four pulses is shown in Fig. 5.

The simulated thrust is diagnosed by collecting all particles leaving the thruster and their directed momentum in axial direction. This models the measurement from a pendulum thrust stand. The thrust is diagnosed at the end of the anode, where the thruster exit is located. It shows a pulsed and fluctuating characteristic as shown in Fig. 5 due to the mechanisms discussed before. The thrust in the simulation

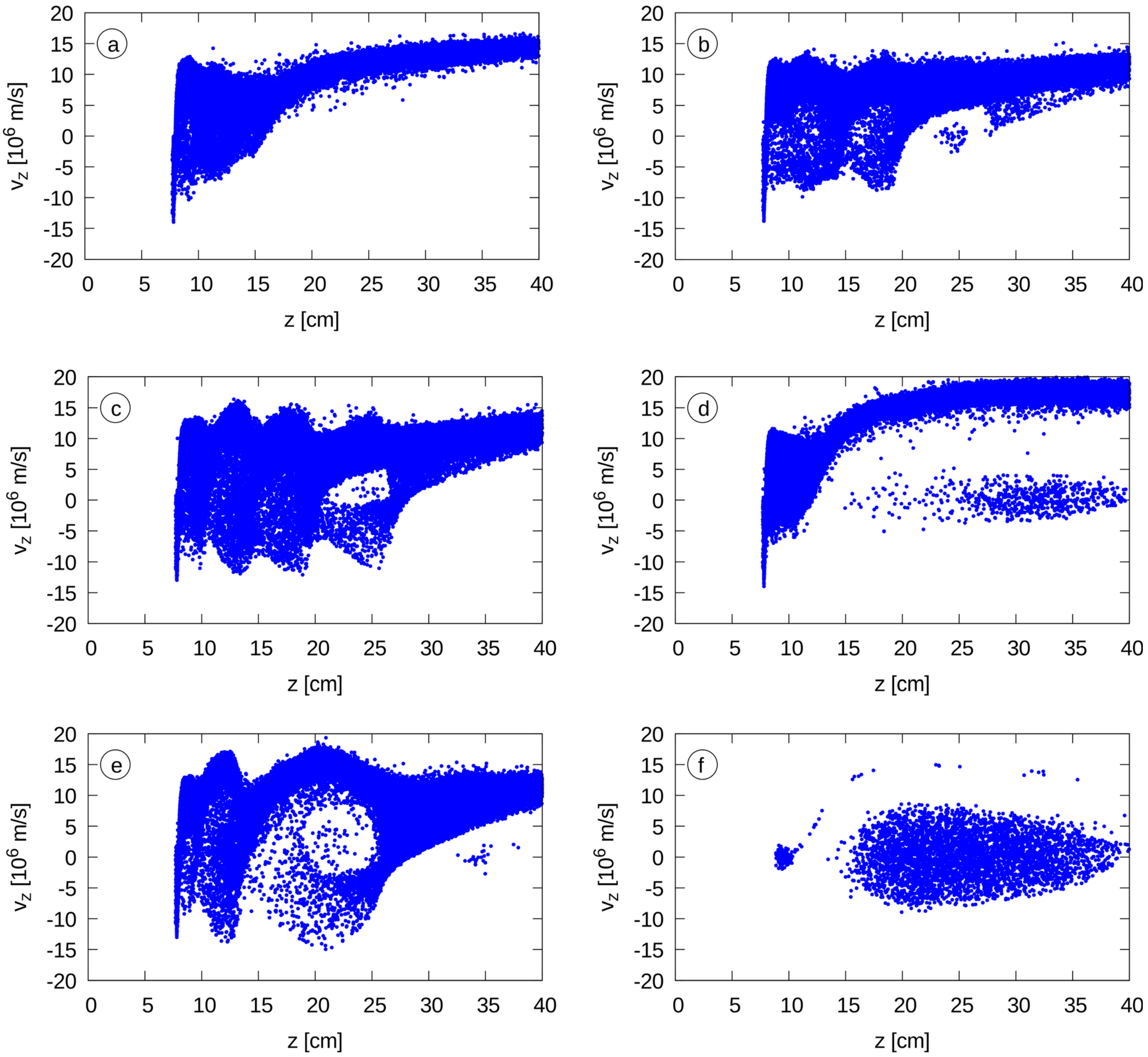

FIG. 3. Phase space of axial velocity as a function of axial position for electrons at different time steps for one pulse.

and in the experiment is of the order of 2 N. Experimentally such thrust values were reached for the same scenarios with currents of about 1 kA. This results in 0.2 mN/A.

V. DISCUSSION

The plasma dynamics in the simulation is similar to the experimentally observed one of cathodic arcs.[2,27,28] In the experiments, a narrow plasma beam appears as in the simulations. A narrow beam results in a high thrust efficiency due to a better directed stream. In addition, the interaction with other spacecraft components is minimized by a narrow beam. Comparing electron and ion density in the simulation, one can see a higher electron density in the plume. This gives a net electron current as measured in the experiment, not only due to the higher density, but due to the higher electron mobility.[29] This electron current is necessary to sustain the arc discharge experimentally, as it creates the conductive path for the capacitors driving the arc to discharge through the plasma, depositing energy into the plasma while generating more ionized species.[7] A net electron current is a helpful feature since it mitigates spacecraft charging issues due to charge expulsion.[30] Since ion and Hall effect thrusters are designed to extract and accelerate ions from a discharge plasma, they must also neutralize the exhaust stream; otherwise, the spacecraft would become more negatively charged until the ions return to the spacecraft, thus imparting no momentum. Since there is a net electron current, the spacecraft will gain a positive charge, which environmental electrons should be able to neutralize easily.[31] Thus, there is no need for charge neutralization systems, which will reduce system complexity, mass and failure modes in operational systems.

The calculated thrust in the simulation is in the region of a few Newton, due to the amount of current being modeled. As in the experiment the thrust is pulsed, with the thrust being dominated by ion production. The simulations described here simulate the action of individual cathode spots, while

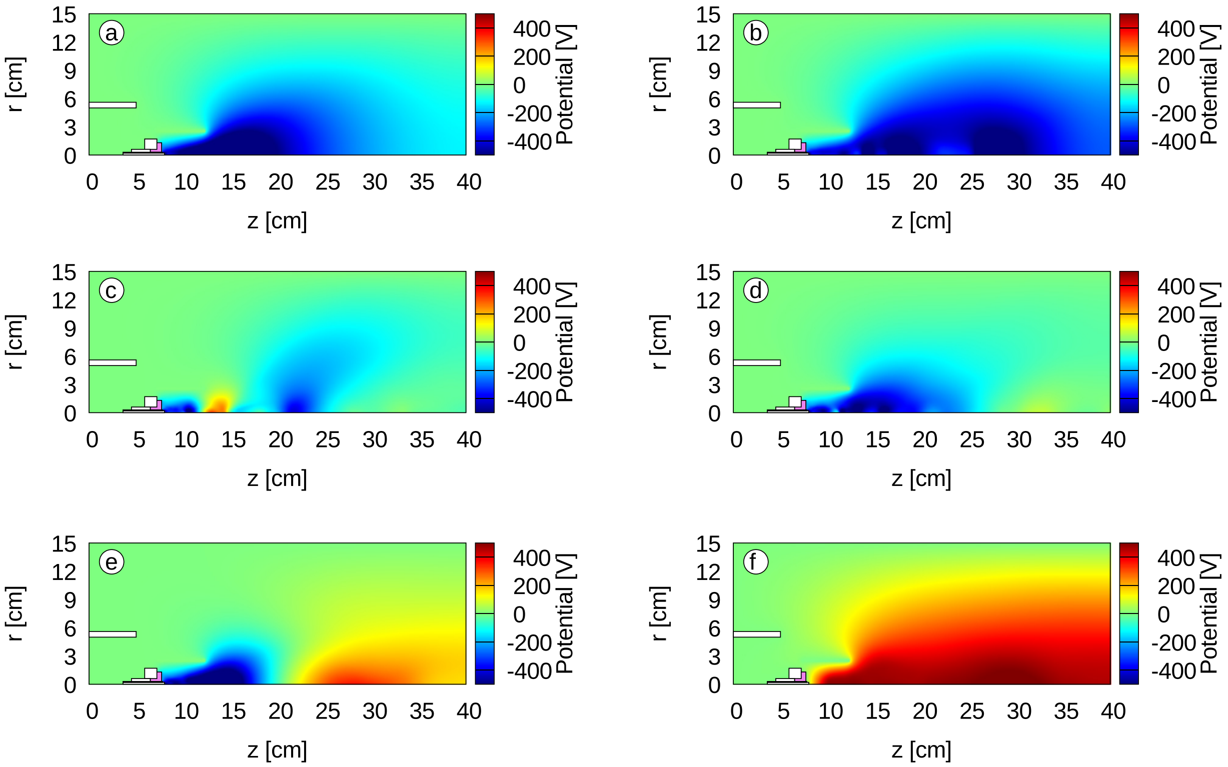

FIG. 4. Plasma potential for different time steps during a typical pulse.

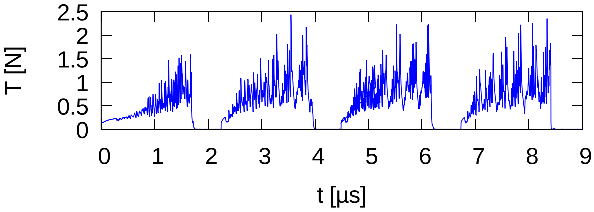

FIG. 5. Simulated thrust created by all species.

experiments with high current pulsed arcs tend to produce several tens of cathode spots; empirically, some 60…80 A of cathode current is carried by each cathode spot, and cathode current can peak at several kiloamps.[7] The actions of the various cathode spots reinforce each other, and so experimental generation of average thrusts on the order of Newtons is common.[1,2]

VI. CONCLUSIONS AND OUTLOOK

PIC simulations are widely accepted for plasma simulations; in particular, they are well-suited for simulations of electric thrusters. In this study, the PIC method was used to simulate the plasma dynamics of a pulsed cathodic arc thruster with a simplified wall model. This pulsed cathodic arc thruster was developed by Neumann Space. The simulation is able to reproduce basic features of the plasma observed in the cathodic arc thruster. Experimental diagnostics show similar results to the simulation, especially the strongly fluctuating currents and thrust. Analyzing in the simulation the phase space of the electrons, these fluctuations can be explained by a plasma-beam-instability. The strong fluctuations are beneficial for the operational characteristics of the arc thruster by increasing the thrust. In the future, PIC simulations can be used to study modified magnetic field configurations and their impact on the predicted performance of the arc thruster. To improve the code technically, the rather simplistic model of the surface model can be extended using a strategy as derived by Timko *et al.*[23]

The use of simulations to guide the experimental investigations is invaluable, as it permits a more rapid iteration and testing of prototypes while demonstrating which designs may not be worth exploring. The union of insights from simulation and data from experiment results in better science and engineering than either can do alone.

[1] P. R. C. Neumann, M. Bilek, and D. R. McKenzie, "A centre-triggered magnesium fuelled cathodic arc thruster uses sublimation to deliver a record high specific impulse," Appl. Phys. Lett. **109**, 094101 (2016).
[2] P. R. C. Neumann, M. M. M. Bilek, R. N. Tarrant, and D. R. McKenzie, "A pulsed cathodic arc spacecraft propulsion system," Plasma Sources Sci. Technol. **18**, 045005 (2009).
[3] J. Daalder, "Cathode spots and vacuum arcs," Phys. B: Condens. Matter **104**, 91–106 (1981).
[4] G. Y. Yushkov, A. Anders, E. M. Oks, and I. G. Brown, "Ion velocities in vacuum arc plasmas," J. Appl. Phys. **88**, 5618–5622 (2000).
[5] M. Bilek, D. McKenzie, and R. Powles, "Treatment of polymeric biomaterials by ion implantation," in *Biomaterials and Surface Modification* (Research Signpost, Kerala, 2007).
[6] O. Kalentev, K. Matyash, J. Duras, K. F. Lüskow, R. Schneider, N. Koch, and M. Schirra, "Electrostatic ion thrusters - towards predictive modeling," Contrib. Plasma Phys. **54**, 235–248 (2014).
[7] E. Hantzsche, "Mysteries of the arc cathode spot: A retrospective glance," IEEE Trans. Plasma Sci. **31**, 799–808 (2003).
[8] R. Fu, S. Kwok, P. Chen, P. Yang, R. Ngai, X. Tian, and P. Chu, "Surface modification of cemented carbide using plasma nitriding and metal ion

implantation," Surf. Coat. Technol. **196**, 150–154 (2005); in 13th International Conference on Surface Modification of Materials by Ion Beams (2005).

[9] P. R. C. Neumann, M. M. M. Bilek, and D. R. Mackenzie, "Optimising ion production in pulsed refractory and non-refractory cathodic arcs," in *Proceedings of the 12th Asia Pacific Physics Conference (APPC12)* (JPS Conference Proceedings, 2014), Vol. 1, p. 015059.

[10] J. E. Polk, M. J. Sekerak, J. K. Ziemer, J. Schein, N. Qi, and A. Anders, "A theoretical analysis of vacuum arc thruster and vacuum arc ion thruster performance," IEEE Trans. Plasma Sci. **36**, 2167–2179 (2008).

[11] L. Birdsall, *Plasma Physics via Computer Simulation* (CRC Press, 2004).

[12] D. Tskhakaya, K. Matyash, R. Schneider, and F. Taccogna, "The particle-in-cell method," Contrib. Plasma Phys. **47**, 563–594 (2007).

[13] D. Meeker, "Finite element method magnetics," FEMM **4**, 32 (2010).

[14] K. F. Lüskow, S. Kemnitz, G. Bandelow, J. Duras, D. Kahnfeld, P. Matthias, R. Schneider, and D. Konigorski, "Electrostatic particle-in-cell simulation of heat flux mitigation using magnetic fields," J. Plasma Phys. **82**, 595820502 (2016).

[15] F. Taccogna, S. Longo, M. Capitelli, and R. Schneider, "Self-similarity in hall plasma discharges: Applications to particle models," Phys. Plasmas **12**, 053502 (2005).

[16] H. Timko, F. Djurabekova, K. Nordlund, L. Costelle, K. Matyash, R. Schneider, A. Toerklep, G. Arnau-Izquierdo, A. Descoeudres, S. Calatroni, M. Taborelli, and W. Wuensch, "Mechanism of surface modification in the plasma-surface interaction in electrical arcs," Phys. Rev. B **81**, 184109 (2010).

[17] B. Jüttner, "Cathode spots of electric arcs," J. Phys. D: Appl. Phys. **34**, R103 (2001).

[18] B. E. Djakov and R. Holmes, "Cathode spot structure and dynamics in low-current vacuum arcs," J. Phys. D: Appl. Phys. **7**, 569 (1974).

[19] G. Mesyats, *Cathode Phenomena in a Vacuum Discharge: The Breakdown, the Spark, and the Arc* (Nauka, Moscow, 2000).

[20] R. Behrisch and K. Wittmaack, *Sputtering by Particle Bombardment* (Springer, Berlin, 1981), Vol. 1.

[21] J. Rager, A. Flaig, G. Schneider, T. Kaiser, F. Soldera, and F. Mücklich, "Oxidation damage of spark plug electrodes," Adv. Eng. Mater. **7**, 633–640 (2005).

[22] A. Anders, S. Anders, M. A. Gundersen, and A. M. Martsinovskii, "Self-sustained self-sputtering: A possible mechanism for the superdense glow phase of a pseudospark," IEEE Trans. Plasma Sci. **23**, 275–282 (1995).

[23] H. Timko, K. Ness Sjobak, L. Mether, S. Calatroni, F. Djurabekova, K. Matyash, K. Nordlund, R. Schneider, and W. Wuensch, "From field emission to vacuum arc ignition: A new tool for simulating copper vacuum arcs," Contrib. Plasma Phys. **55**, 299–314 (2015).

[24] J. Meichsner, M. Schmidt, R. Schneider, and H.-E. Wagner, *Nonthermal Plasma Chemistry and Physics* (CRC Press, 2012).

[25] A. B. Mikhailovskii, *Theory of Plasma Instabilities: Instabilities of a Homogeneous Plasma* (Consultants Bureau, 1974), Vol. 1.

[26] A. Akhiezer and Y. B. Fainberg, "On the interaction of a charged particle beam with electron plasma," Doklady Acad. Nauk SSSR **69**, 555–556 (1949).

[27] R. Sanginés, M. M. M. Bilek, and D. R. McKenzie, "Optimizing filter efficiency in pulsed cathodic vacuum arcs operating at high currents," Plasma Sources Sci. Technol. **18**, 045007 (2009).

[28] L. Ryves, D. R. McKenzie, and M. M. M. Bilek, "Cathode-spot dynamics in a high-current pulsed arc: A noise study," IEEE Trans. Plasma Sci. **37**, 365–368 (2009).

[29] J. Schein, N. Qi, R. Binder, M. Krishnan, J. K. Ziemer, J. E. Polk, and A. Anders, "Inductive energy storage driven vacuum arc thruster," Rev. Sci. Instrum. **73**, 925–927 (2002).

[30] D. M. Goebel and I. Katz, *Fundamentals of Electric Propulsion: Ion and Hall Thrusters* (John Wiley & Sons, 2008), Vol. 1.

[31] M. Tajmar, "Electric propulsion plasma simulations and influence on spacecraft charging," J. Spacecr. Rockets **39**, 886–893 (2002).

Plasma Physics and Technology **3**(2):66–71, 2016

SOLUTION OF POISSON'S EQUATION IN ELECTROSTATIC PARTICLE-IN-CELL SIMULATIONS.

Kahnfeld D.[a,*], Schneider R.[a,b], Matyash K.[a,b], Kalentev O.[c],
Kemnitz S.[b,d], Duras J.[e,a], Lüskow K.[a], Bandelow G.[a]

[a] *Ernst-Moritz-Arndt University Greifswald, Institute of Physics, Felix-Hausdorff-Str. 6, 17487 Greifswald, Germany*

[b] *Computing Center, Ernst-Moritz-Arndt University of Greifswald, D-17498 Greifswald, Germany*

[c] *Biomedizinische NMR Forschungs GmbH am Max-Planck-Institut für biophysikalische Chemie, D-37077 Göttingen, Germany*

[d] *University Rostock, Institute of Informatics, Albert-Einstein-Str. 22, 18059 Rostock, Germany*

[e] *Department of Applied Mathematics, Physics and Humanities, Nürnberger Institute of Technology, D-90489 Nürnberg, Germany*

[*] `kahnfeldd@uni-greifswald.de`

Abstract. In electrostatic Particle-in-Cell simulations of the HEMP-DM3a ion thruster the role of different solution strategies for Poisson's equation was investigated. The direct solution method of LU decomposition is compared to a stationary iterative method, the successive over-relaxation solver. Results and runtime of solvers were compared, and an outlook on further improvements and developments is presented.

Keywords: Particle-in-Cell, ion thrusters, Poisson's equation, LU decomposition, successive over-relaxation.

1. Introduction

For spacecrafts the concept of ion thrusters presents a very efficient method of propulsion. Ion thrusters generate a low thrust with much higher efficiency than chemical propulsion systems [1] and are commonly used on satellites in earth orbits.

Thrust is generated by accelerating ions of a plasma discharge and expelling them into space. The plasma within the thruster channel is dominated by electrostatic and magnetic fields, plasma-wall-interaction and non-linear effects. The shape and size of the plume have to be considered in the design of ion thrusters to account for possible damages caused by ion sputtering, but experimental access is difficult [1].

The HEMP-DM3a ion thruster design, as shown in fig. 1, possesses a rotational symmetry. The left boundary of the channel contains the anode with a voltage of 500 V, with the cathode supplied by an electron beam outside the channel which also serves as electron source and neutralizer for the expelled ions. The thruster channel is surrounded by permanent magnet rings of opposite magnetization. This results in a nearly constant magnetic field at the symmetry axis of the thruster with the exception of cusp regions, where two rings with opposite magnetization are located next to each other. The inner boundary of the thruster channel is made up of a dielectric ceramic consisting of Boron Nitrite which has a high threshold energy to reduce sputtering [2]. The thruster's exit is concluded with a grounded metal plate attached outside the dielectric. A more detailed description of the thruster can be found in [3].

Plasma simulations offer the means to understand the plasma physics within an ion thruster and can aid the design of new thruster concepts. A widely applied method is the Particle-in-Cell (PIC) scheme, simulating the trajectories of super-particles consisting of many real particles. Even with modern hardware, state-of-the-art features such as similarity scaling [4] and non-uniform grids [5] have to be used to make simulation of an ion thruster conceivable.

With the access to highly parallel computing clusters the best chance of gaining a speed-up of the simulation is an efficient parallelization. In order to achieve good scalability the communication overhead needs to be kept as small as possible, while load imbalance needs to be avoided by proper work distribution. One bottleneck for an efficient parallelization is the solution of Poisson's equation, which is often obtained by the use of traditional direct methods such as the Gauss algorithm. While very fast, such methods cannot be parallelized, and may lead to memory problems for large domain sizes. Therefore parallel solution strategies need to be investigated, one of which is the successive over-relaxation method.

2. Theory and code description

2.1. Basics of PIC

The Particle-in-Cell (PIC) method is a well-established scheme for simulation of plasmas. In PIC, so-called super-particles are moved within a simu-

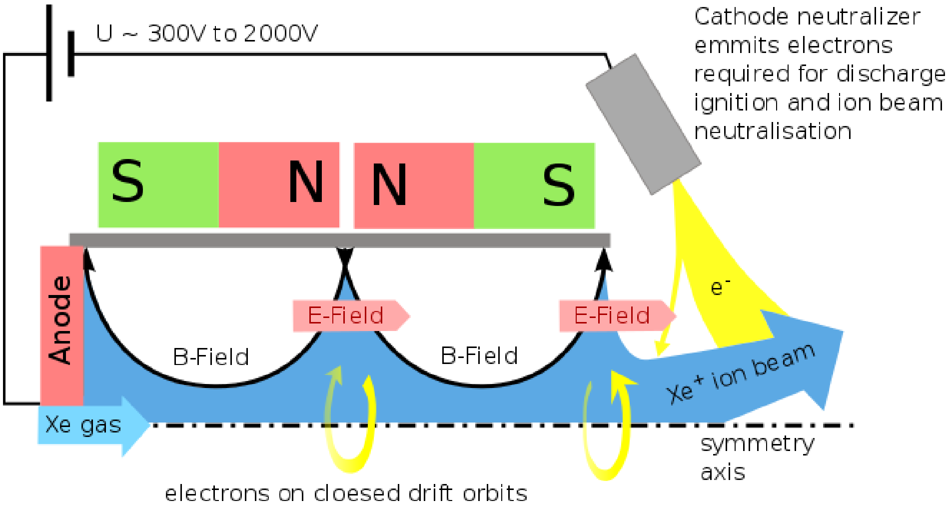

Figure 1. Schematic design of the HEMP-DM3a thruster.

lation domain, each representing a number of real particles. A grid is introduced, dividing the simulation region into cells, with macroscopic quantities such as the charge density n and the electrostatic potential ϕ being calculated only on the grid points. This enables treatment of large systems by calculating the electrostatic potential via Poisson's equation

$$\Delta\Phi(\vec{x},t) = -\frac{n(\vec{x},t)}{\varepsilon\varepsilon_0} \qquad (1)$$

only on the grid instead of N^2 direct particle interactions. Collisional effects are only taken into account within each cell separately.

The PIC cycle starts at a given time t_0 by initializing the system and calculating the macroscopic quantities on the grid points using the particle positions and velocities. The forces acting on the particles are calculated on the grid and then reassigned to each particle, resulting in a change of the particle's position and velocity. After calculating further particle interactions, i.e. collisions and surface interactions, the system is advanced by a discrete timestep Δt and returns to the start of the cycle. To assure stability, the timestep has to be chosen small enough to resolve the fastest particle movement. A more detailed description of the PIC method can be found in [6].

2.2. Finite difference scheme and solvers

To calculate the electric field on the grid, Poisson's equation has to be solved. The solutions will be acquired by introducing a finite difference scheme for the spatial second order derivatives. For a two dimensional $M \times N$ grid (x_i, y_j) with constant permittivity ε and charge density $n = n_i - n_e$ eq. 1 takes the form

$$\Delta\Phi = \mathrm{A}\Phi = -\frac{n}{\varepsilon\varepsilon_0}\,, \qquad (2)$$

creating a system of linear equations to be solved. The form of the matrix A depends on the discretization stencil that is used. The PIC code discussed here employs a five-point stencil leading to an accuracy of second order. Accuracy may be increased by incorporating more points into the difference scheme, i.e. by using a nine-point stencil, at the cost of increased computation time by additional matrix entries [7].

The resulting $(M\cdot N)\times(M\cdot N)$−dimensional matrix A has a characteristic block structure

$$\mathrm{A} = \begin{pmatrix} \mathrm{D} & \mathrm{B} & 0 & \cdots & 0 \\ \mathrm{B} & \mathrm{D} & \mathrm{B} & \ddots & \vdots \\ 0 & \mathrm{B} & \ddots & \ddots & 0 \\ \vdots & \ddots & \ddots & \ddots & \mathrm{B} \\ 0 & \cdots & 0 & \mathrm{B} & \mathrm{D} \end{pmatrix}.$$

The matrices D and B then have a dimension of $M \times M$. In the model case of a five-point stencil on a cartesian grid, D is tridiagonal with values of -4 as diagonal entries and values of 1 elsewhere. In that case, B is the unity matrix. In real applications the matrix structure is more complicated, as boundary conditions, non-constant permittivity ε or choice of geometry change the matrix structure. The case of radial coordinates, which is used in the PIC code discussed, is described more closely in [8]. Despite a more complex structure, basic matrix properties such as symmetry are preserved.

2.2.1. LU Decomposition

An often used method to solve systems of linear equations is the LU decomposition, also known as Gauss algorithm. Eq. 2 can be rewritten in the form

$$\mathrm{A}\Phi = b\,. \qquad (3)$$

The system can be solved by representing the matrix A as the product of an upper triangular matrix U and a lower triangular matrix L, transforming the equation to

$$\mathrm{A}\Phi = \mathrm{LU}\Phi = \mathrm{L}\tilde{\Phi} = b\,.$$

If L and U are known, the solution is easy. $\tilde{\Phi}$ is obtained by simply substituting the result of the previous lines into the next one as L has a triangular structure. The next step is to obtain Φ by solving for $\mathrm{U}\Phi = \tilde{\Phi}$ analogously. This step is also known as back-solve. For each back-solve, the complexity is $\sim (M \cdot N)^2/2$ [9], making it very efficient.

The problem lies in the computation of the decomposition A = LU which shall not be discussed in detail here, but a good review can be found in [9]. It can be shown that a LU decomposition exists for every regular matrix, but pivoting, interchanging rows and columns of the matrix in order to move the matrix elements with the highest absolute value to the diagonal, might be necessary, thus further increasing computation time. The complexity of the decomposition is $\sim (M \cdot N)^3/3$.

The Gauss algorithm is a very robust direct method to solve matrix equations. With the exception of rounding errors, which can be minimized by partial or full pivoting, it reliably delivers the right solution. In PIC the LU decomposition offers a reliable and efficient solver for the field solving step, as the matrix structure is well investigated. The decomposition is calculated at the beginning of code execution, as the matrix does not change throughout the execution of the code, and only the back-solve has to be computed every PIC cycle, hence giving a complexity of $\sim (M \cdot N)^2$ per PIC cycle.

However, a parallelization is problematic, as each line within a back-solve step depends on the results of the previous lines, limiting its application to a computational core. Parallel methods are only available for the calculation of the LU decomposition but not for the back-solve [10]. Therefore, in each PIC step it is necessary to reduce the charge densities onto a single core and then distribute the calculated electrostatic potential if the LU decomposition is used. The communication overhead created by this approach cannot be neglected on highly parallel systems.

2.2.2. Successive over-relaxation

On parallel systems, a frequently used method to solve eq. 2 is the use of a stationary iterative procedure. To formally obtain such procedures, eq. 3 is rearranged using a regular matrix B. The $(k+1)-$th iterate is then calculated as

$$\begin{aligned} \mathrm{A}\Phi = \mathrm{B}\Phi + (\mathrm{A}-\mathrm{B})\,\Phi &= b \\ \mathrm{B}\Phi^{k+1} + (\mathrm{A}-\mathrm{B})\,\Phi^k &= b \\ \Phi^{k+1} = \Phi^k - \mathrm{B}^{-1}\left(\mathrm{A}\Phi^k - b\right) &= F\left(\Phi^k\right)\,, \end{aligned}$$

The iterative procedure can be broken down to four steps:

i) Choose a starting point Φ^0.

ii) Calculate $\mathrm{A}\Phi^k$.

iii) Solve $\mathrm{B}\Delta\Phi^k = b - \mathrm{A}\Phi^k$.

iv) $\Phi^{k+1} = \Phi^k + \Delta\Phi^k$.

B is chosen to have a simple form in order to reduce the necessary number of operations and defines the iterative procedure. Also B is often linked to the matrix A. If it is chosen to be the diagonal of A, the algorithm is known as Jacobi algorithm. If B is chosen to be the sum of the A's diagonal matrix D (with $a_{ii} \neq 0$ for all i) and its lower triangular matrix L (not to be confused with the matrix used in the LU decomposition), the Gauss-Seidel algorithm, with the element index i, is acquired:

$$\begin{aligned} \mathrm{A} &= \mathrm{D} + \mathrm{L} + \mathrm{R} \\ \mathrm{B} &= \mathrm{D} + \mathrm{L} \\ \Phi^{k+1} &= -\left(\mathrm{D}+\mathrm{L}\right)^{-1}\left(\mathrm{R}\Phi^k - b\right) \\ \Phi_i^{k+1} &= \frac{1}{a_{ii}}\left(b_i - \sum_{j<i} a_{ij}\Phi_j^{k+1} - \sum_{j>i} a_{ij}\Phi_j^k\right)\,. \end{aligned} \tag{4}$$

This method is convergent if A is symmetric and positive definite [7]. It can be enhanced by introducing a relaxation parameter ω into the choice of B

$$\mathrm{B}(\omega) = \frac{1}{\omega}\left(\mathrm{D} + \omega\mathrm{L}\right)\,.$$

The algorithm is altered, giving

$$\begin{aligned} \Phi^{k+1} &= \Phi^k + \omega\left(\tilde{\Phi}^{k+1} - \Phi^k\right) \\ \tilde{\Phi}_i^{k+1} - \Phi_i &= \frac{1}{a_{ii}}\left(b_i - \sum_{j<i} a_{ij}\Phi_j^{k+1}\right. \\ &\qquad\left.\sum_{j>i} a_{ij}\Phi_j^k - a_{ii}\Phi_i^k\right) \end{aligned}$$

where $\tilde{\Phi}_i^{k+1}$ is calculated via eq. 4. If $\omega < 1$ this is called under-relaxation and can be used to dampen divergent solutions. For $\omega > 1$ the algorithm is known as successive over-relaxation (SOR) which is an often applied method to solve the finite difference scheme for Poisson's equation.

The iteration continues until a termination criterion is met. A possible choice is

$$\frac{\|\Phi^{k+1} - \Phi^k\|}{\|\Phi^{k+1}\|} < \delta$$

in a given vector norm $\|\cdot\|$. Because this criterion is critical for $\Phi^{k+1} \to 0$ the condition

$$\|\Phi^{k+1} - \Phi^k\|_{max} < \varepsilon$$

may be used as well. The maximum norm is chosen to minimize the necessary computational cost.

For the solution to converge, as the Gauss-Seidel algorithm depends on the newly calculated iterates, the domain should be divided into small subdomains, each solved separately. A chess board pattern, solving first all even and then all uneven grid points, or vice versa, may also be used.

It can be shown [7] that the SOR method is only convergent for $\omega \in (0, 2)$ and that the optimal relaxation parameter can be found in the interval $\omega_{opt} \in (1, 2)$. ω_{opt} can only be analytically calculated for a uniform grid spaced by Δ, as found in [7], but a decent guess is provided by the approximation

$$\omega_{opt} \approx 2 - \Delta \,.$$

The parameter is found in only a narrow range and has a large influence on the convergence rate, thus it needs to be tuned to the grid used. This can be achieved using simple optimization methods such as the hill-climb algorithm.

The complexity of each iteration step is $\sim (M \cdot N)^2$ and the expected number of iteration steps is $\sim (M \cdot N)$, giving the entire SOR method a complexity of $\sim (M \cdot N)^3$ [7]. The complexity is much higher compared to the back-solve of the LU decomposition which scaled quadratically.

The algorithm's structure allows for easy parallelization as the calculation of each point's iterate depends on only the surrounding points, delivering an advantage over LU decomposition. Only the boundary points have to be exchanged during each iteration step. For small subdomains, the communication overhead is kept relatively small.

2.3. Code description

The first simulations of the HEMP-T were performed by K. Matyash et. al. [11] and more recent results can be found in [12]. A 2d3v PIC scheme with radially symmetric 2D domain and a grid spacing of $\Delta z = \Delta r = 0.5\lambda_{D,e}$ on a domain of 1272×480 grid points was used. The particle velocities are treated in 3D. The timestep was chosen to be $\Delta t = 0.2/\omega_{P,e} = 1.2 \cdot 10^{-12}\,\mathrm{s}$ with about 10^6 timesteps necessary to reach a steady state. The simulated plasma consists of neutral Xenon gas, single positively charged Xenon ions and electrons. Particle collisions are simulated using a Monte-Carlo collisions scheme. The collisions include elastic Coulomb, excitation, ionization and elastic neutral-neutral collisions.

To reduce computational costs, similarity scaling as described in [4] is used, reducing the system size but keeping the physical laws intact as the mass-to-charge ration of each species is unchanged. A non-uniform mesh, further discussed in [5], is applied to the simulation region. The ions are moved once per $400\Delta t$ and neutrals are moved once per $2000\,\Delta t$.

A multigrid method incorporating two nested grids, as described in [12], is used for the calculation of the electrostatic potential Φ. A coarse grid covers the entire domain, with a larger grid spacing of $\Delta z_{coarse} = 4\Delta z_{fine}$, while the finer grid only covers the thruster region with a mesh of 888×236 grid points. During the field solve phase, a solution for Φ is first obtained on the coarse grid, with the boundary conditions of the finer grid given by the interpolated values on the coarse grid. Then a solution is obtained for the finer grid. The anode voltage is set to $500\,\mathrm{V}$ with a zero potential boundary condition at the upper and a no flux condition at the right boundary. For simplicity, only the solution of Poisson's equation on the fine grids will be discussed, as the behavior on the coarse grid is very similar.

The existing method for solving Poisson's equation is the Gauss algorithm included in the SuperLU library [10], calculating the LU decomposition once, only using the back-solve during each PIC timestep. Within the PIC code the SOR method was implemented as an alternative option to the SuperLU algorithm. The iteration procedure is executed until the termination condition $\|\Phi^{k+1} - \Phi^k\|_{max} < \varepsilon$ is met for two subsequent iterates Φ^{k+1} and Φ^k in dimensionless form. As the domain covers large areas with $\Phi = 0\,\mathrm{V}$, a relative termination condition is not well-suited here. The SOR method requires an initial guess at the start of the iteration, therefore SuperLU is executed once at the start-up of the code, and the solution will be stored as the initial guess of Φ during the first iteration. Alternatively, the SOR algorithm can also be used to obtain the initial guess, but this usually costs more computational time than the SuperLU method, when no parallelization is used. The solution of each following iteration is then stored and used as guess during the next field solve.

For testing of the solvers, a restarted run of the code, with charged particles covering the thruster channel and the exhaust region, is used. This simulated HEMP-T is in a steady state after 14 516 000 timesteps were computed. For the SOR method, the initial guess is a constant potential solution on the domain to ensure comparability. The PIC code and solvers discussed in this work are sequential, but the focus of this work lies on the investigation of an easy to parallelize Poisson solver.

3. Results

In fig. 2 the potential solution is plotted. It can be anticipated that the zero potential boundary conditions on the upper and the no-flux condition on the right boundary differ from the real situation, thus deviating the simulated potential and distorting simulation results. Therefore, a large simulation region for the plume is desirable, but increases computational cost, which can be made up for by introducing an efficient parallelization of the code.

For the SOR method, an ideal relaxation parameter of $\omega_{opt} = 1.981$ was obtained experimentally. A termination condition of $\varepsilon < 10^{-8}$ in dimensionless units was used, which corresponds to a change in potential of roughly $10^{-2}\,\mathrm{V}$, such that the influence of the potential difference on the system can be neglected. The absolute differences in the domain between the

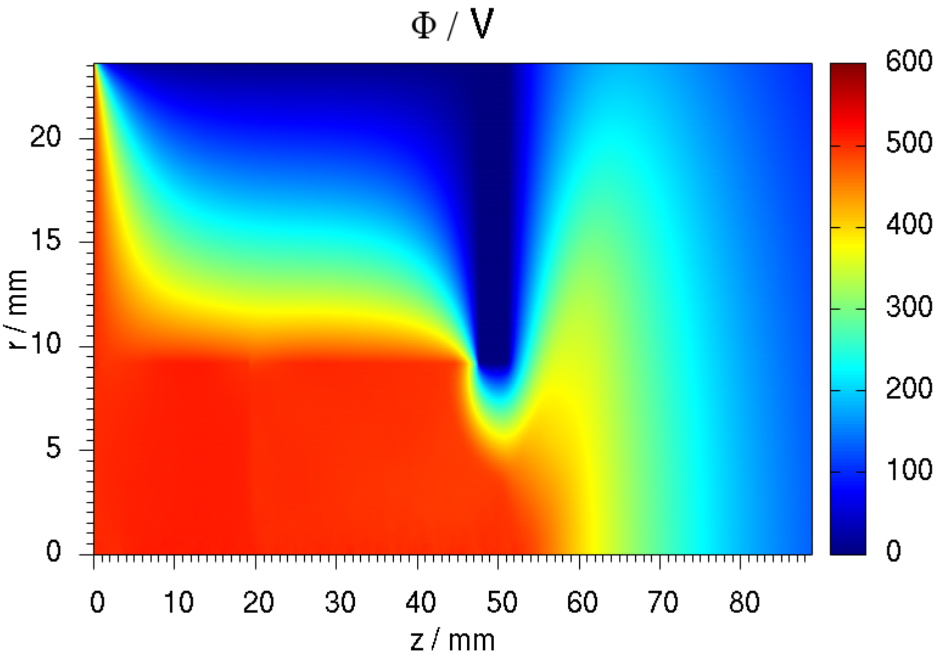

Figure 2. Solution of electrostatic potential in HEMP-DM3a obtained by the use of SuperLU package.

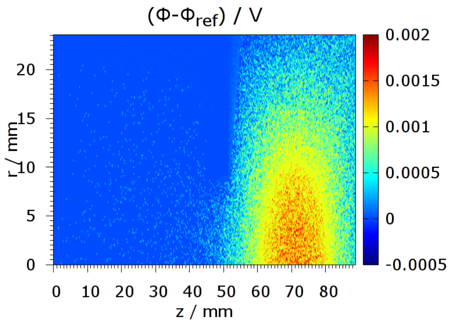

Figure 3. Comparison of solutions of SOR and SuperLU solvers with a termination condition of $\varepsilon < 10^{-8}$.

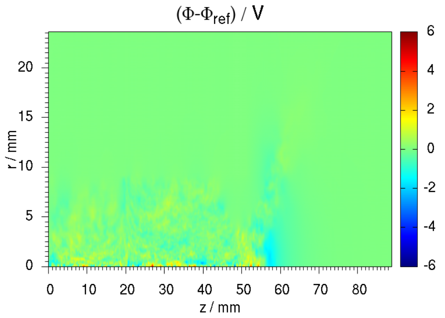

Figure 4. Comparison of solutions of SOR and SuperLU solvers with a termination condition of $\varepsilon < 10^{-8}$ after 9100 PIC steps, averaged over 100 steps

solution of the SOR and SuperLU methods is shown in fig. 3. The deviations are largest in the area of the thruster exit, where the potential gradient is largest. Still the differences are only of the order $\lesssim 10^{-2}$ V. In order to judge the applicability of the SOR method to PIC codes, one also needs to check the potential solution for a larger number of PIC cycles, to ensure that rounding errors will not be adding up in certain regions. Such a long-term comparison can be seen in fig. 4, where the absolute difference in potential after 9100 timesteps, averaged over 100 timesteps is presented. The differences are of the order of several Volts. The plot shows that deviations vary stochastically within the thruster channel and no systematic errors are adding up using the SOR method.

The runtime of the solvers differs drastically. Using the SuperLU back-solve, the execution time of one PIC cycle was just under one second, while one the same machine the time using the SOR solver was measured to be about 23 s per PIC cycle. For the long-term test presented in fig. 4, the overall execution time increased by a factor of 40. This shows the difference in scaling between the back-solve and the SOR method as described above.

4. Conclusions

The SOR method offers an alternative to traditional direct solution methods, i.e. LU decomposition, of Poisson's equation which occurs in finite difference discretizations within electrostatic PIC codes. For sequential code structures, this method is not recommended as its scaling is one order of magnitude worse than that of LU decomposition. On massively parallel systems however, the situation is different, as the LU back-solve cannot be parallelized, hence creating communication overhead and load imbalance and therefore limiting scalability of parallelizations. One choice of parallel solver would be the SOR method, with a trivial generalization to a multicore environment.

One problem that arises in parallelization of the SOR method is the exchange of domain boundaries within each iteration. For a high number of iterations this creates considerable communication overhead. A possible solution to this problem can be found by increasing computational cost of each iteration, with a reduction of total number of iterations. Multigrid methods [7] make use of the error smoothing property of stationary iterations, such as the Gauss-Seidel iteration, and usually converge within the order of ten iterations, making further investigations of such solvers within parallel PIC codes very attractive.

Acknowledgements

This work was supported by the German Space Agency DLR.

References

[1] Dan A. Goebel and Ira Katz. *Fundamentals of Electric Propulsion: Ion and Hall Thrusters* . JPL SPACE SCIENCE AND TECHNOLOGY SERIES. NASA, 2008.

[2] Norbert Koch, Martin Schirra, Stefan Weis, Alexey Lazurenko, Benjamin van Reijen, Jens Haderspeck, Angelo Genovese, Peter Holtmann, Ralf Schneider, Konstantin Matyash, and Oleksandr Kalentev. The HEMPT Concept - A Survey on Theoretical Considerations and Experimental Evidences . In *Proceedings of the 32nd International Electric Propulsion Conference*, number IEPC-2011-236, September 2011.

[3] Erfahrungsaustausch Oberflächentechnologie mit Plasma- und Ionenstrahlprozessen. *The HEMP Thruster - An Alternative to Conventional Ion Sources?*, volume X., march 2003.

[4] F. Taccogna, S. Longo, M. Capitelli, and R. Schneider. Self-similarity in Hall plasma discharges: Applications to particle models. *Phys. Plasmas*, 12:053502, 2005.

[5] Karl Felix Lüskow, Julia Duras, Oleksander Kalentev, Konstantin Matyash, David Tskhakaya, Jürgen Geiser, and Ralf Schneider. Non-equidistant Particle-In-Cell for Ion Thruster Plumes. In *Proceedings of the 33rd International Electric Propulsion Conference*, October 2013.

[6] D. Tskhakaya, K. Matyash, R. Schneider, and F. Taccogna. The Particle-In-Cell Method. *Contrib. Plasma Phys.*, 47(8-9):563–594, 2007.

[7] J. Stoer and R. Bulirsch. *Numerische Mathematik 2.* Springer Verlag, 5th edition, 2005.

[8] Konstantin Matyash, Ralf Schneider, Andreas Mutzke, Oleksandr Kalentev, Francesco Taccogna, Norbert Koch, and Martin Schirra. Kinetic simulations of SPT and HEMP thrusters including the near-field plume region, December 2009. First presented at the ICNSP'09.

[9] J. Stoer. *Numerische Mathematik 1.* Springer Verlag, 9th edition, 2005.

[10] Xiaoye S. Li. An overview of SuperLU: Algorithms, implementation, and user in- terface . *ACM Trans. Mathematical Software*, 31:302–325, September 2005.

[11] Konstantin Matyash, Ralf Schneider, Andreas Mutzke, Oleksandr Kalentev, Francesco Taccogna, Norbert Koch, and Martin Schirra. Kinetic Simulations of SPT and HEMP Thrusters Including the Near-Field Plume Region. *IEEE Transactions on Plasma Since*, 38(9, Part 1):2274–2280, SEP 2010.

[12] Karl Felix Lüskow. Physics of Ion Thrusters' Plumes . Master's thesis, University of Greifswald, July 2013.

Plasma Physics and Technology **3**(3):126–130, 2016

INFLUENCE OF ELECTRON SOURCES ON THE NEAR-FIELD PLUME IN A MULTISTAGE PLASMA THRUSTER

Duras J.[a,b,*], Schneider R.[a], Kalentev O.[d], Kemnitz S.[c,e], Matyash K.[c],
Koch N.[b], Lüskow K.[a], Kahnfeld D.[a], Bandelow G.[a]

[a] *Institute of Physics, Ernst-Moritz-Arndt University of Greifswald, D-17498 Greifswald, Germany*
[b] *Department of Applied Mathematics, Physics and Humanities, Nürnberger Institute of Technology, D-90489 Nürnberg, Germany*
[c] *Computing Center, Ernst-Moritz-Arndt University of Greifswald, D-17498 Greifswald, Germany*
[d] *Biomedizinische NMR Forschungs GmbH am Max-Planck-Institut für biophysikalische Chemie, D-37077 Göttingen, Germany*
[e] *University Rostock, Institute of Informatics, D-18059 Rostock, Germany*
[*] `julia.duras@uni-greifswald.de`

Abstract. In order to obtain a better understanding of the near-field plume of a multistage plasma thruster, the influence of an external electron source is investigated by Particle-In-Cell simulations. The variation of the source position showed a strong influence of the magnetic field configuration on the electron distribution and therefore on the plume plasma. In the second part of this work, higher energetic electrons were injected in order to model collision-induced diffusion in the plume. This broadens the electron distribution, which leads to a more pronounced divergence angle in the angular ion distribution.

Keywords: Multistage plasma thruster, near-field plume, external electron source, Particle-In-Cell.

1. Motivation

Ion thrusters with magnetic plasma confinement can be optimized by modifying magnetic field configuration, anode potential, neutral gas source and neutralizer properties. In the case of neutralizer adjustment, mainly the plume behavior is influenced. For a better understanding of the near-field plume physics, the influence of an external electron source on its properties is studied. Here, position and source distribution are varied and the interaction between magnetic field, potential and plasma densities are investigated.
For this purpose a multistage plasma thruster similar to the HEMP thruster [1], [2] was simulated with the Particle-In-Cell method.

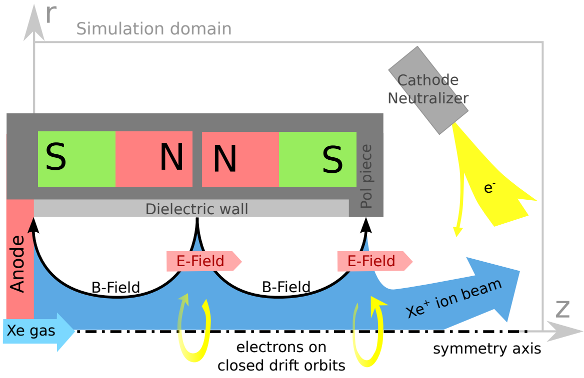

Figure 1. Scheme of HEMP-like thrusters, similar to [3].

2. Physics of a multistage plasma thruster

A multistage plasma thruster consists of a rotationally symmetric discharge channel with an anode and an inlet for the propellant at the upstream end, as shown in figure 1. The discharge channel is surrounded by axially magnetized permanent magnet rings with opposite magnetization. Inside the thruter channel a dielectric wall is facing the plasma. At the exit a grounded pole piece is placed. Outside the thruster channel a hollow cathode neutralizer is placed. It provides the thruster with starter electrons for igniting the discharge and neutralizes the out-going ion beam. The permanent magnets generate a magnetic field which points mainly in axial direction especially in the channel region next to the symmetry axis. In the so-called cusp regions, the magnetic field next to the channel wall is mostly directed in radial direction. In figure 1 three cusps are shown, an anode cusp, an inner cusp and an exit cusp. The magnetic field strength B is chosen such that the Larmor radius of the electrons is much smaller than the radius of the discharge channel, while for the ions it is larger $r_{\mathrm{L,e}} \ll R < r_{\mathrm{L,i}}$. Therefore, in the thruster channel electrons are magnetized while ions are not. Electrons are created by the neutralizer acting as cathode and experience close to the axis a magnetic field nearly parallel to the axis which directs them towards the anode.
The cusp-structure of the magnetic field builds up

a magnetic mirror in front of the thruster exit. In combination with the potential drop, this magnetic mirror lets the electrons oscillate in a confined electron cloud in the plume originating from the electron source pointing towards the thruster's exit. In the cusp regions, the perpendicular electric and magnetic fields induce a $\vec{E} \times \vec{B}$-drift to the electrons in poloidal direction. In addition the magnetic field configuration builds up a magnetic mirror in radial direction and the electrons are reflected before they reach the channel wall. The strong radial magnetic field in these regions separate the different thruster regions. Only few electrons can overcome these regions by collisional and anomalous transport, which is caused by electrostatic turbulence [4]. By this, electron density is increased in the respective downstream cusp region and allows for efficient ionization of the propellant. In the channel regions between the cusps, the electron transport is determined in axial direction by the fields and in radial direction by collisional transport. Therefore, in the regions where no cusps are existing electron losses at the dielectric wall are low and the non-magnetized ions can generate a positive surface charge. The dominance of the axial transport along the magnetic field lines quickly compensates small perturbations of the electric potential and results in a flat potential inside the discharge channel with only small steps at the regions with large radial transport, namely at the cusps. Xenon ions follow the potential gradients and are getting accelerated mostly in the potential drop of the thruster exit. Within the acceleration channel the radial potential gradients towards the wall are rather small and the ion energies are kept below the sputter threshold, hence minimizing erosion. The different dynamics for electrons and ions lead to a spatial separation of ionization in the channel and acceleration at the thruster exit. In order to produce an ion beam with small divergence angle, a grounded magnetic pole piece is placed at the exit cusp. The magnetic field lines are focused in this region and the grounded potential produces in radial direction a large potential drop of $\Delta\phi = eU_\mathrm{a}$. This guides the electrons to enter the thruster channel and get confined only close to the symmetry axis, which creates an ion lens. The resulting ion beam is strongly affected by the potential structure in this region as well as in the near-field plume region. Here, the magnetized electrons are determining the potential and therefore influencing the ion trajectories.

Therefore, the thruster magnetic field topology and the potential in the plume are important for optimization of the ion beam divergence. Different external electron source positions might change the electron distribution in the plume and therefore potential and angular ion distribution.

3. Code description and simulation set-up

The non-Maxwellian characteristics of the electron distribution function in the thruster requires a kinetic method [5]. Due to the rotational symmetry of the system, the spatial domain was reduced to r-z and an electrostatic 2d3v Particle-In-Cell code with Monte Carlo collisions (PIC MCC) [6], [4] was used. In this PIC-MCC simulation we follow the kinetics of so-called Super Particles (each of them representing many real particles), moving in the self-consistent electric field calculated on a spatial grid by solving Poisson's equation. The particle collisions are treated by Monte Carlo Collision (MCC) routines. All relevant collisions are included in the model: electron-electron Coulomb, electron-neutral elastic, ionization and excitation collisions, ion-neutral momentum transfer and charge exchange collisions. The dynamics of the background neutral gas is self-consistently resolved by Direct Simulation Monte Carlo [7]. Plasma surface interactions are provided by a Monte Carlo erosion module. For electrons an anomalous transport model is applied [8]. In order to reduce the computational time a similarity scaling is applied with a factor of 10 [9].

In figure 1, the simulation domain and the thruster geometry are shown. The thruster has a channel radius of $R = 9\,\mathrm{mm}$ and length of $L = 51\,\mathrm{mm}$. The main part of the channel wall is dielectric, at the exit a grounded magnetic pole piece terminates the thruster channel. At the anode a potential of $U_\mathrm{a} = 500\,\mathrm{V}$ is applied. The simulated domain consists of a fine grid of 890×240 cells with a grid spacing of $\Delta r = \Delta z = 0.5\lambda_{D,e} = 0.01\,\mathrm{mm}$ containing the thruster channel and the near field plume. It is overlaid by a courser grid of four times larger cell size, covering the whole domain. The potential boundary condition at the symmetry axis and at the right hand side of the domain is set to zero radial electric field, while at other domain boundaries Dirichlet boundary conditions with $\phi = 0\,\mathrm{V}$ or $\phi = U_\mathrm{a}$ are applied. For the grounded magnetic pole piece the potential is set to zero. The solution at the domain boundary between fine and coarse mesh is transferred explicitly by boundary conditions between the two meshes.

4. Results

4.1. Influence of the electron source position

Within PIC ion thruster simulations, the resolved domain is usually too small to simulate the neutralizer at the position of the experiment. Due to the magnetization of the electrons the usage of an effective source, placed at the same magnetic field line as the neutralizer is used. The external source is simulated as a volume source of size $4\,\mathrm{mm} \times 4\,\mathrm{mm}$ with Maxwellian distributed electrons of a temperature of $T_\mathrm{e} = 2\,\mathrm{eV}$ and a cathode current of $I_\mathrm{cath} = 1.5\,\mathrm{mA}$.

Four different source positions were chosen in order

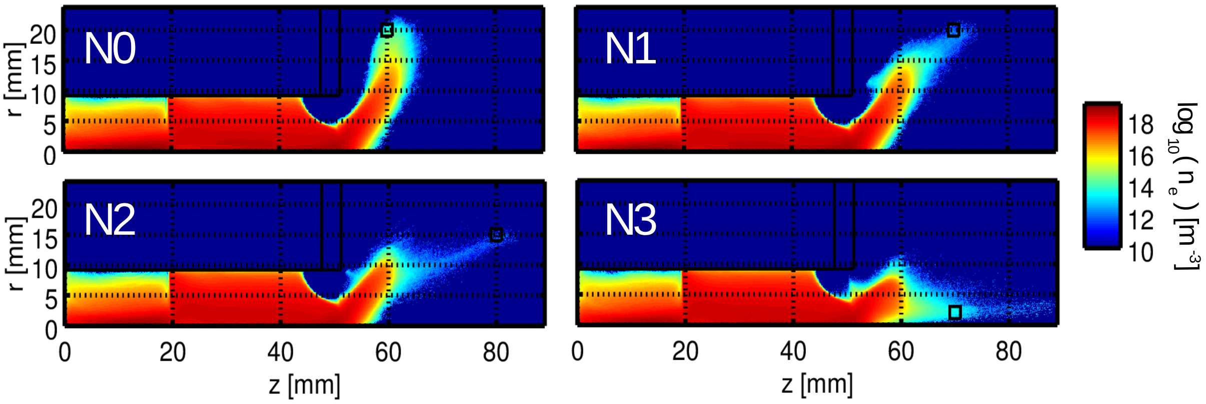

Figure 2. Electron density in logarithmic scale for different source positions.

to study its influence on the plume plasma. In figure 2 the resulting electron density is shown and the black box in the plume indicates the electron source position. The magnetic field lines where the sources N0 and N1 are located, are connected to the front of the metal cap. Sources N2 and N3 aim at the thruster exit. The positions where also chosen to represent different magnetization strengths of the source electrons. While the B-field strengths at positions N1 and N3 are similar, it is nearly doubled at N0 and nearly the half at N2.

In figure 2 the electron density for the different source position is shown in logarithmic scale. The simulated time to reach steady state was in the range of 2–6 µs, which corresponds to a computation time of 20 up to 60 days. For the four cases the channel plasma is practically not changing. At 20 mm the central cusp is clearly visible, as well as the dominant axial transport by the magnetic field lines close to the z-axis, which produces a higher density. Due to the electron loss at the anode, the region between anode and central cusp is less filled than the region between the central and exit cusp, where both cusps act as sources of energetic electrons.

For the sources N0–N2, the electron distribution in the near-field plume and close to the exit is changing only in the low density range. The electron density in the range of $10^{18}\,\mathrm{m}^{-3}$, shown in red, is nearly constant. This distribution is built up by trapped electrons, oscillating between the magnetic mirror and the potential drop. For N2, with lowest magnetic field strength at its source position, electrons are getting accelerated by the potential, which results in a lower density. It increases in the region of higher B due to oscillation in the magnetic trap. In the case of N0, with highest magnetic field strength at the source position, this appears already in the source region and increases with increasing B. The electron distribution formed by source N1 shows a mixture of these two cases.

Electrons injected by source N3 fill in a wider area due to the magnetic field configuration in this region.

Since the differences of the electron distribution generated by sources N0, N1 and N2 are only visible in the low density range, the resulting potentials are quite similar. Only the source position of N3 close to the axis shows an electron distribution expanded towards the symmetry axis. Therefore, the resulting potential, in the first row in figure 3, is given for N0 and N3. It clearly shows a flat potential in the channel, which drops in the plume. At the thruster exit the metal wall is forming a potential drop in radial direction which acts as a lens for the non-magnetized ions. For N3, in comparison to N0, the potential distribution in the plume is compressed in radial direction and stretched in axial direction. This is a result of the broader electron distribution close to the symmetry axis.

Since the ions are not magnetized they follow the potential gradient which determines their angular distribution. At the bottom row in figure 3 the corresponding ion densities for electron source N0 and N3 are shown in logarithmic scale. Within the channel the distribution satisfies very well quasi-neutrality, as expected for a plasma. At the thruster exit the potential drop accelerates the ions into the plume. Due to the different electron distributions in the plume, for N0 the distribution of higher ion density is expanding deeper into the plume than for N3. For the angular ion distribution, the influence of the different electron sources is minor, since in both cases ions show a broad distribution. Only close to the symmetry axis the contribution is higher for N3.

The magnetic field configuration in front of the thruster exit determines the distribution of electrons in the plume, whereas the source position influences the ion distribution in the plume only slightly.

4.2. Thermal versus beam-like electron source

Due to the long run time of PIC simulations, it is not possible to represent the full electron dynamics. In the plume electron and neutral density are two orders lower than in the channel with a typical Coulomb collision time of about 50 µs. Typically, for a runtime of

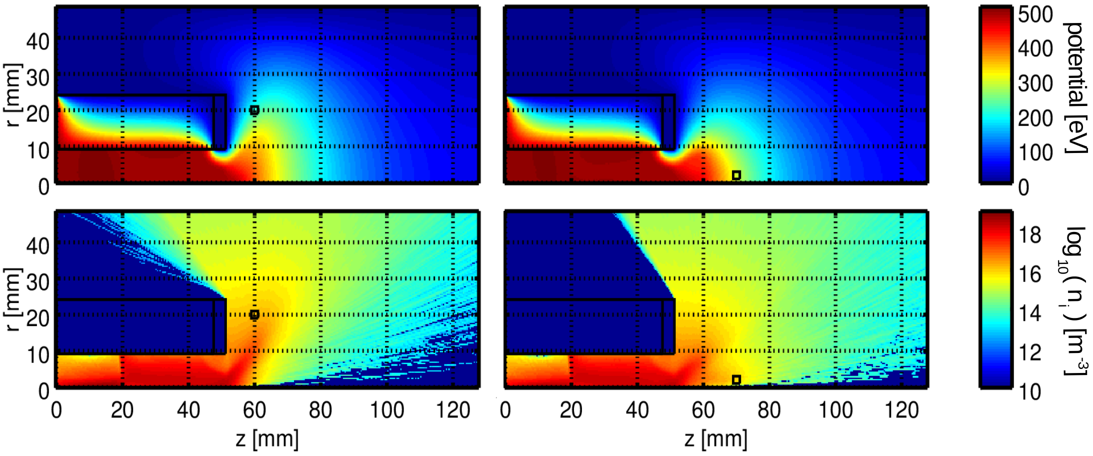

Figure 3. Potential and ion density generated by electron source N0 and N3. The ion density is given in logarithmic scale.

1 month a simulated time in the range of some micro seconds is possible, which does not resolve collision-induced electron diffusion. Therefore, the filling of the plume with electrons guaranteeing quasi-neutrality is not appearing as observed experimentally, as this happens only on the time-scale of collisional transport. In order to investigate this effect an electron beam directed away from the thruster is used as external source. Electrons with a higher velocity have a larger Larmor radius, which broadens their distribution in the plume. To further reduce the influence of the magnetic mirror the source is placed in a region of low magnetic field strength, similar to the one at the source position of N2. The injected electron beam has a thermal energy of 0.1 eV and a drift velocity of 20 eV. It is directed down-stream the thruster plume, with an angle of 55° with respect to the symmetry axis. As before the cathode current is set to $I_{\mathrm{cath}} = 1.5\,\mathrm{mA}$. The resulting electron density, potential and ion density are shown in figure 4. Densities are given in logarithmic scale. The black box in the plume indicates the electron source position.

As in the previously studied cases, the shape of the electron distribution in the plume remains very similar. But due to the higher probability to cross magnetic field lines, the distribution is broader. Since the magnetic field lines guide the plume electrons into the thruster this results in a higher density at the thruster exit, which increases the collisional rate, filling up the channel volume. As can be seen in the potential plot in figure 4, the increased electron density in the plume extends the potential drop. This affects the ions, which just follow the potential gradients, and a beam with a more pronounced shape and a dedicated peak at around 60° divergence angle is developing. Due to the higher electron density in the channel and close to the exit, the ionization rate increases which increases the ion density, as can be seen in the bottom plot in figure 4.

In figure 5 the angular current distribution with respect to the symmetry axis is given for the two thermal sources N0 and N3 as well as for the beam-like electron source. This distribution is calculated at the outer domain boundary and the angle vertex refers to the thruster exit $z = 51\,\mathrm{mm}$ at $r = 0\,\mathrm{mm}$. It is given in ion current density within 5° normalized to the total measured ion current density. Both thermal sources produce a flat angular distribution, where for source N3, the higher ion density close to the symmetry axis contributes more at low angles. The more extended electron distribution in the plume generated by the beam-like source directed away from the thruster produces a clear ion beam. This is a characteristics which is also seen in experiments [8].

5. Conclusion

In this work the influence of external electron sources on the plume in a multistage plasma thruster was studied. A strong impact of the magnetic field on the electron distribution in the near field plume was observed, especially due to the magnetic mirror effect. The electron distribution was insensitive to the source position in case of a thermal electron source. Only an effective source close to the symmetry axis increases the electron density close to the axis, which leads to higher contribution in the angular current distribution at small angles. In order to overcome calculation time limits and to represent electron diffusion in the plume by collisions, a source of higher energetic electrons directed away from the source was simulated. This produces a broader distribution in the plume, its shape determined by the magnetic field lines. The broader filling produces a more extended potential drop, which generates a pronounced ion beam.
In the experiment this effect might be further increased due to a higher neutral background pressure. Also, secondary electrons produced by impinging ions at the vacuum vessel walls can influence the electron

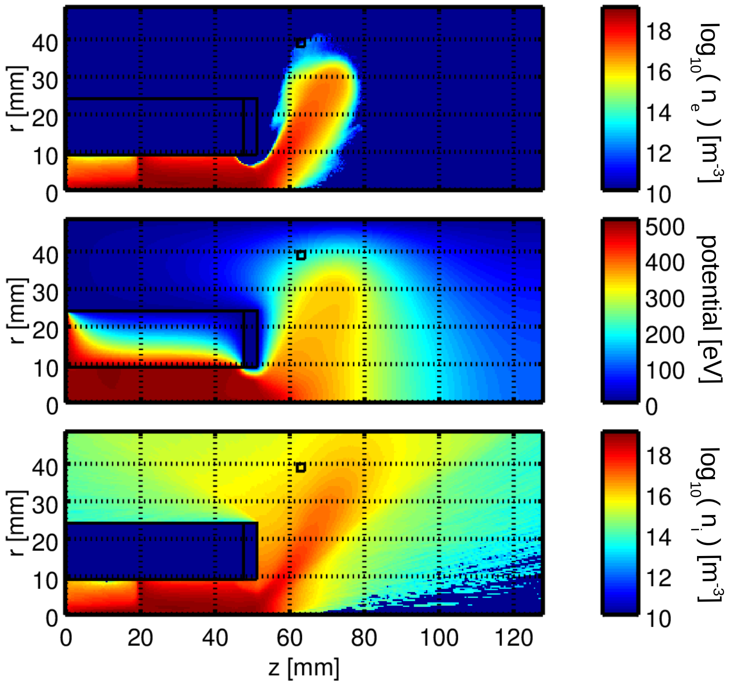

Figure 4. Electron density, potential and ion density for a beam-like electron source directed away from the thruster.

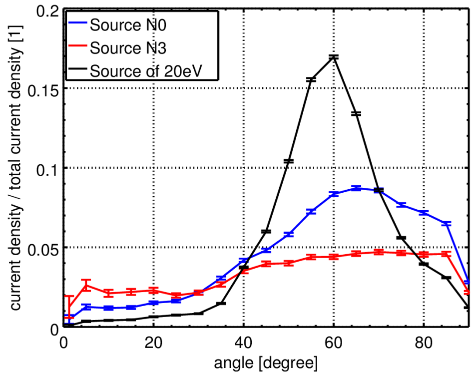

Figure 5. Angular current distribution with statistic error bars and angle given with respect to the symmetry axis.

distribution in the plume acting as additional near-axis source. Due to the magnetic field lines such electrons are guided towards the symmetry axis and would rise the angular current distribution at lower angles.

Acknowledgements

This work was supported by the ”ITSim - Skalierung von Ionentriebwerken mittels numerischer Simulation” project of the Bavarian State Ministry of Education Science and the Arts and the German Space Agency DLR.

References

[1] G. Kornfeld, H. Seidel, and J. Wegener et al. Plasma Accelerator Arrangement, 1999. Priority: Germany No. 198 28 704.6, filed 26 June 1998.

[2] N. Koch, M. Schirra, and S. Weis et al. The HEMPT Concept - A Survey on Theoretical Considerations and Experimental Evidences . In *Proceedings of the 32nd International Electric Propulsion Conference*, number IEPC-2011-236, 2011.

[3] N. Koch, H.P. Harmann, and G. Kornfeld. Development and Testing Status of the THALES High Efficiency Multistage Plasma (HEMP) Thruster Family. In *Proceedings of the 29nd International Electric Propulsion Conference*, number IEPC-2005-297, 2005.

[4] O. Kalentev, K. Matyash, and J. Duras. Electrostatic Ion Thrusters - Towards Predictive Modeling . *Contributions to Plasma Physics*, 54:235–248, 2014.

[5] Karl Felix Lüskow. Physics of Ion Thrusters' Plumes . Master's thesis, University of Greifswald, July 2013.

[6] K. Matyash, R. Schneider, and A. Mutzke et al. Kinetic Simulations of SPT and HEMP Thrusters Including the Near-Field Plume Region. *IEEE Transactions on Plasma Since*, 38(9, Part 1):2274–2280, 2010.

[7] R. Procassini, C. Birdsall, E. Morese, and Cohen B. A relativistic monte carlo binary collision model for use in plasma particle simulation codes. *Memorandum No. UCB/ERL M87/24, University of California, Berkeley*, 1987.

[8] K. Matyash, O. Kalentev, and R. Schneider et al. Kinetic Simulation of the stationary HEMP thruster including the near-filed plume region. In *Proceedings of the 31st International Electric Propulsion Conference*, number IEPC-2009-110, September 2009.

[9] F. Taccogna, S. Longo, M. Capitelli, and R. Schneider. Self-similarity in Hall plasma discharges: Applications to particle models. *Phys. Plasmas*, 12:053502, 2005.

J. Plasma Phys. (2017), *vol.* 83, 595830107 © Cambridge University Press 2017 1
doi:10.1017/S0022377817000125

Ion angular distribution simulation of the Highly Efficient Multistage Plasma Thruster

J. Duras[1,2,†], D. Kahnfeld[2], G. Bandelow[2], S. Kemnitz[3], K. Lüskow[2], P. Matthias[2], N. Koch[1] and R. Schneider[2]

[1]Nuremberg Institute of Technology, D-90489 Nuremberg, Germany

[2]Institute of Physics, University of Greifswald, D-17498 Greifswald, Germany

[3]Institute of Computer Science, University of Rostock, D-18059 Rostock, Germany

(Received 18 July 2016; revised 16 January 2017; accepted 16 January 2017)

Ion angular current and energy distributions are important parameters for ion thrusters, which are typically measured at a few tens of centimetres to a few metres distance from the thruster exit. However, fully kinetic particle-in-cell (PIC) simulations are not able to simulate such domain sizes due to high computational costs. Therefore, a parallelisation strategy of the code is presented to reduce computational time. The calculated ion beam angular distributions in the plume region are quite sensitive to boundary conditions of the potential, possible additional source contributions (e.g. from secondary electron emission at vessel walls) and charge exchange collisions. Within this work a model for secondary electrons emitted from the vessel wall is included. In order to account for limits of the model due to its limited domain size, a correction of the simulated angular ion energy distribution by the potential boundary is presented to represent the conditions at the location of the experimental measurement in 1 m distance. In addition, a post-processing procedure is suggested to include charge exchange collisions in the plume region not covered by the original PIC simulation domain for the simulation of ion angular distributions measured at 1 m distance.

Key words: plasma applications, plasma simulation

1. Motivation

For ion thrusters, the angular ion distribution in terms of ion current, charge state and energy is an important parameter since it determines the thrust efficiency of the propulsion system. It is also one of the few thruster characteristics that can be accessed experimentally to validate numerical plasma simulations.

In the present study, numerical simulations are performed for the Highly Efficient Multistage Plasma Thruster (HEMP-T), patented by the THALES group in 1998 (Kornfeld, Seidel & Wegener 1998). As described in Koch, Harmann & Kornfeld (2007), HEMP-Ts consist of a dielectric, rotationally symmetric discharge channel with an anode and a propellant inlet located at the upstream end and a hollow cathode neutraliser placed at the thruster exit. The discharge channel is surrounded

---

† Email address for correspondence: julia.duras@th-nuernberg.de

by a system of axially magnetised permanent magnet rings in opposite magnetisation, forming a multi-cusp structure. The level of magnetic induction at any position within the thruster channel is chosen such that the Larmor radius of the electrons is much smaller than the geometrical dimensions of the discharge channel. While the propellant ions are hardly affected by the magnetic field due to their much higher mass, electrons are efficiently confined and only few electrons are lost to the wall, mostly at the cusps. In this work an older prototype model named DM3a is discussed. It has three cusps, the anode, the central and the exit cusp and is described in Kornfeld, Koch & Harmann (2007). An anode potential of $U_a = 500$ V is applied.

Numerical simulations show a typical neutral particle density in the channel is $n_n = 10^{20}\ \mathrm{m}^{-3}$ with a neutral temperature of $T_n = 700$ K. Typical plasma parameters are a plasma particle density of $n_{e,i} = 10^{18}\ \mathrm{m}^{-3}$, with a temperature of approximately $T_e = 4$ eV and $T_i = 1$ eV. While the ions in the channel are nearly thermalised, the electrons have an additional drift velocity of approximately $10^4\ \mathrm{m\ s}^{-1}$ towards the anode. Inside the thruster channel the electron Debye length is $\lambda_{D_e} = 7.4\ \mu\mathrm{m}$, the electron plasma frequency is $\omega_{p,e} = 1.8 \times 10^{11}$ Hz and the electron mean free path is in the range of the channel length of 50 mm. This motivates kinetic simulations rather than a fluid approach for the electrons. The electrostatic approximation can be used, because the magnetic fields connected with the internal plasma currents are negligible compared to the static magnetic fields from the magnets. A strong coupling of the channel and plume plasma requires a simulation of both regions. In the plume, the plasma densities are decreased by at least 4 orders of magnitudes and the ion kinetic energy is increased to $E_{kin,i} = 500$ eV, as a consequence of the accelerating potential drop close to the exit.

A widely applied kinetic method is the particle-in-cell (PIC) scheme with Monte Carlo collisions (PIC-MCC), simulating the trajectories of super-particles consisting of many real particles. It requires the resolution of the smallest length scale of the system, usually the Debye scale, and the shortest time scale of the system, usually the plasma frequency, resulting in small domain sizes in the mm range and short simulated run times of approximately some µs. Since angular ion distributions are typically measured at a distance of tens of centimetres to some metres from the thruster exit, it is necessary to introduce proper mapping functions to transfer the results of the kinetic model to these positions. The computational requirements for such a fully kinetic model are quite demanding in memory and run time. Therefore, after a short description of the PIC-MCC code, a possible parallelisation strategy is discussed in § 2. Afterwards, the simulated angular distribution of ion current and energy is described in detail in § 3 and compared with experimental data.

2. Code description and parallelisation strategy

The non-Maxwellian characteristics of the electron distribution function in the thruster requires a kinetic method (Kalentev *et al.* 2014). Due to the rotational symmetry of the system, the spatial domain was reduced to r–z (radial and axial coordinate) and an electrostatic 2d3v PIC code (2-D in position space and 3-D in velocity space) with Monte Carlo collisions (Matyash *et al.* 2010; Kalentev *et al.* 2014) was used. In this PIC-MCC simulation we follow the kinetics of so-called super-particles (each of them representing many real particles), moving in the self-consistent electric field calculated on a spatial grid by solving Poisson's equation

$$\Delta \Phi = -\frac{\rho}{\varepsilon}. \tag{2.1}$$

Here, Φ indicates the electric potential, ρ the plasma density and ε the absolute permittivity. The relevant collisions: electron–electron Coulomb, electron–neutral elastic, ionisation and excitation collisions, ion–neutral momentum transfer and charge exchange collisions are included. For Coulomb collisions a binary collision routine, as suggested by Takizuka & Abe (1977), is used. Collisions with neutrals are simulated by a Monte Carlo routine similar to Vahedi *et al.* (1993), using cross-sections for xenon from Hayashi (2003), Phelps (2000) and Phelps (2002). A detailed description of the applied collision models can be found in Tskhakaya *et al.* (2007). The dynamics of the background neutral gas is self-consistently resolved by Direct Simulation Monte Carlo (Procassini *et al.* 1987). As can be seen from three-dimensional (3-D) simulations of a similar HEMP thruster model, classical transport along magnetic field lines is dominant (Kalentev *et al.* 2014). Only in the narrow cusp regions, where $\boldsymbol{B}$ turns from the axial to radial direction, fluctuations of the azimuthal electric field allow the electrons to overcome. In the 3-D simulations the anomalous fluxes are calculated self-consistently (Kalentev *et al.* 2014). Using these results, an effective anomalous transport coefficient of $D_{\perp} \propto 0.4 \times k_B T/eB$ following Bohm, Burhop & Massey (1949) can be determined. This coefficient is then used in the 2-D model, which does not allow us to calculate electrostatic turbulence self-consistently. The anomalous transport fluxes are implemented by a diffusive model using the calibrated transport coefficient deduced from the 3-D simulation for a random walk model in velocity space in all three velocity components (radial, axial and poloidal). Information of all three velocity components exists in the 2-D code due to the Monte Carlo collisions (Bronold *et al.* 2007; Tskhakaya *et al.* 2007). The isotropic characteristics of turbulence is well represented by this procedure. Dominant transport contributions in two dimensions will be perpendicular to the magnetic field lines, as discussed previously. With respect to the channel plasma parameters, an equidistant grid with a spacing of $\Delta r = \Delta z = 1.3\,\lambda_{D,e} = 0.01$ mm is used, including both the thruster channel and the near-field plume. In order to reduce the computational time, a similarity scaling is applied with a factor of 10 (Taccogna *et al.* 2005). For the time resolution a time step of $\Delta t = 0.2\,\omega_{p,e}^{-1} = 1$ ps is chosen. In the channel around the propulsion exhaust, the neutral particle density is two orders of magnitude higher than for the plasma particles. For a correct treatment of MCC of neutrals with plasma particles, the same weighting of plasma and neutral super-particles is required. This results in a number of simulated super-particles which is 100 times higher than for ions and electrons. In total, the high resolution in space, time and particles results in a long run time. For the serial PIC-MCC code, typically one month of calculation is needed on a desktop system in order to simulate a run time in the range of some micro seconds. With access to parallel computing clusters, the best chance of gaining a speed up of the simulation is an efficient parallelisation.

Dependent on the simulated system, a domain decomposition according to number of particles in each subdomain is applied; collision probability or grid cells per rank. In this work, a domain decomposition according to number of particles was used. With the help of the Message Passing Interface (MPI), particle arrays as well as the electric field computed on the grid are distributed to the different subdomains. Each subdomain is either located at different nodes or cores. This allows the parallel execution of the particle pusher. In a second step, the MC collisions routine is planned to be parallelised by using the Open Multi-Processing (OpenMP), suitable for shared memory parallelisation on a single node.

To calculate the electric field on the grid, Poisson's equation (2.1) is solved using a finite difference scheme for the spatial second-order derivatives creating a system of linear equations

$$\boldsymbol{A\Phi} = \boldsymbol{b}. \tag{2.2}$$

Here, the vector $\boldsymbol{\Phi}$ and $\boldsymbol{b}$ indicate the electric potential ϕ and the plasma density $-\rho/\varepsilon$ respectively, on the grid points. For a two-dimensional $M \times N$ grid, this gives a matrix $\boldsymbol{A}$ of dimension $(M \cdot N) \times (M \cdot N)$. In order to reach reasonably low computing time, the calculation of $\boldsymbol{\Phi}$ within one time step has to be faster than one second $t_{max} \leqslant 1$ s.

A standard sparse matrix solver is the LU decomposition. The matrix is decomposed into a product of an upper triangular matrix $\boldsymbol{U}$ and a lower triangular matrix $\boldsymbol{L}$. By this, in each time step the calculation of $\boldsymbol{L}(\boldsymbol{U\Phi}) = \boldsymbol{b}$ can be done easily. While the decomposition is rather time consuming, the so-called back solve has a complexity of $\sim(M \cdot N)^2/2$ (Stoer 2005*a*), making it very efficient. Therefore, the decomposition is calculated only at the beginning of the simulation, as the matrix does not change throughout the execution of the code, and only the back solve has to be computed every PIC cycle, hence giving a complexity of $\sim(M \cdot N)^2$ per PIC cycle. A parallelisation of this method is problematic, as each line within a back-solve step depends on the results of the previous lines, limiting its application to one computational core. Parallel methods are only available for the calculation of the LU decomposition but not for the back solve (Li 2005).

In order to reduce the number of grid points, a 'matryoska-like' hierarchy of equidistant grids can be used for the simulation of the HEMP thruster (Kalentev *et al.* 2014). The hierarchy is constructed such that a coarse grid, given by the electron Debye length in the plume, covers the whole domain, while a fine grid with a mesh spacing of $\lambda_{D,e}$ in the channel, covers in addition the channel and the near-field plume. The solution of Poisson's equation (2.1) is obtained by first solving the equation on the coarse grid and then using the interpolated coarse grid values as boundary values for the fine grid solution. This approach appears to be not only accurate enough, but also remarkably fast compared with the solution for a single equidistant mesh. Alternatively, non-equidistant meshes could be used, but these suffer from artefacts (Tskhakaya *et al.* 2007), such as self-forces, and corrections to minimise such errors are needed. A reduction can be achieved by a modified two point central difference scheme for calculation of the electric field on a non-equidistant grid (Duras *et al.* 2014). In the case of thruster simulations, a transition from a fine to a coarser grid can be done in the plume region, since here the coupling with the channel plasma is lower and the influence of artificial forces is reduced.

Instead of using the fast, but serial back solve, the advantage of a slower but parallelisable method can be facilitated (Kahnfeld *et al.* 2016). A standard iterative solver is the successive over-relaxation (SOR) method which is often applied to solve the finite difference discretisation of the Poisson equation (2.1). It is a variation of the Gauss–Seidel algorithm with a relaxation factor $\omega > 1$. The matrix $\boldsymbol{A}$ is represented by the sum of $\boldsymbol{A}$'s diagonal matrix $\boldsymbol{D}$ (with $a_{ii} \neq 0$ for all i) and it's strictly lower and upper triangular matrices $\boldsymbol{L}$ and $\boldsymbol{R}$ (not to be confused with the matrix used in the LU decomposition) with $\boldsymbol{A} = 1/\omega(\boldsymbol{D} + \omega\boldsymbol{L}) + \boldsymbol{R}$. The expected number of iteration steps is $\sim(M \cdot N)$, giving the entire SOR method a complexity of $\sim(M \cdot N)^3$ (Stoer 2005*b*). This is much higher compared to the back solve of the LU decomposition which scales quadratically, however the algorithm allows for easy parallelisation as the calculation of each point's iterate depends only on the surrounding points. Only the boundary points have to be exchanged during each iteration step.

In this work, compared to a serial run, parallelisation of the particle pusher gained a speed up of 2.6, running on 2 nodes with 4 cores each node. Here, mainly the serial solver limits the total simulation speed up.

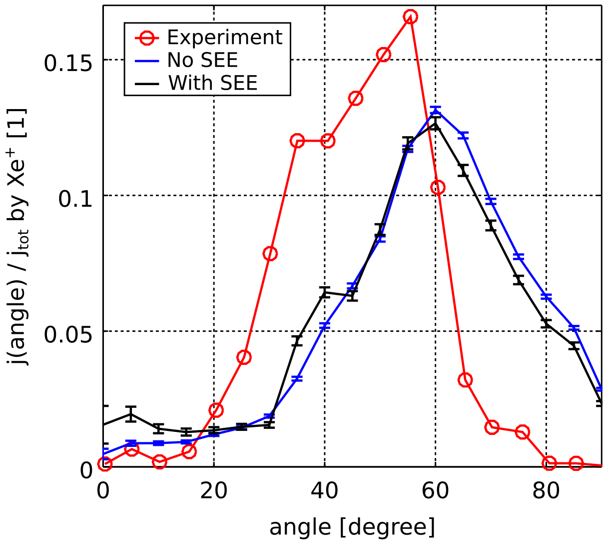

FIGURE 1. Angular ion current distribution with respect to the thruster exit at $r = 0$ mm, measured in experiment (Matyash *et al.* 2009) and simulated with SEE and without. Simulation results are given with statistic error bars.

3. Ion angular distributions

The angular distributions of ion current and energy are among the key parameters of an ion thruster and are also directly accessible to experiments. Within experiments, ion angular distributions are typically measured with a Retarding Potential Analyzer (RPA) at approximately 1 m distance from the thruster exit (van Reijen *et al.* 2013). In the PIC simulation, the simulated plume has a size of several centimetres, limited by the high computational costs. In the plume, the potential distribution and ion–neutral collisions are the important physical mechanisms for current and energy distribution of the ions. Also, secondary electron emission (SEE) at vessel walls, generated by accelerated ions, influences the potential at the thruster exit. These low energetic electrons are magnetised in the thruster near-field plume and follow the magnetic field lines.

In the following the angular ion current distribution, as well as the angular energy distribution, will be discussed in detail. Within the simulation, these distribution functions are diagnosed along a diagnostic surface at the plume domain boundary. The angle is defined with respect to the thruster exit at the symmetry axis ($r = 0$ mm), assuming a point source. In experimental measurements the same assumption is applied. The angular resolution is chosen to be 5°. For the current diagnostics, the current passing the diagnostic surface is calculated and for the energy distribution, the kinetic energy of the ions crossing this surface is detected.

3.1. *Angular ion current distribution*

In figure 1, the calculated angular ion current distribution is given in blue. It shows contributions for all angles with a maximum current at 60°. In the same figure a measured angular ion current distribution for the DM3a HEMP model is given in red. It shows two maximums at 35° and 55°, respectively. For a better understanding, the origin of the detected ions was diagnosed and analysed with respect to the angle. It indicates a correlation of the respective cusp, in which an ion is generated, and the

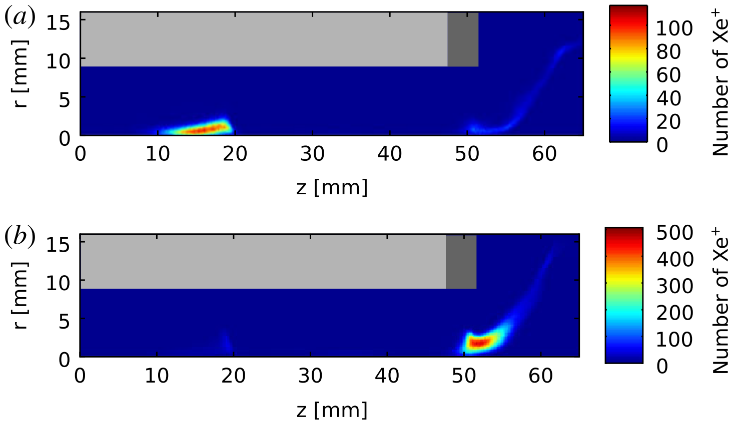

FIGURE 2. Ionisation distribution for ions detected at the diagnostic surface at 40 ± 2.5° (*a*) and 60 ± 2.5° (*b*). The dielectric channel wall is shown in light grey and the grounded pole piece is shown in dark grey.

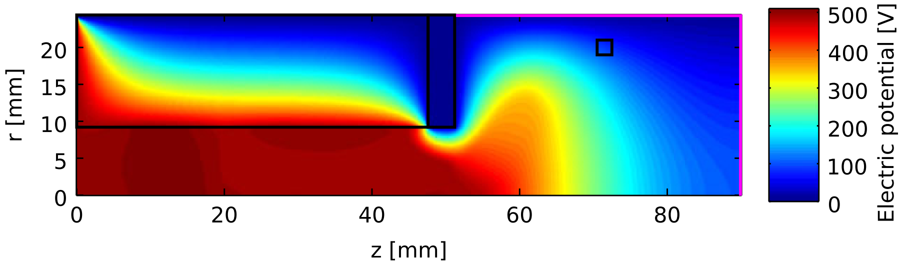

FIGURE 3. Potential of thruster channel and plume, given in V. In magenta, the diagnostic surface for the ion angular distributions is given at the plume domain boundary. The small black box in the plume indicates the position of the electron source.

angle into which it is emitted, as can be seen in figure 2, which shows the ionisation distribution for ions detected at 40° and 60°. While for angles between 30° and 50°, ions are mainly generated in the central cusp, for angles larger than 55° the exit cusp apparently is the place of origin. Due to a low contribution of the ionisation in the central cusp, the second maximum around 40° is not well accentuated. Therefore, the simulated ion angular current distribution can be seen as qualitatively matching the experimental data, shifted by 5° towards higher angles.

An important effect on the angular ion distribution is the potential drop in the plume, accelerating the ions towards different angles. In the simulation, it is also sensitive to the potential at the boundary of the simulation domain due to its limited size. In figure 3, the resulting potential is shown and in magenta, the diagnostic surface is indicated. The black rectangle at $r = 20$ mm and $z = 75$ mm indicates the position of the primary electron source with a source current of $I_{src,1} = 0.3$ mA. It represents the real neutraliser, which is located outside the computational domain. The position was chosen in order to provide sufficient starter electrons for the thruster channel. In experiments, the HEMP-T can operate even without the neutraliser because even a very small amount of free electrons are sufficient for successful start up. Corresponding ion and electrons distributions can be found in Duras *et al.* (2016). For the boundary condition at the right-hand side of the domain $E_z = 0$ is chosen. The potential at the left-hand side is fixed to the anode potential U_a. At the upper boundary $\Phi = 0$ V is used. This fixed potential can squeeze or stretch the potential solution in the radial direction, which results in shifted angular distributions. To prevent this, it is reasonable to use, for the area of the simulated plume, a similar aspect ratio as the vessel in which the experiments were taking place. What constitutes a sufficient domain size to reduce the influence of this defined potential boundary remains to be investigated.

An indirect influence on the potential is induced by the emission of secondary electrons from the vessel walls. These low energetic electrons are attracted by the anode potential and become magnetised by the magnetic field of the thruster acting as additional primary source of electrons. A study of different external electron sources and their positions showed strong influence of the magnetic field on the near-field plume (Duras *et al.* 2016). To represent the possible contributions of secondary electrons created by ions at the vessel walls, an electron source is placed close to the symmetry axis. This changes the potential distribution in the channel, while external electron sources at other places in the plume hardly influence the potential structure. The main reason for this is that the magnetic field, close to the symmetry axis, points directly into the thruster. At other radial positions the field lines are curved and electrons are trapped between a magnetic mirror movement, pushing them away from the thruster, and the potential drop forcing them towards the exit. Electrons emitted close to the symmetry axis have higher energies due to the direct guidance into the channel. This increases the probability of ionisation which expands the potential drop out of the thruster channel.

SEE at the aluminium vessel walls can act as an additional electron source. Secondary electrons created at the vessel walls by impinging ions fly towards the thruster. Rosenberg & Wehner (1962) measured sputter yields for singly charged ions impinging on aluminium which have been published for ion energies of 100, 200, 300 and 600 eV. With the help of an empirical fitting formula by Yamamura, Matsunami & Itoh (1983), an emission coefficient of $\gamma = 0.6$ can be approximated for singly charged xenon ions impinging with an energy of 500 eV.

Approaching the thruster entrance such electrons experience an increasing magnetic field, which directs them mostly towards the axis. In the small simulation domain of this work, the electron influx from this process is parametrised as an additional surface source close to the axis. Electrons are injected at the right domain boundary close to the symmetry axis at $r \in (0; 2\ \text{mm})$ and $z \in (88\ \text{mm}; 90\ \text{mm})$, with a directed drift velocity towards the thruster based on an energy of 100 eV corresponding to the potential at this location and a thermal broadening of the source distribution assuming a temperature of 0.45 eV. Of the total emitted ion current of $I_{tot} = 142$ mA, 10 % were chosen as an effective electron source close to the axis, representing SEE. This contribution is a factor of approximately 5 times higher than the primary electron source. This value was chosen because it induced a visible effect in the solution without affecting strongly the integral ion current.

The resulting angular current distribution with SEE can be seen in black in figure 1. It shows a higher ion contribution close to the symmetry axis (0°), which is the direct effect of the additional electron source in this region. At approximately 40° the second ion beam becomes more pronounced, which is in qualitative agreement with the experimental data.

3.2. *Angular ion energy distribution*

The simulated angular ion energy distribution calculated at the domain boundary is shown in figure 4. At the left-hand side the calculated ion flux is colour coded in

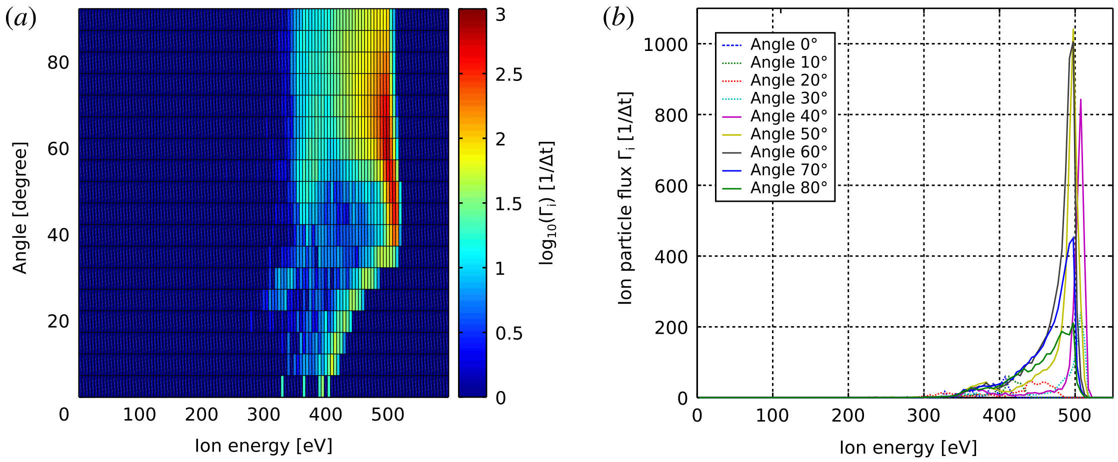

FIGURE 4. Angular ion energy distribution at the domain boundary. (*a*) Contour plot of the ion particle flux Γ_i in logarithmic scale as a function of angle and ion energy. (*b*) Γ_i in linear scale as a function of ion energy shown for nine angles.

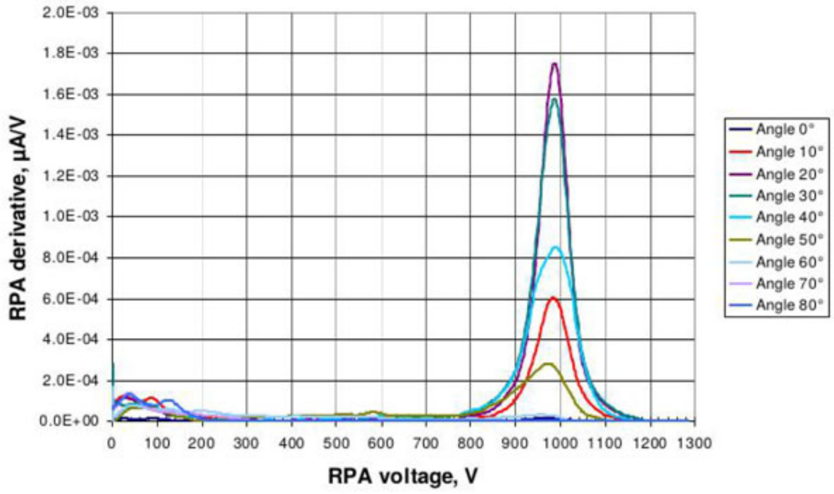

FIGURE 5. Angular ion energy distribution for the HEMP thruster model HEMPT 3050, derived from RPA measurements. The applied thruster anode voltage was $U_a = 1000$ V (Koch *et al.* 2011).

logarithmic scale and the angle is defined with respect to the thruster exit at the symmetry axis. The right-hand side of figure 4 shows the same result in linear scale as line plots for nine angles. As expected, the maximum ion energy is 500 eV, given by the anode potential. The dominant contribution of ions originates from ions at approximately 60°.

An experimentally measured energy distribution for the HEMP thruster model HEMPT 3050 is shown in figure 5 for nine different angles (Koch *et al.* 2011). It is characterised by a maximum close to the anode potential $U_a = 1000$ V, with an opening angle of 20°. While the simulated energy distribution shows a peak, smeared out to lower energies, the measured data show a Gaussian distribution around U_a.

In the numerical diagnostic, the limited domain size causes differences between the simulated and measured ion energy distributions. In order to make the simulated ion distribution comparable to the experimentally measured one, a transfer function $g(f)$,

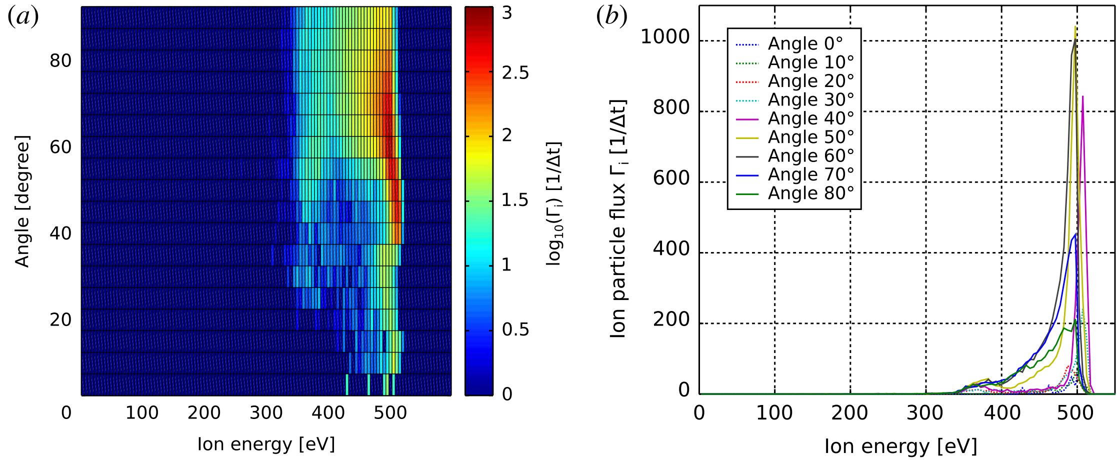

FIGURE 6. Mapped angular ion energy distribution to the location of the experimental detector position. (*a*) Contour plot of the ion particle flux Γ_i in logarithmic scale as a function of angle and ion energy. (*b*) Γ_i in linear scale as a function of ion energy shown for nine angles.

similar to the detector function in Reiter (2009), is used to transfer information from the domain boundary to the detector position in the experiment

$$g : f(\text{domain boundary}) \mapsto f(\text{detector position}). \tag{3.1}$$

Here f stands for the angular ion energy distribution. This correction is used to represent effects which are not included in the current PIC simulation. One artefact caused by the limited domain size originates from the von Neumann boundary condition at the right-hand side of the domain. Ions reaching the diagnostic surface at this location have not yet reached the maximum kinetic energy of U_a. For small angles, 0°–30°, one can clearly see in figure 4 a reduction of the maximum energy, which is decreasing with the angle. At the detector position 1 m distant from the thruster exit, the potential will have relaxed to values close to ground potential and the additional acceleration by this potential drop has to be taken into account. Therefore, the transfer function $g(f)$ of the angular ion energy distribution corrects the ion energies of the detected ions by adding the additional potential at the domain boundary

$$f(\text{detector position}) = f(\text{domain boundary}) + q_i \varPhi(\text{domain boundary}), \tag{3.2}$$

with the ion charge q_i. In figure 6, the corrected angular ion energy distribution can be seen. For angles $<35°$, the correction results in a shift to higher energies, so that for all angular bins the maximum energy corresponds to the anode potential U_a. This improves the qualitative agreement between simulation and measured ion energy distribution (see figure 5).

Another discrepancy between experiment and simulation are the missing ion charge exchange (CX) collisions during the 1 m of flight within the plume. Within the PIC simulation, domain charge exchange collisions between ions and neutrals are fully included. While within the acceleration channel the mean free path of these collisions is smaller than the channel length, the decreasing neutral density increases this mean free path to approximately 1 m, which is larger than the simulated domain size. Therefore, CX collisions appearing between the domain boundary of the simulation and the position of the experimental measurement of the ion energy distribution are not represented within this simulation due to the latter's limited domain size and require special corrections. This is visible in the missing low energetic part of the ion energy distribution of the simulation (figure 4), which clearly appear in the experimental measurements at about 0–200 eV (figure 5). Here the idea of the transfer function, trying to map the information from the boundary of the simulated domain to the location of the experimental measurement, can be improved using a Monte Carlo post-processing procedure including CX collisions for a pre-defined neutral background gas density in the vessel.

4. Conclusions

Although angular ion distributions are important parameters in experiments and the validation of ion thruster simulations, measurements and simulations are difficult to compare. Especially for PIC simulations, the measurement distance of these distributions is much larger than the possible domain size. Therefore, a parallelisation strategy is necessary in order to increase the domain size. With a parallel particle pusher, using a particle weighted domain decomposition, a speed up of a factor 2.6 was achieved for 2 nodes with 4 cores, compared to a serial simulation.

Ion angular distributions are sensitive to the plume potential. Secondary electron emission at vessel walls due to impinging fast ions can modify the potential structure in the near-field region of the plume and by this the ion angular distributions. As shown in previous studies (Duras *et al.* 2016), only near-axis electron sources are able to change the plume potential. In addition the magnetic field of the thruster guides most of the emitted secondary electrons towards the channel axis. Therefore a near-axis surface source was implemented at the domain boundary, which affects only the small angles in the ion angular current distribution as expected.

The small domain size leads to artefacts at the domain boundary, because the potential does not drop to zero within this domain size. The concept of a transfer function was introduced to map the simulated ion angular distribution from the computational boundary to the location of the experimental measurement at approximately 1 m. For this, the potential energies of the ions were corrected, shifting them by the potential at the domain boundary. This improves the qualitative agreement between simulation and measured ion energy distribution. In the future, a further improvement of the transfer function is possible including the effect of charge exchange collisions in the plume plasma by a Monte Carlo module, following the ions from the domain boundary to the location of the detector.

Acknowledgements

This work was supported by the Bavarian State Ministry of Education Science and the Arts and the German Space Agency DLR. We also like to thank R. Heidemann from THALES Electron Devices GmbH for interesting and stimulating discussions.

REFERENCES

BOHM, D., BURHOP, E. H. S. & MASSEY, H. S. W. 1949 *The Characteristics of Electrical Discharges in Magnetic Fields*. McGraw-Hill.

BRONOLD, F. X., MATYASH, K., TSKHAKAYA, D., SCHNEIDER, R. & FEHSKE, H. 2007 Radio-frequency discharges in oxygen: I. particle-based modelling. *J. Phys.* D*: Appl. Phys.* **40** (21), 6583–6592.

DURAS, J., MATYASH, K., TSKHAKAYA, D., KALENTEV, O. & SCHNEIDER, R. 2014 Self-force in 1d electrostatic particle-in-cell codes for non-equidistant grids. *Contrib. Plasma Phys.* **54** (8), 697–711.

DURAS, J., SCHNEIDER, R., KALENTEV, O., KEMNITZ, K., MATYASH, K., KOCH, N., LÜSKOW, K., KAHNFELD, D. & BANDELOW, G. 2016 Influence of electron sources in the near-field plume in a multistage plasma thruster. *Plasma Physics and Technology* **3** (3), 126–130.

HAYASHI, M. 2003 Bibliography of electron and photon cross sections with atoms and molecules published in the 20th Century – Argon –. *Res. Rep. NIFS-Data Series*, NIFS-DATA-072.

KAHNFELD, D., BANDELOW, G., DURAS, J., LÜSKOW, K., KEMNITZ, K. & SCHNEIDER, R. 2016 Solution of poisson's equation in electrostatic particle-in-cell simulations. *Acta Polytech*; (submitted).

KALENTEV, O., MATYASH, K., DURAS, J., LÜSKOW, K. L., SCHNEIDER, R., KOCH, N. & SCHIRRA, M. 2014 Electrostatic ion thrusters – towards predictive modeling. *Contrib. Plasma Phys.* **54**, 235–248.

KOCH, N., HARMANN, H.-P. & KORNFELD, G. 2007 Status of the THALES high efficiency multi stage plasma thruster development for HEMP-T 3050 and HEMP-T 30250. In *Proceedings of the 30th International Electric Propulsion Conference,* vol. IEPC-2007-110. Electric Rocket Propulsion Society.

KOCH, N., SCHIRRA, M., WEIS, S., LAZURENKO, A., VAN REIJEN, B., HADERSPECK, J., GENOVESE, A., HOLTMANN, H.-P., SCHNEIDER, R., MATYASH, K. *et al.* 2011 The hempt concept – a survey on theoretical considerations and experimental evidences. In *Proceedings of the 32nd International Electric Propulsion Conference,* vol. IEPC-2011-236. Electric Rocket Propulsion Society.

KORNFELD, G., KOCH, N. & HARMANN, H.-P. 2007 Physics and evolution of HEMP-Thrusters. In *Proceedings of the 30th International Electric Propulsion Conference,* vol. IEPC-2007-108. Electric Rocket Propulsion Society.

KORNFELD, G., SEIDEL, H. & WEGENER, J. 1998 Plasma accelerator arrangement. *Patent* PCT/DE99/01708.

LI, X. S. 2005 An overview of superlu: Algorithms, implementation, and user in- terface. *ACM Trans. Math. Softw.* **31**, 302–325.

MATYASH, K., KALENTEV, O., SCHNEIDER, R., TACCOGNA, F., KOCH, N. & SCHIRRA, M. 2009 Kinetic Simulation of the stationary HEMP thruster including the near-filed plume region. In *Proceedings of the 31st International Electric Propulsion Conference,* vol. IEPC-2009-110. Electric Rocket Propulsion Society.

MATYASH, K., SCHNEIDER, R., MUTZKE, A., KALENTEV, O., TACCOGNA, F., KOCH, N. & SCHIRRA, M. 2010 Kinetic simulations of SPT and HEMP thrusters including the near-field plume region. *IEEE Trans. Plasma Sci.* **38** (9, Part 1), 2274–2280.

PHELPS, A. V. 2000 Nitrogen atoms and molecules. Retreved from http://jila.colorado.edu/avp/collision_data/neutralneutral/atomatom.txt (January 2015).

PHELPS, A. V. 2002 Nitrogen atomic and molecular ions. Retreved from http://jila.colorado.edu/avp/collision_data/ionneutral/IONATOM.TXT (January 2015).

PROCASSINI, R., BIRDSALL, C., MORESE, E. & COHEN, B. 1987 A relativistic monte carlo binary collision model for use in plasma particle simulation codes. *Mem. No.* UCB/ERL M87/24, University of California, Berkeley.

VAN REIJEN, B., WEIS, S., LAZURENKO, A., HADERSPECK, J., GENOVESE, A., HOLTMANN, P., RUF, K. & PTTMANN, N. 2013 High precision thrust vector determination through full hemispherical rpa measurements assisted by anguar mapping of energy charge state distribution. In *Proceedings of the 33nd International Electric Propulsion Conference,* vol. IEPC-2013-284. Electric Rocket Propulsion Society.

REITER, D. 2009 The EIRENE code user manual. Retreved from http://www.eirene.de (September 2016).

ROSENBERG, D. & WEHNER, G. K. 1962 Sputtering yields for low energy He+-, Kr+-, and Xe+-Ion Bombardment. *J. Appl. Phys.* **33** (5), 1842–1845.

STOER, J. 2005*a* *Numerische Mathematik*, vol. 1. Springer.

STOER, J. 2005*b* *Numerische Mathematik*, vol. 2. Springer.

TACCOGNA, F., LONGO, S., CAPITELLI, M. & SCHNEIDER, R. 2005 Self-similarity in hall plasma discharges: Applications to particle models. *Phys. Plasmas* **12**, 053502.

TAKIZUKA, T. & ABE, H. 1977 A binary collision model for plasma simulation with a particle code. *J. Comput. Phys.* **25**, 205–219.

TSKHAKAYA, D., MATYASH, K., SCHNEIDER, R. & TACCOGNA, F. 2007 The particle-in-cell method. *Contrib. Plasma Phys.* **47** (8–9), 563–594.

VAHEDI, V., DIPESO, G., BIRDSALL, C. K., LIEBERMAN, M. A. & ROGNLIEN, T. D. 1993 Capacitive RF discharges modelled by particle-in-cell Monte Carlo simulation. I. Analysis of numerical techniques. *Plasma Sources Sci. Technol.* **2** (4), 261.

YAMAMURA, Y., MATSUNAMI, N. & ITOH, N. 1983 Theoretical studies on an empirical formular for spittering yiels at normal incidence. *Radiation Effects* **71**, 65–86.

Contrib. Plasma Phys. **46**, No. 0, 1 – 15 (2007) / **DOI** 10.1002/theDOIsuffix

Electrostatic Ion Thrusters - Towards Predictive Modeling

O. Kalentev[1,*], **K. Matyash**[1,**], **J. Duras**[1,***], **K. F. Lüskow**[1,†], **R. Schneider**[1,‡], **N. Koch**[2,§], **M. Schirra**[3,¶], and **B. van Reijen**[3,‖]

[1] Ernst-Moritz-Arndt Universität Greifswald, D-17489, Germany
[2] Technische Hochschule Nürnberg Georg Simon Ohm, Keßlerplatz 12, D-90489 Nürnberg, Germany
[3] Thales Electronic Systems GmbH, Söflinger Straße 100, D-89077 Ulm, Germany

Received XXXX, revised XXXX, accepted XXXX

Key words PIC simulation, High Efficiency Multistage Plasma Thruster, Integrated Modeling.

The development of electrostatic ion thrusters so far has mainly been based on empirical and qualitative know-how, and on evolutionary iteration steps. This resulted in considerable effort regarding prototype design, construction and testing and therefore in significant development and qualification costs and high time demands. For future developments it is anticipated to implement simulation tools which allow for quantitative prediction of ion thruster performance, long-term behavior and space craft interaction prior to hardware design and construction. Based on integrated numerical models combining self-consistent kinetic plasma models with plasma-wall interaction modules a new quality in the description of electrostatic thrusters can be reached. These open the perspective for predictive modeling in this field. This paper reviews the application of a set of predictive numerical modeling tools on an ion thruster model of the HEMP-T (High Efficiency Multistage Plasma Thruster) type patented by Thales Electron Devices GmbH.

1 Introduction

Ion thrusters, where the propellant is ionized and the ions are accelerated by electric fields, are of increasing importance for scientific and commercial space missions. Compared to the commonly used chemical thrusters they have a 5 to 10 times higher specific impulse [1]. This results in a considerable reduced propellant budget such that a significant reduction of spacecraft launch mass by some 100 to $1000 kg$ can be achieved.

The most straightforward concept of an electric propulsion system is the grid thruster. Here, gaseous propellant is ionized in a low pressure, low temperature gas discharge sustained by DC, radio-frequency or microwave fields, respectively. A biased grid at the thruster exit accelerates and extracts the produced ions. Since ionization and acceleration occurs independent of each other, it is possible to optimize these two processes separately. This yields a high efficiency of the device but also a huge system complexity. Therefore ion propulsion systems based on grid thrusters tend to be expensive and to exhibit reliability issues [2].

An alternative are grid-less ion thrusters which are based on magnetic confinement of the plasma electrons, where the trapped electrons both ionize the propellant and provide the potential drop for ion acceleration. Due to their low complexity in therms of system architecture they are becoming of increasing interest in particular for commercial satellites. In order to achieve reduced development and qualification effort, it is therefore needed to set up and apply a series of different modeling tools which can quantitatively describe the plasma physics within the thruster but also interactions of the thruster with the testing environment and finally the satellite. The integrated modeling strategy should include several modular components in a consistent way in order to provide

---

[*] Corresponding author E-mail: kalentevo@uni-greifswald.de, Phone: +49 (0)38 348 61447, Fax: +49 (0)38 348 614 01
[**] E-mail: knm@ipp.mpg.de
[***] E-mail: durasj@uni-greifswald.de
[†] E-mail: kl081737@uni-greifswald.de
[‡] E-mail: schneider@uni-greifswald.de
[§] E-mail: Norbert.Koch@th-nuernberg.de
[¶] E-mail: Martin.Schirra@thalesgroup.com
[‖] E-mail: Benjamin.Reijen@thalesgroup.com

the necessary complexity and accuracy depending on the problem. As an example, results for the grid-less High Efficient Multistage Plasma Thruster (HEMP-T) model DM3a are presented. The outline of the paper is the following: after a general introduction of the HEMP-T the general strategy for predictive modeling is presented. The characteristics of HEMP-T as deduced from 2D Particle-in-Cell (PIC) calculations are reviewed. A first example of 3D PIC results for self-consistent modeling of electrostatic turbulence in a HEMP-like geometry is given. Strategies and results for the simulation of the interaction of the thruster with the satellite in the plume and results on erosions are discussed afterwards, before the paper is summarized in the conclusions.

2 The High Efficient Multistage Plasma Thruster (HEMP-T)

An ion thruster design which has the advantage of an electric field topology similar to grid thrusters at significant reduced thruster complexity is the High Efficient Multistage Plasma Thruster (HEMP), patented by the THALES group in 1998 [3]. As described in [1], HEMP-T's consist of a dielectric, rotationally symmetric discharge channel at the upstream end of which an anode is located. The anode is connected to the power supply and represents the only high voltage electrode in the thruster; it also serves as inlet for the propellant. The discharge channel is surrounded by a system of axially magnetized permanent magnet rings in opposite magnetization, the so-called PPM system. At the downstream end of the discharge channel, the thruster exit, a hollow cathode neutralizer is placed to provide the starter electrons for igniting the discharge and for neutralizing the ion beam emitted by the thruster. A schematic picture of the HEMP-T concept as described above is given in Fig. 1. The PPM system forms a linear magnetic multi-cusp structure inside the discharge channel. The magnetic field periodically changes between predominant axial and predominant radial direction. The level of magnetic induction B at any position within the thruster channel is chosen such that the Larmor radius of the electrons is much smaller than the geometrical dimensions of the discharge channel, whilst the propellant ions are hardly affected by the magnetic field due to their much higher mass. The gradients fulfill $\frac{dB_z}{dz} > 0$ in the axial zones and $\frac{dB_r}{dr} > 0$ in the radial zones, where in addition a strong gradient $\frac{dB_r}{dz}$ is build up. In this way the plasma electrons are efficiently confined along the entire discharge channel and only few electrons are lost to the wall mostly at the cusps. Electron confinement due to cusp mirror oscillations is dominant compared to the Hall current which builds up due to the $E \times B$ drift.

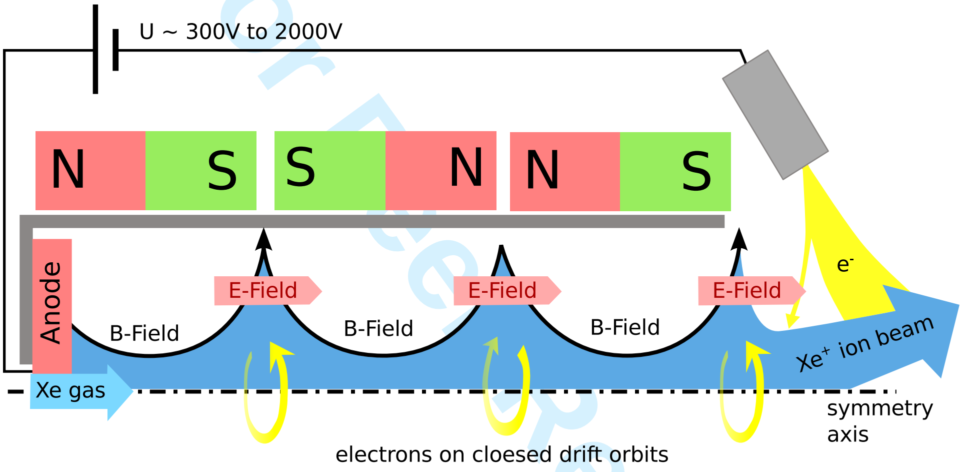

Fig. 1 Schematic view of the High Efficient Multistage Plasma Thruster (HEMP).

In this work an older prototype model named DM3a is discussed. It has implemented two cusps, the anode and the exit cusp and is described in [4]. In the HEMP thruster the ionization is particularly strong at the cusps regions. Due to the strongly reduced plasma wall contact in the cusp regions and mean energy of impinging ions at these locations below the sputter threshold, HEMP is characterized by a long lifetime of at least $10.000h$ [5].

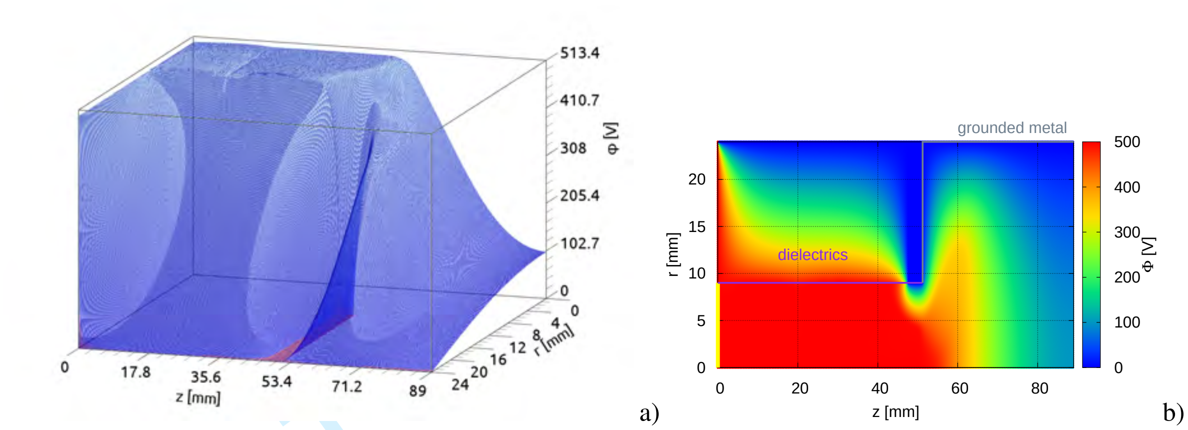

Fig. 2 Potential of the HEMP DM3a thruster with a channel radius of $R = 9mm$ and $L = 51$ length. The anode volatege is set to $500V$. Plotted as a **a)** 3D plot and as a **b)** potential profile.

Potential, densities and plasma species temperatures of the DM3a were calculated with an electrostatic 2d3v Particle in Cell code with Monte Carlo collisions (PIC MCC) [6]. PIC MCC is a simulation method, used for low temperature plasmas [7], [8]. It gives a fully self-consistent microscopic description of a plasma and is able to involve complicated atomic and plasma-surface interactions. In the PIC-MCC simulation we follow the kinetics of so-called Super Particles (each of them representing many real particles), moving in the self consistent electric field calculated on a spatial grid from the Poisson equation. The particle collisions are handled by Monte-Carlo collision (MCC) routines, which randomly change particle velocities according to the actual collision dynamics. All relevant collisional processes are included in the model: electron-neutral elastic, ionization and excitation collisions, ion neutral momentum-transfer and charge exchange collisions. The dynamics of the background neutral gas is self-consistently resolved with direct simulation Monte Carlo. For a reliable plasma simulation, effects on the smallest length scales in a plasma, the Debye-scale $\lambda_{D,e}$ have to be resolved. Therefore, the smallest lateral grid size is $\Delta x = 0.5\lambda_{D,e}$. The simulation has to resolve the fastest process in the system - the electron Langmuir oscillations. Therefore, the time step in the simulation is chosen $dt = 0.2/\omega_{pe}$, where ω_{pe} is the electron plasma frequency. A more detailed description of PIC can be found in [8]. An important ingredient for speeding up the 2D PIC calculations is the use of a similarity scaling [6]. A typical value of the scaling factor is 0.1. Scaling is particularly well applicable for the HEMP-T concept because of the negligible wall effects due to the efficient magnetic plasma confinement.

In Fig. 2 the potential as calculated with an electrostatic 2D PIC code is shown. For the HEMP thruster the potential in the plasma bulk is nearly constant with a steep drop at the thruster exit producing a narrow peak in the ion energy spectrum a high specific impulse. Close to the axis, the mainly axial magnetic field allows the electrons to flow along the electric field. A small perturbation of the electric potential is therefore quickly compensated by fast electrons. The inner surface of the channel walls are made of Boron Nitride based ceramics. Near the thruster walls, the potential is decreasing forming the electrostatic sheath. The maximum potential drops are located at the cusps, where magnetic field is perpendicular to the wall.

The influence of the plasma sheath can also be seen in the electron density in Fig. 3. The electron density is uniformly decreasing towards the channel walls and the cusp regions are clearly visible. The higher electron density in these regions due to electrons confined at the radial magnetic field at cusps can be seen. The transfer of energy from directed into thermal motion heats the electrons [9]. Thus, the density of the electrons in the cusp regions is high and the ionization can take place efficiently. For the HEMP thruster the electron source provides the primary electrons, which defines the operational point for the thruster due to the very strong amplification of it by ionization inside the thruster. The direct connection of anode and exit region close to the axis allows ignition of the thruster even without external source by some free electrons. These electrons can be created e.g. by cosmic radiation and will be accelerated to anode potential starting the ionization avalanche [10]. To characterize the basic physics of HEMP-T the velocity distribution functions resolved spatially along the thruster

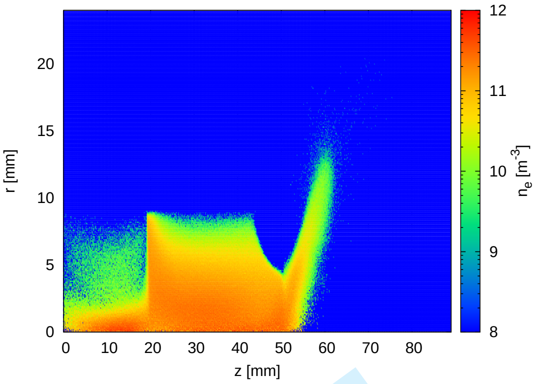

Fig. 3 Electron density profile of the HEMP DM3a thruster.

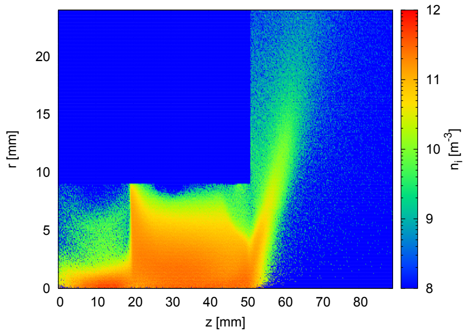

Fig. 4 Ion density profile of the HEMP DM3a thruster.

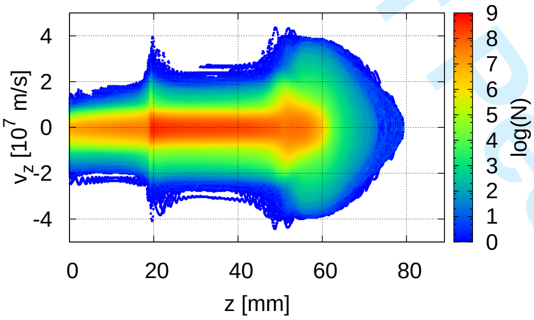

Fig. 5 Electron axial velocity distribution function for $r < R_{thruster}$ as a function of the axial position z

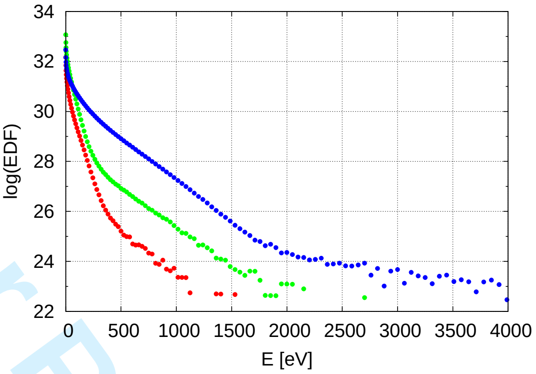

Fig. 6 Electron energy distribution function at different axial positions $10\,mm$ (red), $35\,mm$ (green) and $51\,mm$ (blue)

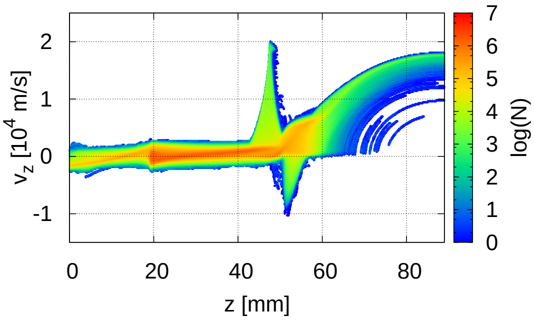

Fig. 7 Ion axial velocity distribution function with $r < R_{thruster}$ as a function of the axial position z

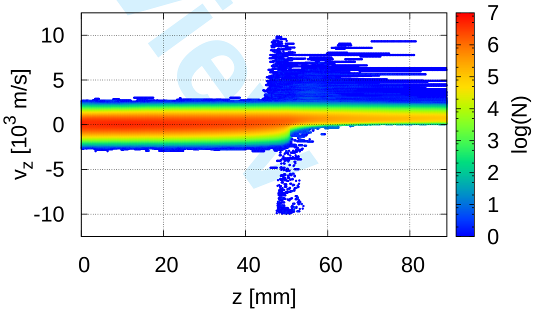

Fig. 8 Distribution of velocity in axial direction for neutrals for $r < R_{thruster}$

axis and averaged in radial direction were calculated. All velocity distribution functions (Fig. 5, 7 and 8) are temporally averaged over 10^6 time steps of a quasi steady-state run. In Fig. 5 the axial velocity distribution function of electrons is plotted. Electron energy distribution functions at different locations are shown in Fig. 6. The distribution functions in the channel are non-Maxwellian, because the mean free paths for electron Coulomb collisions is much longer than the electron path in the system. The axial velocity distribution function shows that the electron axial energy is much higher in the regions about $z = 20\,mm$ and $z = 51\,mm$, since electrons are heated at the cusps. Outside the cusps the velocity distributions are nearly identical within the channel.

The ion density profile is and the corresponding distribution function of the axial velocity are shown in Fig. 4 and 7. Within the channel all ions have rather low velocities due to the nearly constant potential profile. Only at the exit they are accelerated by the strong potential drop. Near the exit cusp and in the plume ions with high energies are existing. The first peak in the distribution at $z = 48\,mm$ with velocities up to $20000\,m/s$ can be explained by the grounded wall after the dielectrics. The right side of the potential structure at this position is very steep and creates a region with large positive velocities. The boundary of this structure is a direct consequence of the potential structure in this region as shown in Fig. 2, because after the grounded wall the potential rises again and ions are slowed down by the counter-acting electric field. Close to the exit cusp inside the channel there are many ions with low velocities. At the exit cusp and afterwards they are accelerated, seen by the shift of the orange color to higher velocities. This acceleration is a consequence of the steep potential drop at the exit. In this acceleration region the ion density decreases. Most of them escape from the region due to their high velocity in radial direction. Further ions are accelerated until the grounded end of the computational domain, due to the continuous drop of the potential. Some of them reach a velocity of about $18000\,m/s$. This explains the trend to higher velocities in Fig. 7 beginning at the exit cusp at $51\,mm$ up to the end of the domain. This structure looks like a quarter of a circle in the velocity distribution function. This is close to a motion with constant acceleration, where the velocity is proportional to the square-root of the distance. Ions are also scattered into the side part of the plume by charge-exchange collisions, where so-called wings can build up.

In Fig. 8 the axial velocity distribution function for neutrals is presented. One can see that charge exchange collisions have an impact on the velocity profile of neutrals. They couple the neutrals to the ions and are responsible for similarities in both distribution functions. Apart from the high-velocity wings the distribution looks quite more regular, since the neutrals are not affected by the magnetic or electric field. Most of the neutrals in the channel have velocities in the range of $-2000\,m/s \ldots 2000\,m/s$, equally distributed in positive and in negative direction. This is again a result of the large neutral density there and their relative low temperature. In the plume the situation for neutrals is different. Neutrals are only flying out of the thruster and negative velocities are not detected.

3 Modeling strategy

The most complete model resolving all time scales would be a direct coupling of a kinetic plasma model with a molecular dynamics model for the walls. This would allow a fully self-consistent analysis of the complete system including plasma dynamics, possible erosion of thruster walls and interaction of the exhausted ions with surrounding satellite surfaces or, during test and qualification, with the testing environment, like the vacuum chamber walls, respectively. Such a solution is not possible due to the tremendous computational costs and high complexity of this combined model. Instead, we propose to use a hierarchical multi-scale set of models in which the parametrization for a lower hierarchy model can be deduced from a higher one (see Fig. 9). For example, a 3D particle-in-cell (PIC) model can deliver a parametrization of turbulence effects by appropriate anomalous transport coefficients. A first proof-of-principle example of a 3D PIC code with a simplified geometry will be presented in section 4. Transport coefficients based on such runs could then be used in a 2D PIC, which is more practical for production runs.

Furthermore, separating the analysis of the thruster from the plume is not adequate, because there exist a strong coupling between thruster and plume plasma. Due to strongly non-Maxwellian characteristics of the distribution functions of both electrons and ions it is not possible to keep any of them in a fluid representation. To get a correct description of both thruster and plume plasma one has to solve a kinetic problem for the whole region of interest including all significant physical processes. These are collisions, turbulence effects, surface driven sheath instabilities and breathing modes. That is why the choice of a PIC model is a natural one for such a problem. In addition, a similarity scaling is applied to further reduce the calculational costs [6].

However, despite the scaling, it is not possible to have a uniform grid for the whole region (thruster and plume) due to extremely different plasma conditions and also physical dimensions of both parts. Therefore, using an equidistant grid will lead to unacceptable grid sizes in terms of computational costs. A possible strategy for the plasma model is a 2D PIC model with a hierarchical grid (see section 5).

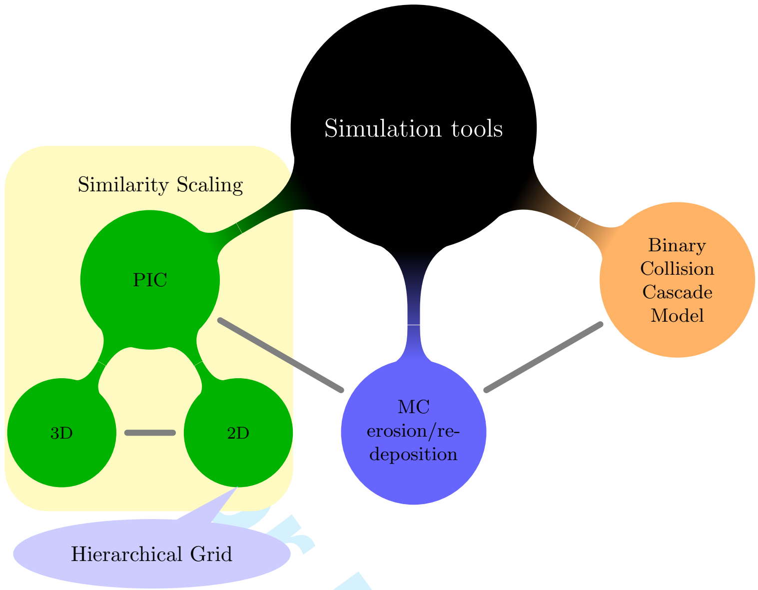

Fig. 9 The concept of a multi-scale modeling for combined thruster-plume models

In order to describe erosion-redeposition processes one can use different approximation levels of the model. The most thorough description is given by the full molecular dynamic model, which would be far too time-consuming because it resolves all individual atoms and their interactions. Next level can be represented by the binary collision cascade model assuming an amorphous target and the interaction of particles with the solid based on heavy particle collisions with ions and additional losses with electrons acting as viscous force. Such a model can use the detailed information about flux distributions provided by the PIC code and calculate then based on this the erosion response of the materials. The most crude approximation is given by a Monte-Carlo (MC) procedure simulating erosion-redeposition based on sputter yield tables calculated from the binary-collision cascade or molecular dynamics model together with the information about plasma fluxes. This model is particular useful due to its simplicity and flexibility allowing to quantify the life time of ion thrusters (see section 6).

4 Anomalous diffusion of electrons

In Hall effect thrusters a radial magnetic field is applied to confine the electrons in the thruster channel and to create the accelerating potential for the ions. The axial electron current towards the anode is possible only because of presence of some diffusion process. There are two major diffusion processes responsible for the electron current across the magnetic field. Classical diffusion due to collisions with neutrals and anomalous diffusion due to azimuthal fluctuations of the electric field.

In classical diffusion, the diffusion coefficient D is proportional to the square of the mean free path λ_{mfp} and one over the average time τ between two collisions

$$D \quad \propto \quad \frac{\lambda^2_{mfp}}{\tau} \quad . \tag{1}$$

Due to the gyration of the electrons, the mean free path in a plasma with an external magnetic field is its Larmor radius $r_{L,e} = \frac{|\vec{v}_{\perp,e}|}{\omega_{c,e}}$. For a strong magnetic field with $\omega_{c,e}\tau >> 1$, the diffusion coefficient due to neutral scattering is given in [11] as

$$D_\perp \quad = \quad \frac{k_B T_e}{m_e \tau \omega_{c,e}} \propto \frac{\vec{v}^2_{th,e}}{v^2_{\perp,e}} \frac{r^2_{L,e}}{\tau} \propto \frac{1}{B^2} \quad . \tag{2}$$

While the Larmor radius is proportional to $1/B$, the diffusion across the magnetic field scales with $1/B^2$. While for diffusion along magnetic field lines collisions are decreasing the mean free path and thus the collision coefficient, here collisions are necessary, therefore $D_\perp$ is proportional to the collision frequency $\nu = 1/\tau$. But in many experiments on the magnetized plasmas, the contribution of classical diffusion is not sufficient to explain the measured electron transport across the magnetic field lines [12]. Another kind of diffusion is the so-called "anomalous" or Bohm diffusion, which is due to electron scattering on the fluctuations of the perpendicular electric field. While in many $E \times B$ experiments $D_\perp$ scales with B^{-1} rather than with B^{-2}, a semi empirical formula was proposed by D. Bohm, E. Burhop, and H. Massey, with a diffusion coefficient [13]:

$$D_\perp = \frac{1}{16}\frac{k_B T_e}{eB} = D_B \quad . \tag{3}$$

A general derivation for $D_\perp \propto B^{-1}$ for this kind of diffusion was given by L. Spitzer in 1960 [12], with

$$D_\perp = 2(K_1 K_2)^2 K_3 \cdot \frac{k_B T_e}{eB} \quad . \tag{4}$$

$K_1,\ K_2,\ K_3$ are empirical constants, determining the strength of the electron perturbation perpendicular to the magnetic field.

To study anomalous diffusion in the HEMP thruster, a three dimensional electrostatic PIC code is used. Because the calculation is extremely time consuming, only a proof-of-principle for studying anomalous transport in a HEMP-like geometry was possible. The HEMP thruster has a cylindrical volume. But in a PIC simulation a cylindrical grid causes self forces. To avoid that, a Cartesian grid is chosen. The HEMP model is set up as a cuboid, based on a Cartesian grid. To be able to obtain a solution in a reasonable run time (one week), the size of the system is scaled down by a factor of 50. In order to preserve the ratio of the charged particles mean free paths and the gyroradii to the system length, the neutral Xenon density and the magnetic field are increased by the same factor 50 [6]. The simulation domain has a height and width of $L_x = L_y = 23mm$, a length of $L_z = 130mm$ and includes the thruster channel as well as the plume region, as shown in Fig. 10. The thruster exit is positioned at $z = 51mm$ and the two cusps at $z = 20.5mm$ (anode cusp) and $z = 37mm$ (exit cusp). The channel walls consist of boron nitride based ceramics. The external domain boundaries consist of metal walls with a potential of $\phi = 0$. The anode voltage, applied at $z = 0mm$ is set to $500V$. Particles which are hitting the metal as well as the dielectric boundaries are absorbed. In the thruster channel, these particles are contributing to the local surface charge. To identify anomalous diffusion driven by turbulence, no secondary electron emission was implemented. For the neutral xenon atoms, the density profile was prescribed by an exponential profile $n_n = n_n exp\{-Z/L\}$, with $L = Z_{max}/2.5$ and $Z_{max} = 65mm$. Such density profile is close to the one obtained from self consistent

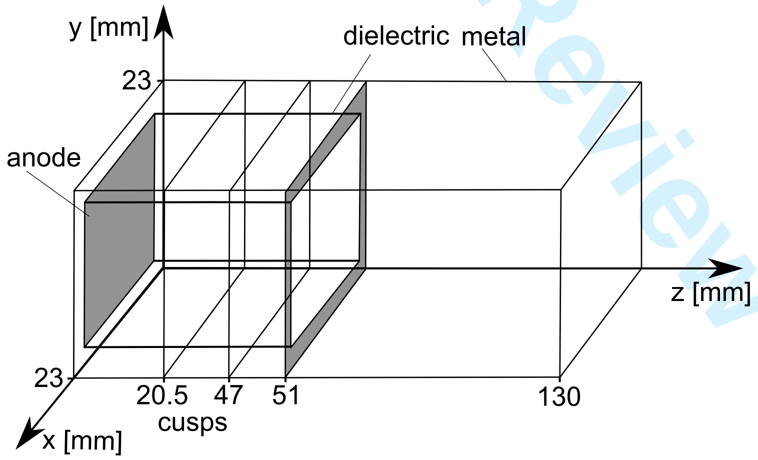

Fig. 10 Schematic view of the computational domain for a HEMP-like thruster model.

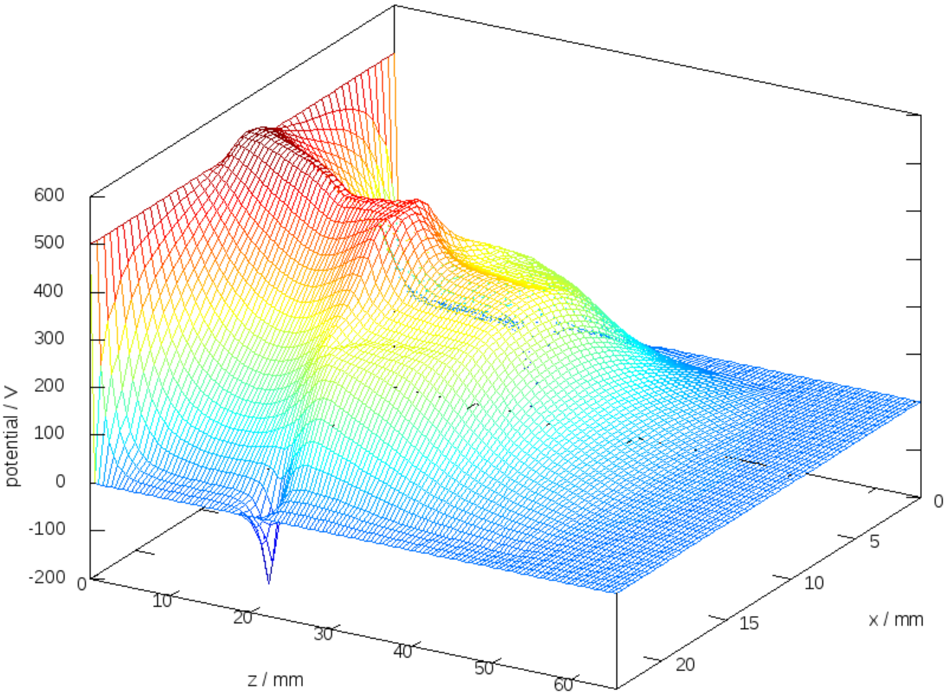

Fig. 11 Plasma potential of a HEMP thruster model, simulated with a 3D Cartesian PIC code, plotted along the y-axis of at $y = 15.5mm$.

models in 2D.

In the following, the three dimensional data is shown in two dimensional cuts. In Fig. 11 a profile of the plasma potential along the y-axis, for $y = L_y/2$, is shown. One can see that the potential has a step-like shape in the z-direction, which is caused by the two cusps. The potential shape is in overall agreement with the 2D results: the main potential drop occurs at the exit cusp, as shown in Fig. 2. At $z = 20.5mm$, the potential gets negative at the wall. This is the anode cusp region, where the magnetic field lines are perpendicular to the wall. The second cusp region can be identified by a potential plateau in the magnetic bottle between $z = 23 - 37mm$.

In Fig. 12 the potential in this cusp is shown in the x-y-plane. The variation of the potential is not purely radial. One can identify a $n = 1$ azimuthal mode at about $R = 3mm$ and a $n = 2$ mode at about $R = 7mm$ with an amplitude of electric field $E \approx 100V/cm$. These fluctuations of the azimuthal electric field are responsible for the anomalous electron transport across the cusps in the simulation.

The electron density is shown in Fig. 13 and 14. The density profile for $y = L_y/2$, Fig. 13, shows a large electron density at the anode ($z = 0$) and at the anode cusp ($z = 20.5$). The density drop between the two regions is due to the electron transport along magnetic field lines. At the exit cusp, practically no electrons can be found, because it is not yet filled with charged plasma particles due to run-time limits of the code. Due to that, no negative wall potential for the exit cusp can be seen in Figure 11. In Fig. 14, the electron density in the x-y-plane at the anode cusp $z = 20.5mm$ is shown. A high electron density in the enter of the model can be seen. Similar to the potential, stretching and compression along the diagonals is visible.

Estimation of the anomalous diffusion coefficient, caused by the fluctuations of the azimuthal electric field following the approach suggested in [12] gives

$$D_\perp \propto 0.4 \cdot \frac{kT}{eB}$$

which is in the order of magnitude of the diffusion coefficient given by Equ.(3). One has to mention, that the presented calculation is only a rough estimate, because of the large scaling factor used in the simulation.

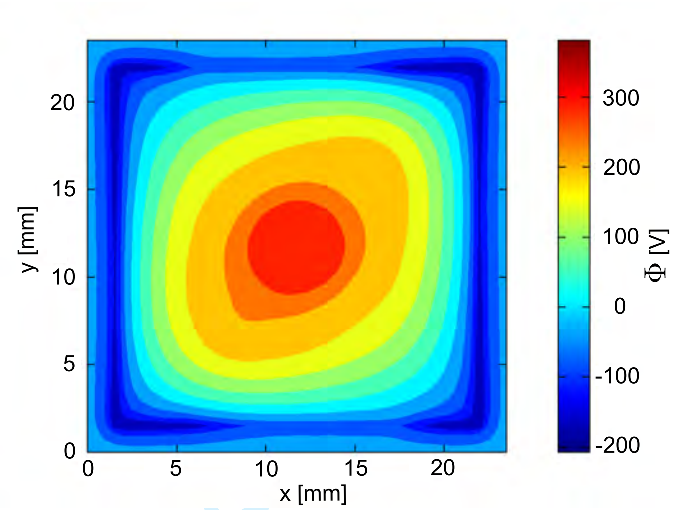

Fig. 12 Plasma potential of a HEMP thruster model in the $x-y-$plane at the cusp region $z = 20.5mm$.

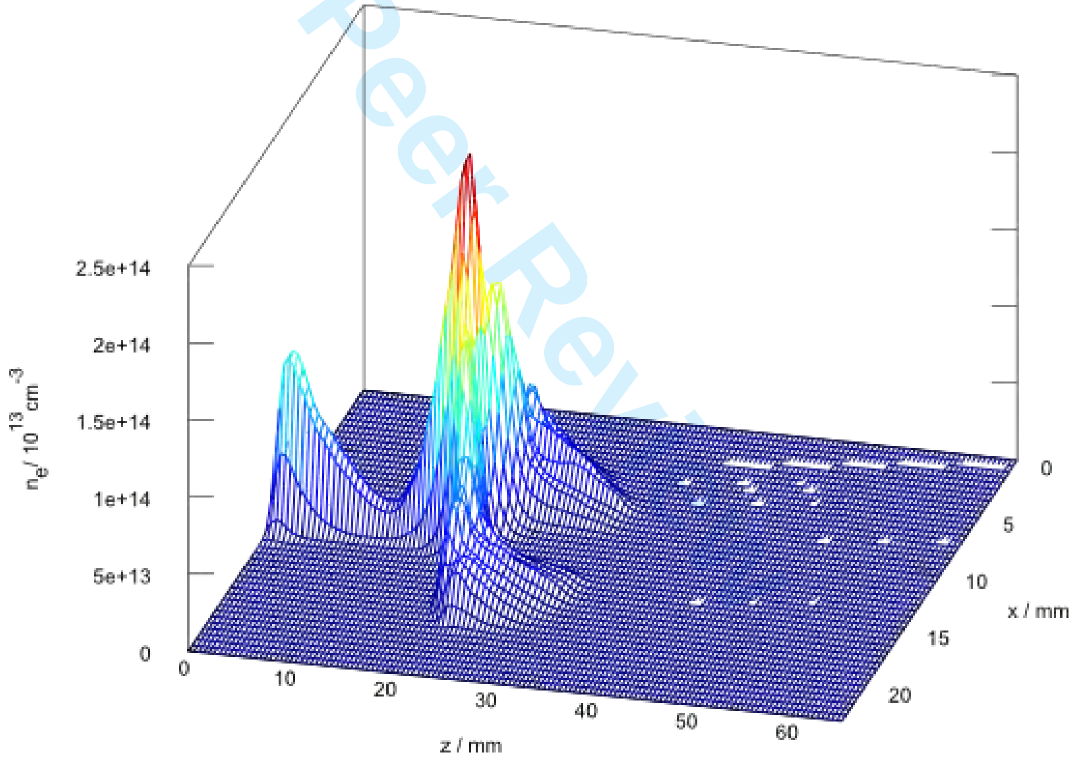

Fig. 13 Electron density along the y-axis of a HEMP thruster model at $y = 15.5mm$.

Due to the geometrical characteristics of the HEMP-T with large parts where the magnetic field is essentially axial and only small zones of radial fields at the cusps, the anomalous transport is only important at the cusps. Here, the anomalous diffusion allows the electrons to overcome the radial magnetic field and to fill the region between cusps. In the region of axial fields the parallel transport along fieldlines dominates. This is different to Hall thrusters, where in the whole acceleration channel the radial magnetic field is applied and the thruster characteristics is determined by anomalous electron transport. As a consequence modeling optimization with a 2D code of HEMP-T is possible, because classical transport dominates.

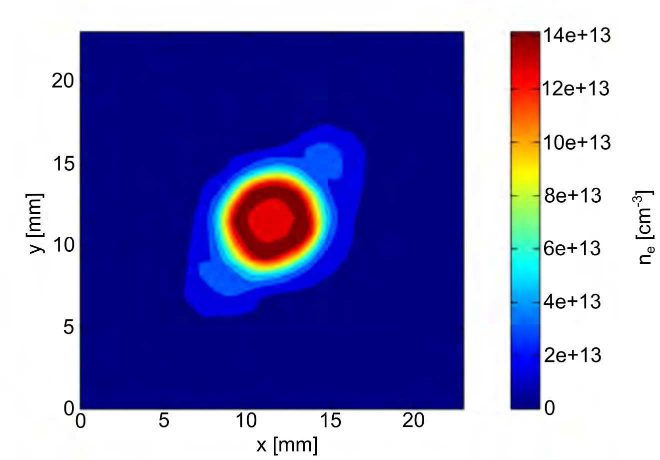

Fig. 14 Electron density of a HEMP thruster model in the $x-y-$plane at the cusp region $z = 20.5mm$.

5 Plume modeling

Up to now, either fluid or hybrid models (with kinetic ions) are used for the plume modeling. However, the plasma in the acceleration channel is already non-Maxwellian [14]. The mean free paths of particles in the plume of about $\sim 10\ m$ does not allow a relaxation of the distributions to a Maxwellian in the plume region. Therefore, a correct model of the plume plasma has to be kinetic. Unfortunately, the well-established Particle-In Cell (PIC) method is momentum conserving and free of artificial self forces only in the case of equidistant meshes [8]. This means that a self-consistent PIC model for an ion thruster including the full plume plasma has to resolve the smallest length scale (usually the Debye scale at the largest electron density inside the thruster) and the fastest time scale (usually the plasma frequency at the largest electron density inside the thruster). A typical thruster size is about $10\ cm$ whereas the typical size of interest for a plume is $1\ m \sim 10\ m$. Electron density inside the thruster is about $\sim 10^{13}\ 1/cm^3$ and for such a density $\lambda_D = 7.43 \cdot 10^{-4}\ cm$ for $T_e = 10\ eV$. In the plume plasma density drops exponentially, such that on a distance of $\sim 5\ cm$ from a thruster nozzle it is around $\sim 10^{10}\ 1/cm^3$ which results in $\lambda_D \sim 10^{-2}\ cm$. This allows only small domains for the plume due to computational time restrictions [6]. Such small domains suffer from the strong influence of the solution from the boundary conditions at the end of the plume, which can lead to results that are not consistent with experimental data, especially in terms of angular ion distribution functions. Fig. 15 demonstrates the influence of boundary conditions on a potential solution in the near-plume region. In addition, non-linear coupling of a plasma inside the thruster with the plume part may influence the operational regime of the thruster, including currents, density distributions and thrust.

The presented method uses a ”matryoshka-like” hierarchy of equidistant grids with different cell sizes. The hierarchy is constructed such, that the most dense grid covers only the thruster and the near-plume region; the next level with a cell size of $2 \sim 4$ times larger extends further to capture more of the plume and so on. Thus, the thruster and the near-plume region is covered with all grids and the most distant from the thruster regions are covered only by the most coarse grid. Furthermore, the density of the charged particles is gathered in all grids independently. The Poisson equation is solved one by one starting from the most coarse and finishing the most dense grid such, that the boundary values for the next level are taken from the coarser mesh obtained on the previous step. Such an approach appears to be not only accurate enough, but also remarkably fast compared with the solution for a single non-equidistant mesh. Such a fast solver is possible due to two reasons. First, the matrix which one gets after the discretization of the Poisson equation for an equidistant grid has a block structure. Such a structuring can be used by specialized solvers, for example [15] or [16]. And second, for such a single mesh one has a larger matrix to solve, rather then for the case of ”matryoshka-like” grids.

However, non-equidistant grids suffer from artifacts [8], like self-forces, and corrections to minimize such errors are needed. To overcome this, a modified two point central difference scheme for calculation of the electric field on non-equidistant grids is implemented [17].

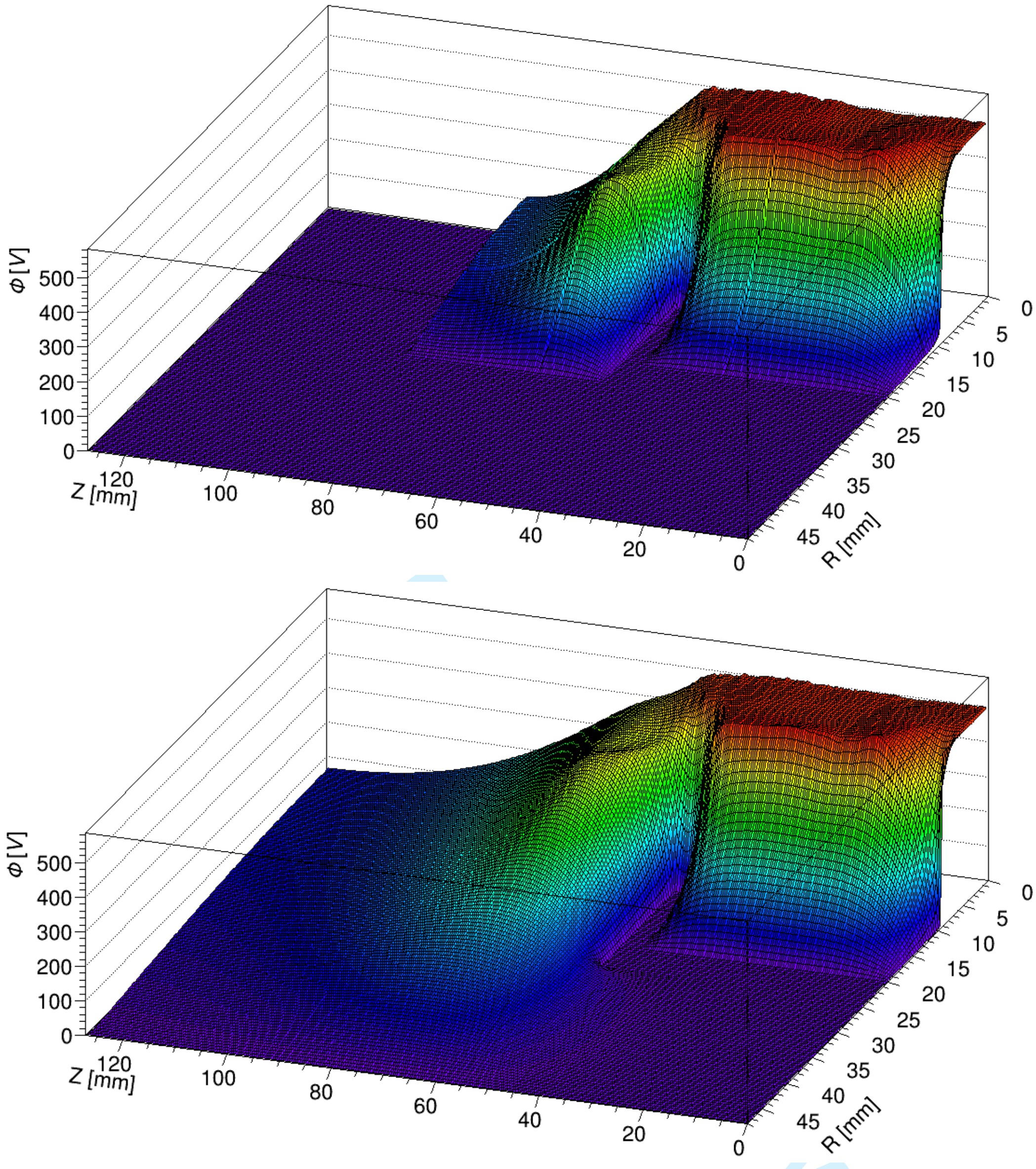

a)

b)

Fig. 15 Influence of boundary conditions on a potential solution for **a)** a small and **b)** a large simulation domain.

6 Effects due to impinging ions

Ions created in the thruster discharge may impinge surrounding surfaces which can induce sputter erosion and re-deposition of eroded material. Depending on the surface region this may affect operational and performance characteristics of the thruster itself, of the ion thruster module or even of the whole satellite, respectively. For the simulation one can distinguish:

a) Impact on inner thruster surface by ions generated in the inner thruster discharge.

b) Impact on exit-sided surface of the thruster and the neutralizing electron source by ions generated in the plasma plume downstream the thruster exit.

c) Impact on satellite surface producing erosion and re-deposition.

d) Impact on vacuum chamber walls during testing and life-time qualification creating redeposition onto thruster and thruster module surface.

The proposed multi-scale modeling strategy is well suited to address the above mentioned ion impingement effects. A good approximation of a plasma surface interaction are binary collisions between the impinging ion, which gets neutralized next to the surface, and the target atoms, producing collisional cascades in the solid. When a part of the collided particles get enough energy to leave the surface, the target emits them as sputtered particles. Sputtered particles are impurities in a plasma, values of sputter yields are important for plasma experiments and simulations. A tool for simulating binary collisions in matter is the SD.Trim.SP (Stationary/Dynamic Transport of Ions in Matter, with the calculation mode Serial or Parallel) code.

The SD.Trim.SP computer program simulates sputtering, backscattering and transmission effects of ion bombarded material and can additionally take the modification of the target into account, when it runs in the dynamic mode. It applies the Monte-Carlo Binary Collision Approximation (BCA) and assumes therefore an amorphous (randomized) material with a infinite lattice size and a temperature of $0K$. In SD.Trim.SP the particle movement in matter is approximated as a series of inelastic binary collisions between atoms, the BCA and a continuous friction, to simulate the interactions of moving atoms with electrons. For additional information about the use of SD.Trim.SP, see [18]. The domain of SD.Trim.SP, is a one dimensional simulation space, where the Cartesian x-component is perpendicular to the surface. Also two dimensional simulations are possible A negative x-component indicates the space above the surface, while a positive one shows the position in the solid. Also layers of different materials can be implemented. SD.Trim.SP in static mode proceeds in the following way. At first a projectile is initialized with the kinetic energy E_0 and the direction $\vec{r_0}$. After a distance of λ, a collision partner is determined by the stochastic choice of an impact parameter p. While SD.Trim.SP assumes an amorphous structure of the material, no lattice structure has to be taken in account and therefore λ and p are determined by their distribution functions given by the BCA. Both are implemented with inverse Monte-Carlo sampling. The azimuthal angles between two collisions are chosen randomly between $[0; 2\pi]$. The BCA gives the energies of the particles after the collision and the scattering angle ϑ_1 as well as the recoil angel ϑ_2, which are determining the new direction of the projectile and the target atom. The energy loss of atoms traveling through matter, due to interactions with electrons, is simulated as a continuous friction in between two collisions. Three scenarios are possible for each particle. If the energy is smaller than the binding energy of the matter $E < E_b$ the particle sticks and is not followed any more. If $E > E_b$ and the particle is close enough to the surface, it gets emitted as a sputtered atom and is also not followed any more. In the third case the particle moves through the matter and produces a collision cascade through several collisions, proceeded as described above. Reflection at the surface is realized with different binding energies for particles coming from inside or outside the target. To determine the dynamics of the target thickness, SD.Trim.SP has a dynamic mode. Here, the material is resolved one dimensional and the target is segmented into slabs. These slabs have an initial thickness, which changes during the calculation due to collisional transport. For many particles, the calculation as well as the memory occupation of every collisional cascade becomes very costly. Therefore, for large fluence pseudo particles which are representing a number of real particles are introduced to minimize the numerical costs. For an entire dose of Φ_0 the material should be exposed with, pseudo particles with a differential fluence of $\Delta\Phi = \Phi_0/N_d$ are followed in N_d simulation steps. Moreover, the physical sputter yield rapidly decreases for energies lower than a threshold energy E_{thr}.

Although the coupling of the BCA and the PIC models is promising in terms of analyzing erosion of a thruster during its operation, it is in practice inapplicable for other above mentioned tasks (c and d). That is why a Monte-Carlo model, which uses sputter yield tables pre-calculated with a binary collision cascade model is developed [18]. Coupling the plasma model with this erosion module an integrated model can be set up. The plasma fluxes impinging on the walls from PIC are used in a Monte-Carlo procedure for erosion re-deposition simulations, where the erosion fluxes are determined from the tables. Application of this model is discussed in [19].

A terrestrial qualification of a thruster has a significant difference from outer space exploitation in that it is held in a limited vessel, which can create different artifacts on the measured thruster properties. For example, the back scattered flux from vessel walls can be deposited on the walls of the thrusters and by that create a conducting layer influencing the thruster operating regimes. The quantitative characterization of such an influence is possible by means of a self-consistent coupling between the PIC code modeling of the plasma and the Monte-Carlo (MC) erosion-deposition code modeling of erosion of the thruster walls due to plasma-wall interaction and of deposition of the eroded particles both from vessel and thruster walls. Due to large size difference of a thruster and a vessel it is possible to parametrize the back-scattered flux from vessel walls as an effective source for the MC erosion-deposition code. The primary distribution of ions with respect to energies, angles and species is specified and pseudo-particles are followed interacting with the vessel walls. Hitting a wall, based on sputter rates calculated by a binary collision cascade code, the back-flow of eroded particles from vessel walls towards the ion thruster acceleration channel is calculated [20]. In case of metal walls large erosion is appearing, whereas for carbon walls much smaller physical sputtering happens. However, in the case of carbon the release of hydrocarbons is a major problem linked to the sponge-like characteristics of carbon with respect to its interaction with hydrogen. This means that every time the vessel is opened a large amount of hydro-carbons are created due to the interaction of air with carbon. Due to the porous structure of graphite air molecules can diffuse quite deep into the bulk of such graphite tiles and produce there hydro-carbons. The ions bombarding these tiles release this large reservoir and create back-flow to the thruster. Co-deposited layers of hydro-carbons are created in the acceleration channel. These layers are getting conductive hence changing the potentials and produce sub-sequent problems. The result is a different performance of the thruster in the vessel compared to the one in space. Using instead of carbon metal walls the rates of physical sputtering are larger, but the evaporation at hot channel parts will prevent deposition inside the thruster.

Strategies to overcome this limitations by additional baffles are studied with the help of the Monte-Carlo erosion code. In Fig.17 the influence of a baffle on the back flow towards the thruster channel is sketched. Particles, accelerated by the thruster, impinge on the vessel walls and sputter its surface. Due to micro roughness of the surface, the distribution function of the sputtered particles follows a cosine function [21]. Its orientation is mainly vertical to the surface, but nearly independent on the incident angel of the accelerated particles. For baffles tilted away from the thruster, this cosine distribution results in a reduced amount of back-scatted particle towards the thruster channel.

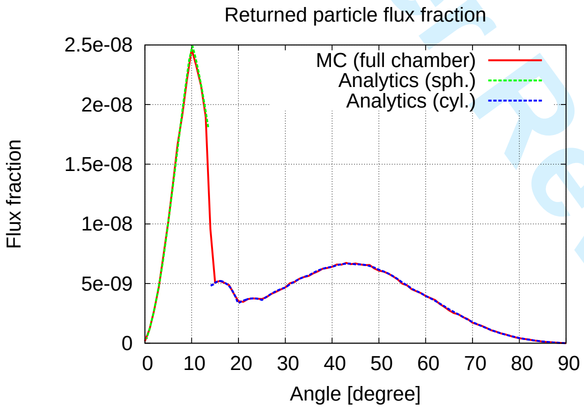

Fig. 16 Particle flux fraction at the thruster exit due to backscattering at vacuum vessel wall.

The calculated angular distribution of the back scattered particles by the Monte-Carlo simulation and from an analytical model are shown in Fig. 16. Due to the larger intersection of the solid angle with the thruster exit plane, the particle flux is larger for small angles of incidence. The returned particle flux consists of two parts, due to the vessel geometry. Sputtered particles from the spherical end are giving the contribution of small angles between 0 and 15 degrees, while for larger angles the sputtered particles are from the cylinder walls. The Monte-Carlo simulation (full line) agrees to the analytical calculations (dashed lines).

In further simulations these results can be used to verify structure of co-deposited layers inside the thruster channel and its impact on the measured thrust.The advantage of the shown simulation is its flexibility to analyze different vessel geometries. In spite of the low back-flowing fraction of emitted particles ($< 1\%$), these particles are producing co-deposited layers during the long test runs causing artifacts in the thrust. A strategy for avoiding this is to implement baffles in the vessel. While the $cos(\theta)$ distribution of the sputtered particles does not depend on the angle of incidence of the impinging ion, tilted baffles are turn the direction of the distribution and reduce the back-flow to the thruster exit, as sketched in Fig. 17. A implementation of baffles in the whole vessel, as

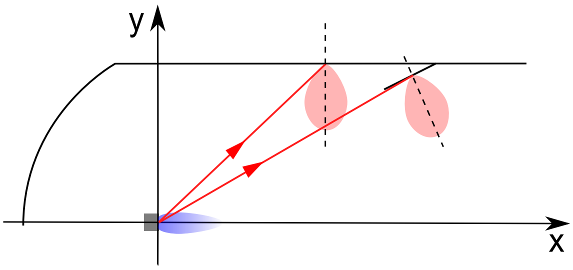

Fig. 17 Effect of a baffle on the distribution of sputtered particles.

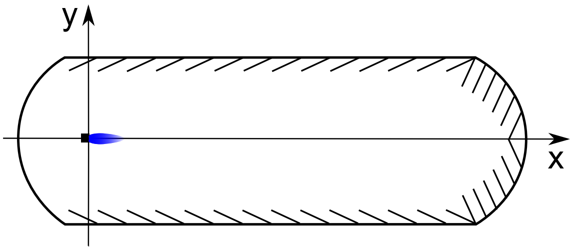

Fig. 18 Sketch of a vacuum vessel with implemented baffles.

sketched in Fig. 18 can reduce the back flow by $40\% - 66\%$. The results of this analysis have entered directly the preparation of the life-time qualification set-up for the HEMP-T system foreseen for the SGEO satellite [5]. The vacuum vessel was equipped with baffles tilted by about 20° to reduce artifacts due to sputtered particles from the vessel walls.

7 Conclusions

An integrated, modular approach is suggested to address the multi-scale problem of combined thruster-plume models. This approach covers ion-thruster plasma, plume and plasma wall interaction. A hierarchical multi-scale set of models in which the parametrization for a lower hierarchy model is deduced from a higher one is proposed. In the frame of such an approach the 3D PIC model could be used to parametrize turbulence effects on the electron mobility in the 2D PIC model. Due to the non-Maxwellian characteristics of plasma the 2D PIC is chosen as the core of the approach for analyzing both in-thruster and plume plasmas. The idea of the ”matryoshka-like” set of grids is utilized to reach acceptable length scales with the capability to resolve even the plume kinetically. Furthermore, the modified central different scheme is used to obtain the electric field in order to minimize the error in the momentum conservation introduced by the use of the non-equidistant grid.

For the erosion, re-deposition analysis a direct coupling of the kinetic PIC model with binary-collision codes allows a detailed analysis of sputtering inside the thruster. To address longer scales including the plume and its interaction with the satellite Monte-Carlo approaches offer the best perspective, allowing even studies of the interaction of ion thrusters with the walls of the testing facilities and the development of strategies to minimize back-flows from vessel walls to the thruster by using appropriate baffle designs.

8 Acknowledgement

The authors would like to thank the German Space Agency DLR, specially Ralf Dittmann, Norbert Püttmann, Jürgen Schulze and Klaus Ruf for continuous support throughout Thales HEMP thruster system development.

References

[1] N. Koch, H. P. Harmann, and G. Kornfeld (eds.), Status of the THALES High Efficiency Multi Stage Plasma Thruster Development for HEMP-T 3050 and HEMP-T 30250, No. IEPC-2007-110, Florence, Italy, September 17-20, 2007.
[2] PANAMSATANNOUNCEMENT, Galaxy 10r satellite suffers propulsion system failure, Tech. rep., August 2004, http://www.spaceflightnow.com/news/n0408/05galaxy10r/.
[3] G. Kornfeld, H. Seidel, and J. Wegener, Plasma accelerator arrangement, 1999, Priority: Germany No. 198 28 704.6, filed 26 June 1998.
[4] G. Kornfeld, N. Koch, and H. P. Harmann, 30’th International Electric Propulsion Conference(IEPC-2007-108) (2007).
[5] A. Lazurenko, A. Genovese, S. Weis, M. Schirra, B. van Reijen, J. Haderspeck, P. Holtmann, K. Ruf, N. Püttmann, and N. Koch, Space Propulsion Conference(SP2012_2366197) (2012).
[6] K. Matyash, R. Schneider, A. Mutzke, O. Kalentev, F. Taccogna, N. Koch, and M. Schirra, IEEE Transactions on Plasma Since **38**(9, Part 1), 2274–2280 (2010).
[7] C. K. Birdsall and A. B. Langdon, Plasma physics via computer simulation (McGraw-Hill, New York, 1985).
[8] D. Tskhakaya, K. Matyash, R. Schneider, and F. Taccogna, Contrib. Plasma Phys. **47(8-9)**, 563–594 (2007).

[9] J. Bittencourt, Fundamentals of Plasma Physics, third edition (Springer Verlag, 2004).

[10] N. Koch, M. Schirra, S. Weis, A. Lazurenko, B. van Reijen, J. Haderspeck, A. Genovese, P. Holtmann, R. Schneider, K. Matyash et al., Proceedings of the 32nd International Electric Propulsion Conference (2011).

[11] F. F. Chen, Introduction to Plasma Physics and Controlled Fusion (Springer Verlag, 1984).

[12] L. Spitzer, Physics of fluids **3**(4), 659–661 (1960).

[13] D. Bohm, E. Burhop, and H. Massey, The characteristics of electrical discharges in magnetic fields (New York: McGraw-Hill, 1949).

[14] F. Taccogna, S. Longo, M. Capitelli, and R. Schneider, Contributions to Plasma Physics **47**(8-9), 635–656 (2007).

[15] P. Kravanja and M. Van Barel, Calcolo **33**(1-2), 147–164 (1996).

[16] E. Chow and Y. Saad, SIAM Journal on Scientific Computing **18**(6), 1657–1675 (1997).

[17] D. Tskhakaya et al., Self-force in 1d electrostatic particle-in-cell codes for non-equidistant grids, to be published, 2013.

[18] W. Eckstein, R. Dohmen, A. Mutzke, and R. Schneider, SDTrimSP: A Monte-Carlo Code for Calculating Collision Phenomena in Randomized Targets (Max-Planck-Institut für Plasmaphysik, 2007).

[19] J. Duras, O. Kalentev, A. Mutzke, K. F. Lüskow, and R. Schneider, Interactions between ion thruster plumes and vessel walls, to be published at 33'IEPC, October 2013.

[20] O. Kalentev, L. Lewerentz, J. Duras, K. Matyash, and R. Schneider, Journal of Propulsion and Power **29**(**2**), 495–498 (2013).

[21] W. Eckstein, Springer Series in Materials Science **10** (1991).

Acta Polytechnica **55**(1):7–13, 2015
`doi:10.14311/AP.2015.55.0007`

MONTE-CARLO RE-DEPOSITION MODEL DURING TERRESTRIAL MEASUREMENTS OF ION THRUSTERS

Julia Duras[a,*], Oleksander Kalentev[a], Ralf Schneider[a,b], Konstantin Matyash[b], Karl Felix Lüskow[a], Jürgen Geiser[a]

[a] *Institute of Physics, Ernst-Moritz-Arndt University Greifswald, Felix-Hausdorff-Str.6, D-17498 Greifswald, Germany*

[b] *Computing Center, Ernst-Moritz-Arndt University Greifswald, Felix-Hausdorff-Str.12, D-17498 Greifswald, Germany*

[*] corresponding author: `julia.duras@physik.uni-greifswald.de`

Abstract. For satellite missions, thrusters have to be qualified in large vacuum vessels to simulate the space environment. One caveat of these experiments is the possible modification of the beam properties due to the interaction of the energetic ions with the vessel walls. Impinging ions can produce sputtered impurities or secondary electrons from the wall. These can stream back into the acceleration channel of the thruster and produce co-deposited layers. Over a long operation time of thousands of hours, these layers can modify the optimized geometry and induce changes in the ion beam properties, e.g., broadening of the angular distribution and thrust reduction. A Monte Carlo code for simulating the interaction of ion thruster beams with vessel walls was developed to study these effects. Back-fluxes of a SPT-like ion thruster for two different test-setups and vessel geometries are calculated.

Keywords: Ion thruster, Monte-Carlo method, terrestrial testing of thrusters, interaction with vessel walls.

---

1. Introduction

Ion thrusters, where the propellant is ionized and the ions are accelerated by electric fields, are of increasing importance for scientific and commercial space missions. Compared to commonly used chemical thrusters they have a 5 to 10 times higher specific impulse [1]. This results in a considerably reduced propellant budget, and a significant reduction of spacecraft launch mass by some 100 to 1000 kg can be achieved. One concept for this electric propulsion involves grid-less ion thrusters, which are based on magnetic confinement of the plasma electrons, where the trapped electrons both ionize the propellant and provide the potential drop for ion acceleration. Due to their low complexity in terms of system architecture, they are becoming of increasing interest in particular for commercial satellites.

In order to reduce the development and qualification costs, it is therefore necessary to set up and apply a series of different modeling tools which can quantitatively describe the plasma physics within the thruster, and also the interactions of the thruster with the testing environment and finally with the satellite. The integrated modeling strategy should include several modular components in a consistent way in order to provide the complexity and accuracy required for the problem [2].

Ions created in the thruster discharge may impinge on the surrounding surfaces, which can induce sputter erosion and redeposition of eroded material. Depending on the surface region, this may affect the operational and performance characteristics of the thruster itself, of the ion thruster module, or even of the whole satellite. For the simulation, one can distinguish:

(a) The impact on the inner thruster surface by ions generated in the inner thruster discharge.
(b) The impact on the exit-sided surface of the thruster and the neutralizing electron source by ions generated in the plasma plume downstream the thruster exit.
(c) The impact on the satellite surface producing erosion and redeposition.
(d) The impact on the vacuum chamber walls during testing and life-time qualification, creating redeposition onto the thruster and thruster module surface.

The proposed multi-scale modeling strategy is well suited to address these ion impingement effects.

The outline of the paper is as follows: the modeling strategy is described and the problems of artifacts during terrestrial qualifications are outlined. As one example of this modeling, the influence of the test-setups on particle back-fluxes towards the ion thruster channel is studied with a Monte Carlo model for an SPT-like ion thruster. Finally, the results are summarized.

2. Modeling strategy

The most complete model resolving all time scales of ion thrusters would be a direct coupling of a kinetic plasma model with a molecular dynamics model for the walls. This would allow a fully self-consistent analysis of the complete system, including plasma dynamics, possible erosion of the thruster walls and the interaction of the exhausted ions with the surrounding satellite surfaces or, during testing and qualification, with the testing environment, like the vacuum chamber walls. This type of solution is not feasible, due to the tremendous computational costs and the high complexity of this combined model. Instead, we propose to use a hierarchical multi-scale set of models, in which the parameterization for a lower hierarchy model can be deduced from a higher level model.

For example, a 3D particle-in-cell (PIC) model can deliver a parameterization of turbulence effects by appropriate anomalous transport coefficients. Transport coefficients based on these runs could then be used in a 2D PIC, which is more practical for production runs.

To get a correct description of both the thruster and the plume plasma, one has to solve a kinetic problem for the whole region of interes,t including all significant physical processes. These are collisions, turbulence effects, surface driven sheath instabilities and breathing modes. A PIC model is therefore a natural choice for this problem. In addition, similarity scaling is applied to further reduce the calculation costs [3].

In order to describe erosion-redeposition processes, one can use various approximation levels of the model. The most thorough description is given by the full molecular dynamic model. However, this would be far too time-consuming, because it resolves each individual atom and their interactions. The next level can be represented by the binary collision cascade model, which assumes an amorphous target and the interaction of particles with the solid based on heavy particle collisions with ions, and additional losses with electrons acting as a viscous force. This model can use the detailed information about flux distributions provided by the PIC code, and can then, on the basis of this, the erosion response of the materials. The most crude approximation is given by a Monte-Carlo (MC) procedure simulating erosion-redeposition on the basis of sputter yield tables calculated from the binary-collision cascade or molecular dynamics model together with information about the plasma fluxes. This model is particular useful due to its simplicity and flexibility for the quantifying the lifetime of ion thrusters.

3. ARTIFACTS DURING TERRESTRIAL MEASUREMENTS OF AN ION THRUSTER

Terrestrial qualification of a thruster differs significantly from outer space exploitation, in that it is held in a limited vessel, which can create various artifacts on the measured thruster properties. For example, the back scattered flux from the vessel walls can be deposited on the walls of the thrusters, and can in that way form a conducting layer influencing the thruster operating regimes. These measurements are taken in large vacuum vessels, up to 10 times larger than the thruster itself, in order to provide a space-like environment. Despite these dimensions, however interactions of exhausted particles with residual gas and vessel walls still take place and can modify the measurements. One source of differences between measurements in space and during terrestrial testing is the re-deposition of sputtered particles inside the thruster channel or for the grid thruster at the thruster walls. The accelerated ions impinge on the vessel walls and produce sputtered impurities. These can stream back towards the acceleration channel of the thruster and produce co-deposited layers. Over a long operation time of thousands of hours, these layers can modify the optimized geometry of the thruster channel or grids and the inner wall surface. This induces changes in the ion beam properties, e.g., broadening of the angular distribution and thrust reduction, as observed in the test campaigns of HEMP-T [4] and the NEXT grid thruster [5]. A reduced back-flux is therefore important to minimize artifacts in the plume measurements.

Due to the large size difference between the thruster and the vessel, it is possible to parameterize the backscattered flux from the vessel walls as an effective source for the MC erosion-deposition code. This paper will show that the position of the thruster inside the vessel, the wall material and the vessel geometry play important roles and can influence the plume measurement results.

4. DESCRIPTION OF THE MONTE CARLO MODEL

The Monte Carlo (MC) method is a common approach for plasma-wall problems, for example MC simulations of sputtering and re-deposition are well established in fusion-oriented studies [6] as is magnetron sputtering [7, 8]. The idea of the Monte Carlo model is to sample the primary distribution of the ions with respect to energies, angles and species. These pseudoparticles are followed hitting the vessel walls and generating sputtered particles, based on sputter rates calculated by a binary collision cascade code. Their angular distributions are sampled and the back-flow of the eroded particles from the vessel walls towards the ion thruster acceleration channel is calculated.

In this work, we assume that particles move along rays according to their source distribution. In this 3D model, the vacuum chamber is assumed to be a cylinder with two spherical caps attached to its ends. The angular source distributions of the mean ion energy, the current and the species fraction were generated with respect to the emission angle θ, see Fig. 3. As an example, ion current and energy distributions similar to those published for SPT-100 [9] are used. The fraction of Xe^{2+} to Xe^{+} ions is taken

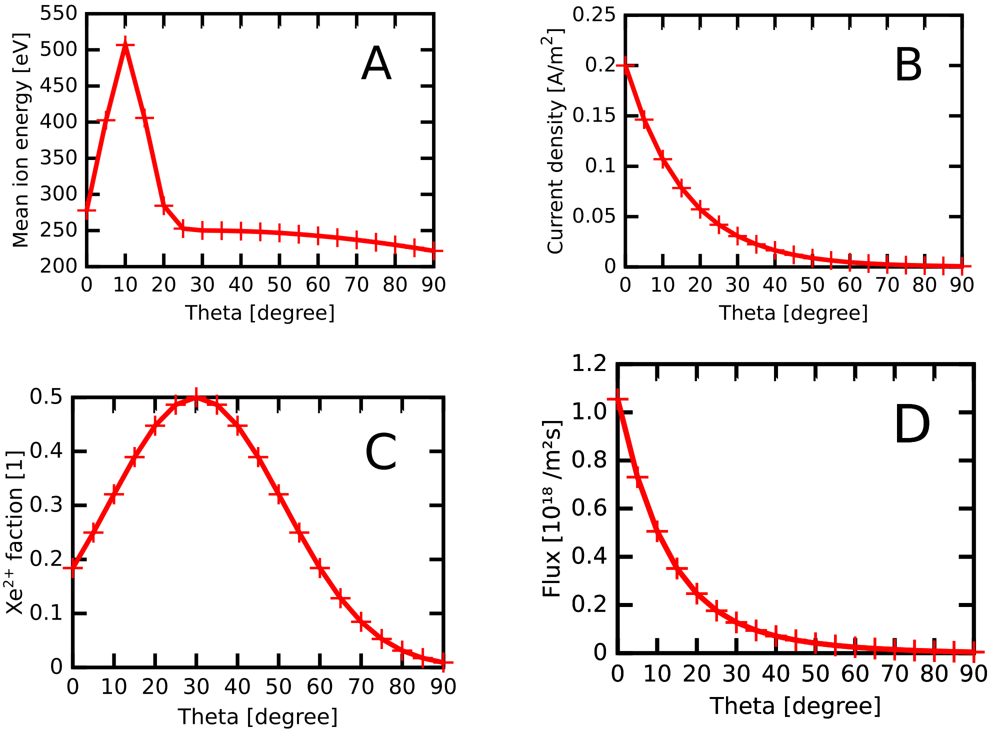

Figure 1. Distribution of mean ion energy (A), current density (B), Xe^{2+} faction (C) and the resulting emitted flux (D) similar to SPT-100.

arbitrarily. All used source distributions used here are shown in Fig. 1(A)–(C), sampled as a point source at the thruster exit, within angular steps of $\Delta\theta = 5°$. The resulting emitted flux

$$\Gamma(\theta) = \frac{j(\theta)}{e \cdot (1 + f^{\mathrm{em}}(\theta))}$$

is shown in Fig. 1(D), where $j(\theta)$ is the current density, e is the elementary charge and $f^{\mathrm{em}}(\theta)$ is the emitted Xe^{2+} fraction. Equal distribution of the poloidal angle is used. This distribution represents an emitted beam of Xenon ions with a mean emission angle of $\theta^{\mathrm{em}} = 0°$. The sputter yield for the impinging ions on the vessel walls is taken from SDTrimSP [10] simulations. While the thruster is operating, ions with energies larger than the sputter threshold form a micro roughness on the thruster surfaces. Due to shadowing, this micro-roughness modifies the real angle of incidence, effectively reducing its range to values between 20° and 50°. For this angular range, the sputter yields vary only slightly with angle. We therefore assume that the sputter yields depend only on the energy of the impinging ions. It is also assumed that the sputtered particles obey a cosine law [11] for their angular distribution. Due to their low energies, the sputtered particles are assumed to have a sticking coefficient of 1. Therefore, only particles with direction towards the thruster exit are followed. A detailed description of the Monte Carlo model and its validation with analytic calculations can be found in [12].

In the following, the influence of the thruster position inside the vessel is studied. This is important, since ion thrusters are qualified within various test-setups.

5. Back-flux for two different test-setups

Measurements of plume parameters are taken in two different test-setups: a 'performance test', where a single thruster is placed in the center of the circular cross-section of the vesse,l and an 'end-to-end test', where four thrusters are assembled as a cluster. Performance tests are typically carried out to test and qualifying single thrusters, while end-to-end tests give the characteristics of a whole cluster of thrusters, as it is applied on satellites where only one of the thrusters is operating. The following comparison of the two test setups shows strong dependency of the back-flux on this thruster position.

For the performance test, the ion thruster is placed co-axially in the vessel. In the following, the LVTF-1 vessel at Aerospazio [13] in Siena, Italy was taken as a reference. It has a cylinder length of $Z_c = 7.7\,\mathrm{m}$ and a radius of $R_c = 1.9\,\mathrm{m}$. The spherical cap at the end has a radius of $R_{sp} = 2.7\,\mathrm{m}$. For simplicity, the ion thruster is approximated by a cylinder with a length of $L = 9.0\,\mathrm{cm}$ and a diameter of $D = 9.0\,\mathrm{cm}$. In most test chambers, graphite-coated walls are used in order to reduce the back-fluxes of sputtered par-

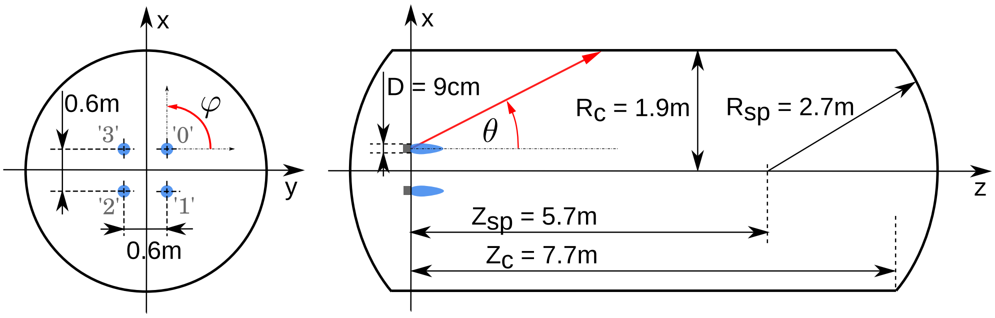

FIGURE 3. Sketch of a thruster cluster assembled in the LVTF-1 vessel within an end-to-end test set-up. '0' to '3' indicate the different thrusters.

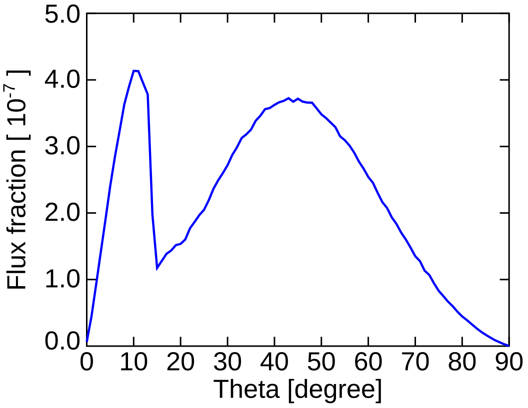

FIGURE 2. Calculated back-flux towards the thruster exit in total (total flux fraction of $1.97 \cdot 10^{-5}$).

ticles, since graphite has a lower sputter yield than aluminum. However, in the case of carbon the release of hydrocarbons is a major problem linked to the sponge-like characteristics of carbon with respect to its interaction with hydrogen. The sputtered hydrocarbons produce a co-deposited layer inside the thruster channel, which can become conductive and can therefore change the potentials and can produce subsequent problems. When carbon is replaced by metal walls, the rates of physical sputtering are larger, but the evaporation in the hot parts of the channel will prevent deposition inside the thruster [2]. Aluminum walls are therefore studied with the Monte-Carlo model.

Within this model, the back-flux is collected on a circle, which represents the thruster exit. The calculated back-flux fraction towards the source is shown by a blue line in Fig. 2. It is given by the number of particles hitting the thruster exit in a certain angular range $[\theta; \theta + \Delta\theta]$, with $\Delta\theta = 1°$, divided by the total number of source particles. For the chosen parameters of the vessel, the back-flux for $\theta = [0; 14°]$ originates from the spherical cap, while for $\theta = [14°; 90°]$ it comes from the cylindrical walls of the vessel. The flux fraction shows a pronounced peak at around 10° and a broader peak at about 45°.

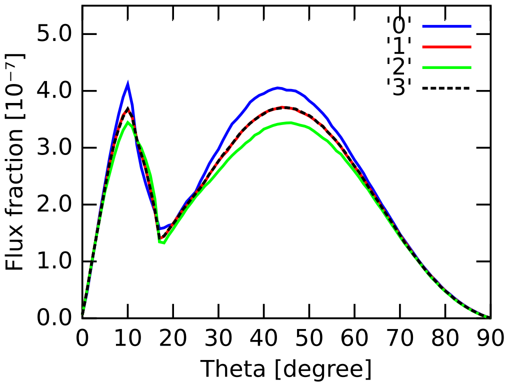

FIGURE 4. Calculated back-flux to four thruster channels with a total flux fraction of $f = 8.0 \cdot 10^{-5}$.

Thruster	$\int f(\theta)\, d\theta$
'0'	$2.11 \cdot 10^{-5}$
'1'	$2.00 \cdot 10^{-5}$
'2'	$1.91 \cdot 10^{-5}$
'3'	$2.00 \cdot 10^{-5}$

TABLE 1. Calculated back-flux to four thruster channels with a total flux fraction of $f = 8.0 \cdot 10^{-5}$.

These structures are determined by the combination of the mean ion energy distribution of the emitted Xenon ions, the sputter yield and the cosine distribution of the sputtered particles. The first peak at 10° is dominated by the maximum of the mean ion energy which takes place at the same emitting angle. The second peak is given by the combination of decreasing mean ion energy, with increasing θ and increasing back-flow as given by the cosine law. For zero degree emission angle less flux is seen, due to the small number of emitted particles in this angular region, because of its small circular area for $\theta \in [0; 1°]$.

For the 'end-to-end' simulations the same vacuum chamber was taken as a reference. A sketch of the implemented geometry is shown in Fig. 3. In order to reduce the artifacts further, all thrusters are pointing

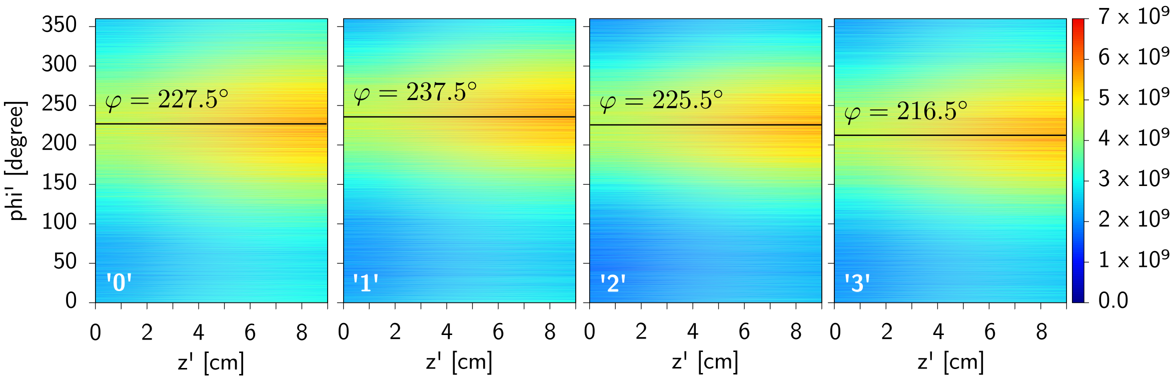

Figure 5. Re-deposited flux in $s^{-1}m^{-2}$ inside the four 9 cm long thruster channels within an end-to-end test setup at the LVTF-1 vessel. Total re-deposited flux $\Gamma = 4.3 \cdot 10^{+12}\,m^{-2}s^{-1}$

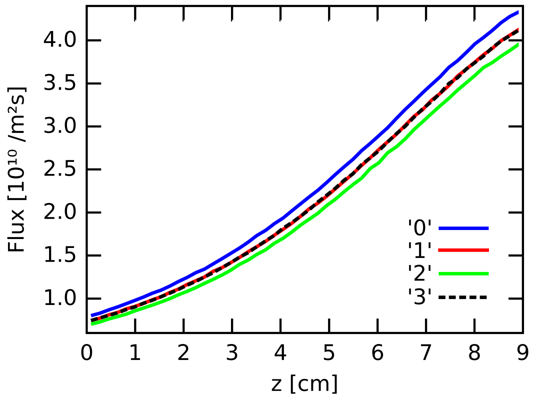

Figure 6. Re-deposited flux along the four thruster channels.

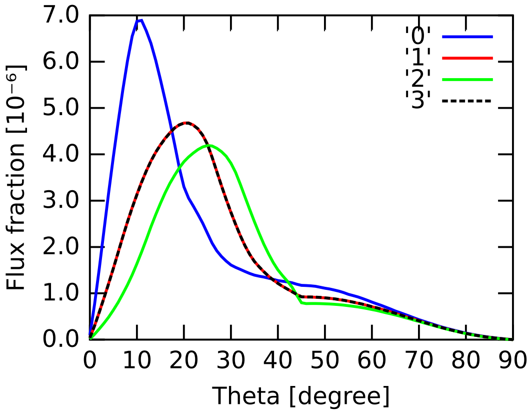

Figure 7. Calculated back-flux to four thruster channels with total flux fraction of $f = 5.7 \cdot 10^{-4}$ at the ULAN vessel.

Thruster	$\int f(\theta)\,d\theta$
‘0’	$1.61 \cdot 10^{-4}$
‘1’	$1.42 \cdot 10^{-4}$
‘2’	$1.26 \cdot 10^{-4}$
‘3’	$1.42 \cdot 10^{-4}$

Table 2. Calculated back-flux to four thruster channels with total flux fraction of $f = 5.7 \cdot 10^{-4}$ at the ULAN vessel.

in the same direction. Thruster ‘0’ was chosen as the operating thruster.

The computed back-flux fractions towards the thruster exit planes of all four thrusters are shown in Fig. 4. The integral flux fraction for each thruster is given in Table 1. Most of the back-flux is measured for thruster ‘0’, since it is the emitting source. One can see that the integral deposited flux decreases with distance to the source. Therefore, equal flux distribution for symmetrically placed thrusters ‘1’ and ‘3’ is reasonable. Since the emitting source is not placed co-axially in the vessel one cannot deduce, where the sputtered particles originate from. In addition, the back-flux is no longer equally distributed in poloidal direction. In Fig. 5, the back-flux on the simplified inner thruster channel wall is given with respect to the depth z' and the poloidal angle φ of the thruster. Here the z'-axis is the symmetry axis of the cylinder, where $z' = 0$ cm is at the anode and $z' = 9$ cm is at the thruster exit. As expected, the flux is slightly higher in the thruster exit region and decreases towards the thruster bottom, see Fig. 6. It shows the measured flux summed over the poloidal angle. In poloidal direction, the distribution varies and the angle with maximum flux

$$\varphi = \max_{\varphi} \int n(\varphi, z')dz'$$

along the z-axis is given in each plot. Thrusters ‘0’ and ‘2’ show approximately the same maximum angle, while for the others the angle is shifted by ±10°. This can be explained by the symmetric thruster positions within the vessel with respect to the emitting source. In total, the re-deposition distribution pattern is nearly the same for all four thrusters, due to the

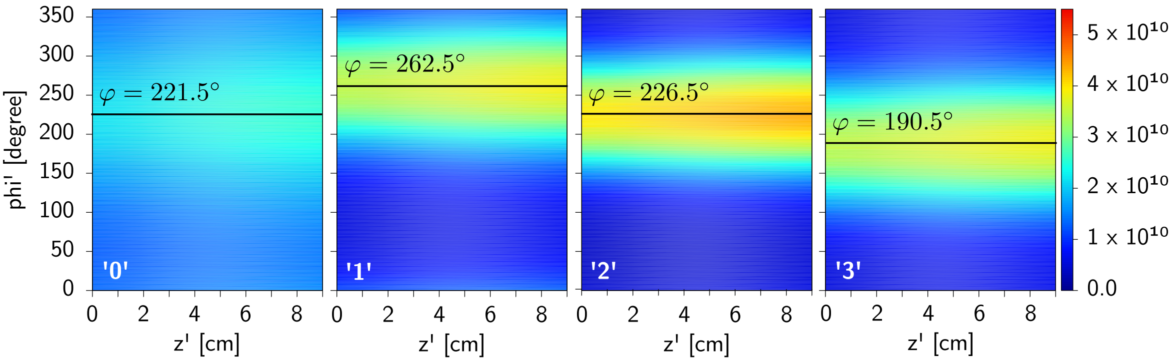

FIGURE 8. Re-deposited flux in $s^{-1}m^{-2}$ inside the four 9 cm long thruster channels within an end-to-end test setup at the ULAN vessel. Total re-deposited flux $\Gamma = 2.4 \cdot 10^{+13}\,m^{-2}s^{-1}$

large vessel geometry in comparison with the thruster size, and the narrow beam-like emission distribution.

For the purposes of comparison, the same simulation was carried out for a smaller vessel. The ULAN facility [14] in Ulm was modeled. It has a cylinder length of $Z_c = 2.9\,\mathrm{m}$ and a radius of $R_c = 1.2\,\mathrm{m}$. As in Aerospazio, the thruster cluster is placed co-axially in the vessel. In Fig. 7, the back-flux fraction at the exit planes and the integral flux fraction are given in Table 2. The total back-flux fraction $f = 5.7 \cdot 10^{-4}$ is about 14 times higher than for the larger Aerospazio vessel $f = 8.0 \cdot 10^{-5}$. A clearer distinction between the four thrusters and a different back-flux pattern develop. The maximum back-flux is measured for the emitting thruster '0', while it decreases with distance from the source, as can be seen in Tab. 2. These differences can be explained by the thruster position closer to the cylinder walls of the vessel. The back-flux for each channel is given in Fig. 8. Here, too, the re-deposition decreases with channel depth, as expected, but more pronounced re-deposition areas with parts of practically no re-deposition build up. In comparison with the larger vessel, the maximum peak is approximately one order higher. While for thruster '0' the re-deposition is almost equally distributed within the channel, a peak builds up with increasing distance from the emitting source, resulting in the highest maximum flux for thruster '2'. Also, the position of the maximum back-flux varies more in poloidal angles φ. Here, the symmetric thruster positions within the vessel with respect to the emitting source is important. These distribution characteristics correspond to observations during testing of the HEMP-T (B.van Reijen, personal communication, June, 2014).

Summarizing these results, a complex re-deposition profile appears due to the non-central position of the source within the vessel. Therefore, the source particles do not hit the vessel walls equally distributed in φ, which destroys the poloidal symmetry of the emitted flux hitting the vessel walls. In addition, the distribution of the sputtered particles is overlying, which gives no poloidal symmetry of the re-deposited particles, although the test-setup has such a simple geometry. The size of the vessel not only influences the amount of re-deposited particles but also gives a more pronounced re-deposition pattern.

6. CONCLUSION

A Monte Carlo model using a ray approximation for the particles allowsus to calculate the back-flux towards the thruster exit generated by sputtered particles at the vessel walls. It has shown the influence of the test set-up and the vessel size, which affects the re-deposition pattern inside the thruster channels. A non-centered emitting source leads to a complex re-deposition profile within the thruster channels. This effect can be diminished with a larger vacuum vessel which reduces the back-flux and smoothes the re-deposition patterns inside the channel. The emission distribution of the thruster itself also plays an important role. The results represent a worst case scenario, since the emission distribution of the thruster was assumed to be beam-like and aluminum was taken as the vessel wall material. For broader emission distributions and back-flux reducing modifications, e.g., carbon walls or baffles [2], the effects are reduced.

Effects like secondary electron emission at the vessel walls, which influence the plume potential, collisions of propellant ions with residual gas, regions of magnetized electrons in the plume and changes in the thruster potential due to re-deposited layers inside the channel are not considered within this model. In a future modeling step, the estimated back-flux distribution can be used for simulating the erosion and re-deposition on the thruster surfaces. This could clarify more precisely how terrestrial conditions influence the thrust measurements in total.

ACKNOWLEDGEMENTS

This work was supported by the German Space Agency DLR through Project 50 RS 1101.

REFERENCES

[1] N. Koch, H.-P. Harmann, G. Kornfeld (eds.). *Status of the THALES High Efficiency Multi Stage Plasma Thruster Development for HEMP-T 3050 and HEMP-T*

30250, IEPC-2007-110. 30th International Electric Propulsion Conference, 2007.

[2] O. Kalentev, K. Matyash, J. Duras, et al. Electrostatic Ion Thrusters - Towards Predictive Modeling. *Contributions to Plasma Physics* **54**:235–248, 2014. doi:10.1002/ctpp.201300038.

[3] K. Matyash, R. Schneider, A. Mutzke, et al. Kinetic Simulations of SPT and HEMP Thrusters Including the Near-Field Plume Region. *IEEE Transactions on Plasma Since* **38**(9, Part 1):2274–2280, 2010. doi:10.1109/TPS.2010.2056936.

[4] A. Genovese, A. Lazurenko, N. Koch, et al. (eds.). *Endurance Testing of HEMPT-based Ion Propulsion Modules for SmallGEO*, IEPC-2011-141. 32th International Electric Propulsion Conference, 2011.

[5] R. Shastry, D. A. Herman, G. C. Soulas, M. J. Patterson (eds.). *Status of NASA's Evolutionarry Xenon Thruster (NEXT) Long-Duration Test as of 50,000 h and 900 kg Throughput*, IEPC-2013-121. 33th International Electric Propulsion Conference, 2013.

[6] R. Behrisch, W. Eckstein. Springer-Verlag.

[7] V. Serikov, K. Nanbu. Monte Carlo numerical analysis of target erosion and film growth in a three-dimensional sputtering chamber. *Journal of Vacuum Science & Technology A: Vacuum, Surfaces, and Films* **14**(6):3108–3123, 1996. doi:10.1116/1.580179.

[8] C. Shon, J. Lee. Modeling of magnetron sputtering plasmas. *Applied Surface Science* **192**(1–4):258–269, 2002. Advance in Low Temperature RF Plasmas, doi:10.1016/S0169-4332(02)00030-2.

[9] L. King. *Transport-property and mass spectral measurements in the plasma exhaust plume of a Hall-effect space propulsion system*. Ph.D. thesis, University of Michigan, 1998.

[10] A. Rai, A. Mutzke, R. Schneider. Modeling of chemical erosion of graphite due to hydrogen by inclusion of chemical reactions in SDTrimSP. *Nuclear Inst and Methods in Physics Research, B* **268**(17-18):2639–2648, 2010. doi:10.1016/j.nimb.2010.06.040.

[11] W. Eckstein. *Computer Simulation of Ion-Solid Interaction*, vol. 10 of *Springer Series in Material Science*. Springer, 1991.

[12] O. Kalentev, L. Lewerentz, J. Duras, et al. Infinitesimal Analytical Approach for the Backscattering Problem . *Journal of Propulsion and Power* **29**(2):495–498, 2013. doi:10.1002/ctpp.201300038.

[13] AEROSPAZIO Tecnologie s.r.l. `http://www.aerospazio.com` [2014-02-01].

[14] H.-P. Harmann, N. Koch, G. Kornfeld (eds.). *The ULAN Test Station and its Diagnostic Package for Thruster Characterization*, IEPC-2007-119. 30th International Electric Propulsion Conference, 2007.

8 Acknowledgement

At the end I want to thank all the people, who helped me during the compilation of this thesis.

I want to express my gratitude to my supervisor Prof. Dr. Ralf Schneider for his great support and all the inspiring physics discussions. Furthermore, I want to thank all members of the CompuS, group especially Lars, Gunnar, Julia, Daniel, Paul and Stefan. It was a pleasure to work with you all in this productive and cooperative atmosphere. I thank Uwe for all the interesting discussions about everyday life and a helping hand with administrative issues.

This thesis would not have been possible without the friendly cooperation and interesting discussions with Detlev Konigorski from the Airbus Group and Patrick Neumann from Neumann Space. I also want to thank the German Space Agency whose funding allowed me to work on this interesting topic and brought me to some great places at international conferences.

I like to thank my parents for their endless trust and support during my whole study time. At this point I like to mention that the last years in Greifswald made it possible to get to know some great friends. They are and were responsible for some unforgettable days and mostly evenings, allowing to escape from my studies.

Last but not least I am grateful to Karo, my girlfriend, for her continuous support and encouragement during all ups and downs of my research.